DEVELOPMENT OF HIGHLY SENSITIVE AND SELECTIVE OPTICAL AND ELECTRICAL SENSORS FOR MICRO-GAS CHROMATOGRAPHY

by

Karthik Reddy Chinna Balareddy

A dissertation submitted in partial fulfillment
of the requirements for the degree of
Doctor of Philosophy
(Electrical Engineering)
in The University of Michigan
2013

Doctoral Committee:
  Associate Professor Xudong Fan, Co-Chair
  Professor Yogesh B. Gianchandani, Co-Chair
  Professor Katsuo Kurabayashi
  Assistant Professor Zhaohui Zhong

To my family for their support and belief in me

Acknowledgements

This thesis would not have been possible with out the support, and help from so many people. To them I would like to extend my sincerest gratitude.

First, my parents, who supported me emotionally, and encouraged me to follow this dream, and my brother for helping to keep me sane.

Next I would like to thank my adviser Prof. Xudong Fan, whose guidance was so crucial for any of this work coming to fruition. Under his mentorship I have significantly improved my understanding of a multitude of different research topics and for that I am grateful.

To my committee, Prof. Gianchandani, Prof, Kurabayashi, and Prof. Zhong for their advice and collaborations.

I would like to thank all the past and present members of the Fan Lab, Wonsuk Lee, Jing Liu, Maung Khaing Kyaw Oo, Yunbo Guo, Yuze Sun, John Suter, Hao Li, Yubo Li, Di Chen, Qiushu Chen, Xingwang Zhang, Yunhan Luo, Xiangwei Zhao, Chung-Shieh Wu, and Xiang Wu. It's been great working with everyone and my interactions with my group members has left a lasting impression on me.

I would like to thank my collaborators Kee Scholten and Girish Kulkarni, as well as their advisers, Prof, Zellers and Prof. Zhong.

My thanks go out to the EECS department, Rackham, WIMS, SSEL, NSF and the Lurie Nanofabrication facility for their support, either financially or through facilities.

Last but not least I'd like to thank all my friends, who are too numerous to name, but you know who you are. It's been a huge amount of fun and thank for helping me enjoy graduate school.

In case I missed anyone, I am sorry. It was not intentional.

Table of Contents

Chapter

List of Figures

Figure

List of Tables

Table

List of Appendices

Appendix

Abstract

DEVELOPMENT OF HIGHLY SENSITIVE AND SELECTIVE OPTICAL AND ELECTRICAL SENSORS FOR MICRO-GAS CHROMATOGRAPHY

by
Karthik Chinna Balareddy

Gas chromatography (GC) is a powerful tool in the analysis of volatile organic compound (VOC) mixtures. It has found applications in healthcare, industrial safety, homeland security, and environmental studies. However to extend its use from lab based to in-situ based applications it is vital to miniaturize the systems to develop so called micro-gas chromatographs (μGC). There are a multitude of issues associated with developing μGC systems. Most of these issues arise from miniaturization of the various components used in GC systems. These issues include the possibility of co-eluting peaks due to the low chromatographic resolution of the short micro-columns used in these systems, the need for long sampling time that is necessary for the detection of low concentration of VOCs, and the presence of dead volumes in the systems that may arise from interconnects and connection ports. Additionally, from a sensing point of view,

many sensors that have been reported are too bulky or fragile for use in portable GC systems, require multiple gas flows, show a lack of uniformity in their sensing responses, or have very long adsorption and desorption times which would preclude their use in µGC. This dissertation presents the development of optical and electrical sensors aimed at alleviating some of these issues, through high sensitivity that will allow for sampling times of these systems to be reduced, analyte pattern analysis from sensing array or multivariable sensing which can be used to identify analytes from an eluted mixture, robust design to withstand use in portable systems and ease of integration with various µGC components.

The first optical sensor developed consists of a polymer sensing film coated on silicon substrate via a variety of methods including, spin coating, drop coating, and spray coating. Several issues with the Fabry-Pérot (FP) are discussed and solved including non-uniformity of responses, reproducibility, dead volumes due to integration, and fabrication of sensor arrays. The sensors showed excellent sensitivity, with detection limits as low as 0.7 pg. An array of these sensors was also demonstrated and showed promise for use in pattern analysis and analyte discrimination.

The second optical sensor characterized, worked on the principle of localized surface plasmon resonance (LSPR). The sensor was shown be capable of differentiating between vapors without the need for an array, i.e. with the use of only a single sensor. However the low sensitivity is still a stumbling block for this type of sensor.

The final sensor detailed within this dissertation is a high frequency graphene field effect transistor sensor (GrFET). The detailed testing results described herein indicate unprecedented sensitivity for a pristine graphene nanoelectronic sensor along with ideal response and desorption times which have not been shown in previous sensors using this material. The sensors were also tested for their response to a series of eluted analytes separated using standard GC techniques.

All three proposed sensors have a small footprint and low power consumption which are critical for μGC applications.

Chapter I

Introduction

1.1 Gas chromatography

Gas chromatography (GC) is a common and powerful technique used in analytical chemistry for the separation and analysis of compounds than can be vaporized without decomposition. Typical uses of GC include testing the purity of a particular substance, or separating the different components of a mixture (the relative amounts of such components can also be determined). In some situations, GC may help in identifying a compound. Additionally GC can be used to prepare pure compounds from a mixture. The most common applications of GC however involve the detection of hazardous or undesirable compounds in areas ranging from environmental, health and industrial monitoring to homeland security. A schematic of a standard GC system is shown in Fig. 1-1.

The GC analysis procedure is as follows. Analytes are sampled using a variety of methods, including but not limited to, Solid Phase Microextraction (SPME), gas syringe, and liquid syringe. The analytes are injected into the GC system via the injection port and vaporized in the injector oven. A portion of this analyte or analyte mixture can be discarded using the GC split system, leaving the remaining portion to be delivered to a downstream capillary column, using an inert gas like Helium or Argon as the carrier. The capillary column can either be uncoated, in which case it is called a guard column or coated with a polymer, called a separation or stationary phase column. The polymer coating (stationary phase) on the interior of the columns serves to separate analytes spatially via a variety of interactions between the analyte and the stationary phase. Depending on the nature of the stationary phase, the analytes can be separated based on their volatilities, polarities, or functional groups. The distal end of column is connected to a detector, most commonly a flame ionization detector (FID)[1-4] or a mass spectrometer (MS).[5,6] However, several other types of detectors have also been used in GC systems including single beam infrared (IR) spectrophotometry,[7,8] ion mobility spectrometry (IMS),[9,10] photoionization detector (PID),[11,12] and surface acoustic wave (SAW).[13,14] The detector outputs a signal each time a analyte is detected in it's vicinity. The analytes which were spatially separated in the column elute out of the column successively and are represented as a chromatogram with a temporal separation between consecutive analytes. Fig. 1-2 illustrates such a chromatogram.

Even though the excellent performance and analysis capabilities of a GC system have made it an industry standard, their large size and high power consumption are less than ideal for rapid *in situ* analysis of volatile organic compounds. In recent years major strides have been made to develop micro gas-chromatograph (µGC) systems to achieve faster, more efficient *in situ* analysis of complex mixtures of volatile organic compounds (VOC).

In this effort several companies have developed smaller versions of a standard GC-MS systems. However, most of these instruments are not mobile or economical enough for truly practical *in situ* monitoring in isolated areas, some of them do not detect a wide range of VOCs, and many of the systems do not possess the sensitivity to detect sub parts per million (ppm) concentrations of analytes.

1.2 Micro gas-chromatography

Since 1979, when the first attempt at a µGC was reported by Stephen Terry at Stanford University (Fig. 1-3), there has been a strong push to miniaturize the various components for VOC analysis.[15,16] The Sandia MicroChemLab program has reported several major developments in regards to µGC systems or micro-machined components including a pre-concentrator, separation columns, and a surface acoustic wave (SAW) sensor.[17,18]

The widespread availability of MEMS fabrication technology, i.e. photolithography, deep reactive ion etching (DRIE), metal deposition, and substrate bonding, has enabled rapid development of µGC components. Over the last 30 years, several reports have been published on µGC components, including micropumps,[19,20] micro-preconcentrators,[21-26] micro-columns,[27-38] micro-thermal modulators,[39-41] and micro detectors.[42-51] However, there are very few reports of integrating all the microfabricated components into a working GC microsystem.

Professor Edward Zellers' group at University of Michigan has been at the forefront of developing MEMS based µGC. In recent work this group has shown the ability for a µGC system to separate and identify explosive markers, schematic shown in

Fig. 1-4. On the front end a hybrid preconcentrator/focuser (PCF) module consisting of a polymer membrane particulate filter, a conventional stainless-steel tube packed with a granular adsorbent, and a 0.41 cm^2 Si/Pyrex microfocuser (μF) chip with an integrated heater and temperature sensor and an reactive ion etched cavity packed with a granular adsorbent was used to trap, sample and inject the sample to be analyzed by the system. A microfabricated Si/Pyrex chip with a 1-m long spiral etched channel, integrated heaters and temperature sensors, and a wall coated stationary phase served as the chromatographic separation microcolumn. A chemiresistor (CR) array detector chip consisting of 4 sensors, each coated with a different thiolate monolayer-protected gold nanoparticle (MPN) interface layers, was used to detect and discriminate the markers. Two mini diaphragm pumps were used along with valves to direct and control air flow; and a scrubber was used to clean the ambient air carrier gas. This system was demonstrated in both a laboratory and during field testing to detect 2,3-dimethyl,2,3-dinitrobutane (DMNB), 2,6-dinitrotoluene (2,6-DNT) and 2,4-dinitrotoluene (2,4-DNT); markers of TNT.[52,53]

Apart from the research and development of μGC systems in laboratories and academics settings, several μGCs have been commercially developed. One such system is the Defiant Technologies Frog-4000.[54] The system uses a trap to collect and inject analytes, a metal microcolumn for separation of analytes and a photoionization detector (PID) as a sensor. A set of diaphragm pumps is used to direct gas flow and ambient air is used as carrier gas. The entire system measures 10 x 7.5 x 14.5 inches and is capable of analyzing a wide range of analytes with boiling points as low as -13.3 ^{o}C and as high as 244.7 ^{o}C. Another example is a device called zNose developed by Electronic Sensor

Technology Inc.[55] It uses a 3 cm stainless steel tube filled with Tenax as the pre-concentrator to trap target analytes from ambient air and inject them into a 1-meter long capillary separation column. After separation, analytes are detected by a SAW sensor. The device has a detection limit of a few pico-grams and is capable of rapid analysis; approximately several minutes. Agilent has also produced their own version of a μGC system; the Agilent 490.[56] It has two independent separation modules, with each having an injection valve. Either a narrow bore or packed separation column can be used, and the eluents from the columns are detected using a thermal conductivity detector. The module can be replaced easily so that customers can choose different modules according to different applications, adding to the systems versatility. The whole system is integrated into a portable size of 28 x 30 x 15 inches and has a detection limit of approximately 1 ppm.

1.3 Components of a μGC Systems

Several components are common to all μGC Systems. Among these components are the preconcentrators/focusers, separation columns, micro-sensors. The increased use of MEMS technologies has spurred rapid development and improvement in performance for these components.

1.3.1 Preconcentrators and focusers

Detection of very low concentrations of VOCs is critical in gas chromatography, however most low power sensor technologies viable for use in μGC are not capable of detecting the parts per billion (ppb) or parts per trillion (ppt) concentrations present in real world settings. To improve the capabilities of µGC systems a method known as preconcentration is used to sample a large volume of ambient air using an adsorbent material to capture analytes and then desorb the analytes into the system, normally through heating of the adsorbent materials.

A standard preconcentrator can be visualized as a tube filled with an adsorbent material to capture analytes present in ambient air. The nature of the adsorbent material and the nature of the analyte determine the extent to which the analyte can be preconcentrated. Polarity of the material and analyte, volatility of the analyte, intermolecular attraction, surface area of the adsorbent materials, and flow rate are some of the factors that determine the extent of adsorption.

Several materials have been proposed for use as adsorbents in preconcentrators. Among the more commonly used are activated carbon,[22,23,57-61] Tenax,[25,61,62] or SPME based adsorption which is reliant on polymers like polydimethylsiloxane (PDMS).[63-68]

Most preconcentrators in use consist of a long metal, glass or ceramic tube packed with adsorbent materials,[68-70] wrapped with a metals like Pt and Ta to heat and thermally desorb analytes from the preconcentrator. Preconcentrators of this design are widely used in µGC development, however there are several disadvantages of this design. Due to their size and shape there are large dead volumes and they possess poor heating efficiency. These issues can cause peak broadening, particularly for less volatile analytes and hence does not work to improve the sensitivity of the system,

To overcome these disadvantages silicon based preconcentrators are being developed by several national labs and research groups. These preconcentrators, fabricated using MEMS technology, are much smaller than the tube based preconcentrators, thereby minimizing dead volumes, power consumption, and thermal mass. In recent years there have been several reports of microfabricated preconcentrators,[23-25] including those used in the µChemLab system developed by Sandia,[17] and the Canary-3 from Defiant Technologies.[71]

Agah *et al.* used high aspect ratio etching of silicon to create pillars which were then coated with Tenax TA. The pillars ensured a high surface area for the design while keeping the thermal mass of the system low, shown in Fig. 1-5. The claimed enhancement factor for these devices was 1000.[26] Kurabayashi *et al*. used a similar approach to but instead of etching pillars within the cavity they used graphitized carbon as an absorbent. The low thermal mass of the device allowed for it to be heated, with a resistive heating element, to 250 ^{o}C in 0.23 seconds with just 1 W of power.[24] A flow rate of over 9 mL/min was achieved with this device. A similar device was shown by C-J Lu *et al* (Fig 1-6). This device measuring 4 mm x 14 mm x 1.1 mm demonstrated a preconcentration factor of 13,637 using *in-situ* grown carbon as an adsorbent.[72] Zellers *et al.* evaluated the performance of multiple designs microfabricated preconcentrators. In this work, four deep-reactive-ion-etched Si micro-preconcentrators packed with commercially available Carbopack X (C-X), were characterized and compared to a capillary preconcentrator-focuser. This work showed that there is a limit to microfabricated preconcentrators miniaturization, below which it is not possible to operate the device at reasonable flow rates. Preconcentration factors ranged from 730 to 39,000 for these devices.[73]

The miniaturization of preconcentrators through MEMS fabrication technology has led to small devices which can be used to inject sharp peaks into the separation columns.

1.3.2 Micro-separation Columns

The first example of a microfabricated separation column integrated in a µGC was reported by Terry *et al.* in 1979. However. this device suffered from poor separation performance and was hence replaced with a conventional capillary column. More recently, due to the increasing demand for further miniaturization of the µGC system the separation columns that could be used were relatively short, leading to attempts to develop better microfabricated columns etched in silicon,[27,28,30-38,74] glass,[75] metal,[54,71,76] or polymer substrates.[77] Several etching techniques have been used to fabricate these columns including deep reactive ion etching (DRIE), and wet chemical etching.

Overton *et al.* reported high aspect ratio, 50µm by 600µm (Fig. 1-7), nickel columns fabricated with LIGA techniques. These columns were demonstrated to separate a mixture of 7 analytes in about 4 s.[76]

Kolesar *et al.* developed a µGC system with an etched silicon micro column. The column coating, copper phthalocyanine, was deposited and patterned directly along a 300 µm wide by 10 µm deep, 0.9 m long micromachined channel. This system was capable of separating ammonia and nitrogen dioxide in 30 minutes. The slow separation was not considered ideal for realistic µGC applications. The µGC system developed by Sandia National Labs used a spiral microfabricated silicon column. The columns measured 100 µm wide by 400 µm deep and about 85 cm in length. These columns were shown to separate 6 analytes in less than 1 minute.[74]

Frye-Mason *et al.* at Sandia demonstrated a parylene microcolumn. The column was fabricated by deposition of parylene on an etched silicon wafer, a glass wafer was subsequently bonded to the parylene coated silicon wafer and finally the silicon was etched away with KOH. The column fabricated by them was 1-m-long with a spiral structure, a rectangular cross section (100- m wide, 350- m high), and was demonstrated to have a much faster heating and cooling time than silicon-glass columns as well as lower power consumption.[77]

Glass microcolumns were demonstrated by Lewis *et al.* The microcolumns were fabricated by etching two glass substrates using lithography, metal deposition and hydrofluoric acid. The rounded features, shown in Fig.1-8, produced by this method are more desirable than the rectangular cross section of the silicon and metal columns. The column was integrated with a photoionization detector and demonstrated the ability to separate the components of a BTEX mixture in 235 s.[75]

Work at the University of Michigan Wireless Integrated Micro Systems and Sensors center has been at the forefront of µGC development including the development of silicon microcolumns. The standard design consists of a 150 µm wide by 240 µm deep rectangular column, and the length of the column could be varied from 25 cm to 3m. The footprint for the columns was minimized by using a double square spiral geometry. The channel is anodically sealed with a Pyrex wafer with heaters and temperature controllers patterned on the back using standard metal deposition, lithography and lift-off techniques, refer to Fig 1-9. Columns can be coated with a variety of stationary phases using a static coating method. Sacks *et al.* demonstrated 12,000 theoretical plates with a 3 m column with air as a carrier gas (4000 plates/m). The work also reported the separation of 30 analytes in under 5 minutes with temperature programming. Additionally these columns were shown to separate n-C_5 to n-C_{15} mixture in 12 s.[30]

Recently Agah *et al.* demonstrated semipacked silicon based microcolumns. Similar in design to the columns fabricated at the University of Michigan, these columns however have posts/pillars in the flow channel, as seen in Fig. 1-10, to maximize contact area between the analyte mixture and the stationary phase. This design was found to have height-equivalent-to-a-theoretical-plate (HETP) of 15,000 plates/m.[78] This research group also developed a method to use thiolates as a stationary phase, demonstrating a HETP of 7300 plates/m and the capability of changing the thiol as desired while also coating selected areas of the column leaving other areas bare.[79]

1.3.3 Sensors

Chemical sensors can be broadly classified into two types; 1. destructive sensors and 2. non-destructive sensors. Destructive sensors are termed as such due to their detection mechanism which leads to destruction of the analyte sample. Destructive sensors can use the entirety of the sample to build a signal, which leads to them being extremely sensitive, however, no downstream analysis can be done due to this.

Several destructive sensors have been proposed for use in gas chromatography. The gold standard for analyte detection is the FID, which is used in almost all bench top GC systems as well as a reference for characterizing other sensing methods. The FID was invented in 1957 by scientists at the Commonwealth Scientific and Industrial Research

Organisation. The FID works by measuring conductivity changes due to the presence of ions formed while burning organic compounds. The FID is generally considered quite easy and cheap to manufacture as well having a wide detection range (10^6). In more recent years several research groups have reported the development of micro-FIDs for use in portable gas chromatographs.[80-83] These micro-FIDs are generally fabricated using patterned Pyrex, silicon or polytetrafluoroethylene (PTFE). However, as shown in Fig. 1-11 all FIDs require multiple gas flows to function and are unable to distinguish between VOCs.

Mass spectrometry (MS) is another detection method that is commonly used in bench-top GCs. An MS produces spectra of the masses of molecules that comprise an analyte. The spectra give insight into the composition of the material and can hence be used to determine the nature of an unknown material. An MS generally consists of three components, an ionizer/ion source, a mass analyzer, and a detector. The ionizer converts the sample into ions, through a variety of methods including inductively coupled plasma, glow discharge, field desorption, fast atom bombardment, etc. The ions are extracted from the sample and separated based on their mass-to-charge ratios by the mass analyzer and finally the detector/detectors measure the abundance of each ion present. Martin *et al.* were the first to report the use of mass spectroscopy with gas chromatography in 1952. Since then the MS has become a common and popular detector for VOC analysis due to it's ability to provide both quantitative and qualitative information about a analyte in a VOC mixture. To date MS detectors haven't been miniaturized sufficiently for use in portable or micro-gas chromatography.

Other less common destructive sensors include flame photometric detector which burns the sample using a hydrogen flame and measures the characteristic wavelengths which are emitted by the excitation of certain elements or compounds in the sample, e.g. phosphorus emits at about 510-536 nm and sulfur at 394 nm.[84,85] The atomic emission detector uses microwaves to generate a plasma and decompose the analytes. The atomic emission spectra from the decomposed elements can be measured to identify the analyte.[86-88]

Compared to destructive sensors, non-destructive sensors are garnering far more interest in the field of µGC. Non-destructive sensors are particularly useful for building arrays of sensors, performing 2-D chromatography, and on column measurements of analytes mixtures. Numerous methods of detection have been proposed and can be broadly classified into three types; 1. acoustic sensors, 2. electrical sensors, and 3. optical sensors, each with their own merits and demerits.

The most common type of acoustic sensor is the surface acoustic wave (SAW) sensor. SAW sensors have been used for several decades to detect analytes and several portable sensing systems have employed them recently.[17,55,71,89] As shown in Fig 1-12 the standard SAW sensors consists of a piezoelectric substrate with several electronic components patterned on it. A input interdigitated transducer (IDT) and output IDT are spatially separated on the substrate and the space between them is the surface across which the acoustic wave propagates. An alternating current is used to drive the input IDT and the ensuing stress and strain on the piezoelectric substrate creates mechanical waves which propagate across the delay line to the output IDT. The synchronous frequency, which can be expressed in terms of the phase velocity v_p and pitch p as shown below, can be measured.

$$f_0 = \frac{v_p}{p}, \tag{1.1}$$

When a mass is added to the delay line through adsorption of analytes the phase velocity is affected as per the following equation

$$v_p \propto \sqrt{\frac{E}{\rho}}, \tag{1.2}$$

where E is the Young's modulus of the material and ρ is its density. Thus, the addition of mass to the sensor will decrease the phase velocity making it an effective quantitative sensor. SAW sensors have been shown to be sensitive to all analytes with detection limits as low as 10 pg and rapid detection speeds.[90] To achieve qualitative sensing SAW sensors arrays have been proposed. By coating a sensor with a specific polymer the adsorption of certain analytes can be increased in comparison to other analytes. By aligning 3 or more sensors coated with different polymers, it is possible to build response patterns which can be used to identify analytes.[44,91-94] However due to the sensing mechanism of the SAW sensor there is a high possibility of interference between adjacent sensors.[44,92] Quartz crystal microbalances are an example of SAW sensors that are used in gas chromatography.[95,96]

Roukes *et al.* demonstrated a NEMS resonator fabricated on a silicon substrate for VOC detection. This sensors work on a similar principle to the SAW sensor, where addition of mass to the system causes a change in characteristic resonant frequency of the system. This sensor was shown to have a theoretical detection limit of about 1 attogram, however practically it is closer to 1 ng, and is capable of rapid detection of separated analyte mixtures.[97,98]

Several electrical sensors have also been proposed for detection of VOCs. All electrical sensors work on the principle of change in the resistivity or electrical conductivity of a conducting film upon the addition of a analyte to it. The addition of an analyte to the electrical film changes the dielectric constant, the size/shape of the medium and/or the number of charge carriers in the film. Several materials have been used as a medium in electrical sensors including carbon black,[99-101] monolayer protected nanoparticles (MPN),[42,43,102] electrically conductive polymers,[103-105] carbon nanotubes,[46,106-108] and graphene.[51,109]

Zellers *et al.* have pioneered the use of gold MPNs as a conductive film in electrical chemical sensors.[42,110] Gold nanoparticles coated with a monolayer of thiol form an effective conducting film between two electrodes. The MPNs are pushed apart due to the adsorption of analytes. The increase in inter-nanoparticle distance increases the resistivity of the electrical film, additionally the presence of the analytes between these nanoparticles changes the dielectric constant of the film thereby leading to a change in the current measured at the output. By coating the gold MPNs with different thiols it is possible to develop sensor arrays for qualitative detection of VOCs (Fig. 1-13). These arrays have been extensively deployed in the µGC systems being developed at the University of Michigan.[52]

Judy *et al.* demonstrated the use of carbon black as an electrical sensor. Here carbon black was used as the conductive film and adsorption of the analytes leads to a change in the measured current.[101] Such sensors have been shown to have detection limits as low as 0.3 ppm and have been used in the electronic nose developed by the Jet Propulsion Lab in Pasadena.[100]

Novel materials like CNTs and graphene have lead to another avenue of research in chemical sensors (Fig. 1-14). Several groups have worked on the development and characterization of CNT and graphene based sensing schemes. In general these sensors have a DC voltage applied across a CNT or graphene medium; analytes bond to the medium, and charge transfer between the analyte and CNT/graphene leads to a change in its resistivity which can be measured as a change in current. The sensing mechanism is enhanced by defects sites and impurities which promote the bonding of analytes to the medium.[111] A major consequence of this method is the inability to desorb the analytes in a timely fashion rendering them impractical for µGC applications.

Clarici *et al.* were the first to show the use of a photoionization detector (PID) with gas chromatography.[112] A PID uses high energy light, usually ultraviolet rays to ionize the molecules into positively charged ions. The resulting gas becomes electrically charged and the change in electric current is measured as the detection signal. It is possible for the ions to recombine with the electrons to reconstitute the gas, making it a non destructive sensing method. Also, the volume of the sample that is ionized is insignificant compared to the total volume. Issues arise when compounds like methane or water are present which absorb UV rays without ionizing.

Thermal conductivity detectors (TCD) have been used for several decades in GC. Due to their ease of fabrication and small size they are being investigated a prime candidate for use in µGC including monolithic integration of columns and sensors (see Fig. 1-15).[113-115] TCDs consist of an electrically heated filament in a fluidic system.

Under constant flow of a carrier gas the voltage remains constant. When an analyte is introduced to the system, causing a change in the thermal conductivity of the effluent, the filament temperature goes up, thereby changing resistance. A common setup used to measure this change is the Wheatstone bridge. A reference filament which isn't subject to the analyte is used to measure the voltage change in the filament subjected to the analyte. Detection limits can be as low as 20 pg.[116]

Optofluidic ring resonators (OFRR) are a promising technology for chemical sensing. Fan *et al.* demonstrated a novel approach by using pulled capillaries coated with polymers to detect analytes.[49,117,118] The resonant wavelength of an OFRR is given by,

$$\lambda = \frac{2\pi r n_{eff}}{m}, \qquad (1.3)$$

where r is the radius of the resonator, n_{eff} is the effective refractive index (RI) as experienced by the evanescent field of the optical mode, and m is an integer. The evanescent field of the resonant light reaches several hundred nanometers into the surrounding medium; normally a polymer coating in the case of chemical sensors. When an analyte is adsorbed by the polymer the effective RI of the medium is changed which leads to a change in the resonant wavelength of light propogating in the resonator. The ring resonator has been shown to have good sensitivity with detection limits less than 1 ng. The sensitivity of the resonator is dependent on the Q-factor (Q); a higher Q-factor leads to an increased light analyte interaction length (L_{eff}) as shown below,

$$L_{eff} = \frac{Q\lambda}{(2\pi n)}, \qquad (1.4)$$

where Q is the Q-factor and n is the RI. OFRRs were also shown to be capable of acting as a separation column, with the polymer coating behaving as a stationary phase and as a sensor simultaneously.[118] However, due to reproducibility issues and lack of robustness, to date no integration of OFRRs with µGC systems has been attempted. Recently Zellers *et al.* have demonstrated the fabrication of silicon based µOFRRs.[119] These chip based sensors show promise for integration with MEMS based µGC systems, due to their excellent reproducibility and compatibility with other silicon based components (see Fig. 1-16).

Another set of optical sensors which are being investigated are the plasmonic sensors. Potyrailo *et al.* demonstrated the use of the plasmonic structure of morpho-butterfly wings to observe unique changes in the localized surface plasmon resonance spectrum (LSPR) for each analyte.[120] However, the use of butterfly wings is not practical and gold MPNs have been gaining traction as substitutes for use in plasmonic sensing. Several groups have demonstrated plasmonic sensors using gold MPNs however detection limits remain non ideal.[121-123]

Grating structures form a broad group of optical sensors, with many different types being employed such as 2-D diffraction gratings,[50,124] fiber Bragg gratings,[125-127] long period gratings,[128,129] *etc*. Bailey *et al.* demonstrated the use of 2-D polymer diffraction gratings as a chemical sensor. The polymer gratings were fabricated using the capillary effects of a PDMS mould placed on glass. The mould ensured the deposition of the polymer in a desired pattern. The resulting grating is shown in Fig 1-17. For the design shown by Bailey *et al.* the diffraction efficiency at any point i.e. diffraction spot 1,0 can be simplified as follows,

$$\eta_{1,0} = 0.1012\left(\frac{\pi d}{\lambda \cos\theta}\right)^2 \left[(\Delta n)^2 - (\Delta k)^2\right], \qquad (1.5)$$

where λ is the wavelength of light d is the thickness of the grating, n is the real part of the RI and k is the imaginary part of the RI. k can be expressed as:

$$k(\lambda) = \frac{2.3\lambda A(\lambda)}{4\pi d}, \qquad (1.6)$$

where $A(\lambda)$ is the wavelength dependent absorbance. Any change in thickness or refractive index of the polymer grating in the presence of an analyte results in a change in intensity of the diffracted beam at a specified point. The detection limits demonstrated by these sensors was as low as 7 ppm, however they have never been tested under pulsed flow conditions.

Long period and Bragg gratings are not considered viable for μGC because of their complex fabrication and fiber based sensing technique. Additionally, most work based on these sensors have not shown a strong capability to detect VOCs of interest.

Another type of optical sensor used for chemical sensing is the Fabry-Pérot (FP) sensor. This sensing scheme will be discussed in detail in the following chapters.

1.4 Thesis goals

The major goal of this thesis is to investigate the feasibility of several different types of sensors and make significant contributions in the development of these sensors for use in portable vapor sensing systems.

There are several challenges associated with the development of μGC systems. The low power requirements and small system size places a large number of constraints on the design of various components for use in μGC.

To date there has been very little progress in the development of optical sensors for use in μGC. This can be attributed to a variety of reasons including the bulky sensing mechanisms, fragile nature of fibers, and the lack of reproducibility in the fabrication of such sensors, as well as the non-uniformity in responses between sensors of the same type.

On-chip FP sensors might present an attractive optical scheme for use in µGC. The use of silicon substrate will increase the ease of integration with other microfabricated GC components, and the robust design and small footprint should be beneficial over other optical sensing schemes.

The following are the goals of the work on FP sensors;

1. Fabricate and characterize spin-coated FP sensors using several different polymers. Optimize the optical setup to achieve ideal sensitivities and detections limits, while identifying the most important factors that influence the detection limits and sensitivities.
2. Design and fabricate arrays of FP sensors to discriminate between vapors in a mixtures. Identify methods to fabricate and implement them efficiently.
3. Develop a method to negate the non-uniformity of sensor responses which may arise from differences in polymer thickness or incident angle.

LSPR based sensing holds great potential for use in achieving selectivity of analytes without the need for an array of sensors, making them even simpler to implement in portable GC systems.

The goal of the studies on LSPR sensors are;

1. Provide proof of sensor selectivity using gold nanoparticles coated with mono layers of C8 thiol.

2. Simplify the optical setup needed to perform such measurements, precluding the need for spectrometer based optical sensing schemes.

While optical sensors show potential for use in µGC, electrical sensors are more easily implemented in such systems. Recent increases in research on carbon nanotubes and graphene has led to their use as vapor sensors; however the DC sensing system used is too slow to be effective in gas chromatography, with desorption taking several hundred seconds.

Using a high frequency sensing scheme which is dependent on rapid dipole oscillations and not slow charge transfer mechanics would be ideal for use in vapor sensing.

The goals of the work on graphene sensors are;

1. Characterize a high frequency graphene-field effect transistor, with a variety of analytes and compare the responses to those provided by an FID.
2. Demonstrate the rapid detection of a mixture of analytes separated using GC stationary phase columns.

1.5 Thesis outline

This dissertation is divided into eight chapters. Chapter I gives an overview of current status of µGC and the important components that comprise a µGC system, including preconcentrators, separation columns and sensors. Chapters II through V are based on work done with on-chip FP sensors, including multiplexing, optical optimization, and integration with µGC components. Chapter VI discusses the proof of concept work done on LSPR sensors, and the ability to differentiate between analytes based on the response spectrum. Chapter VII presents the work on development of a novel high frequency graphene transistor sensor. The final chapter, Chapter VIII, concludes the contribution of the work and discusses the future work on sensors and systems.

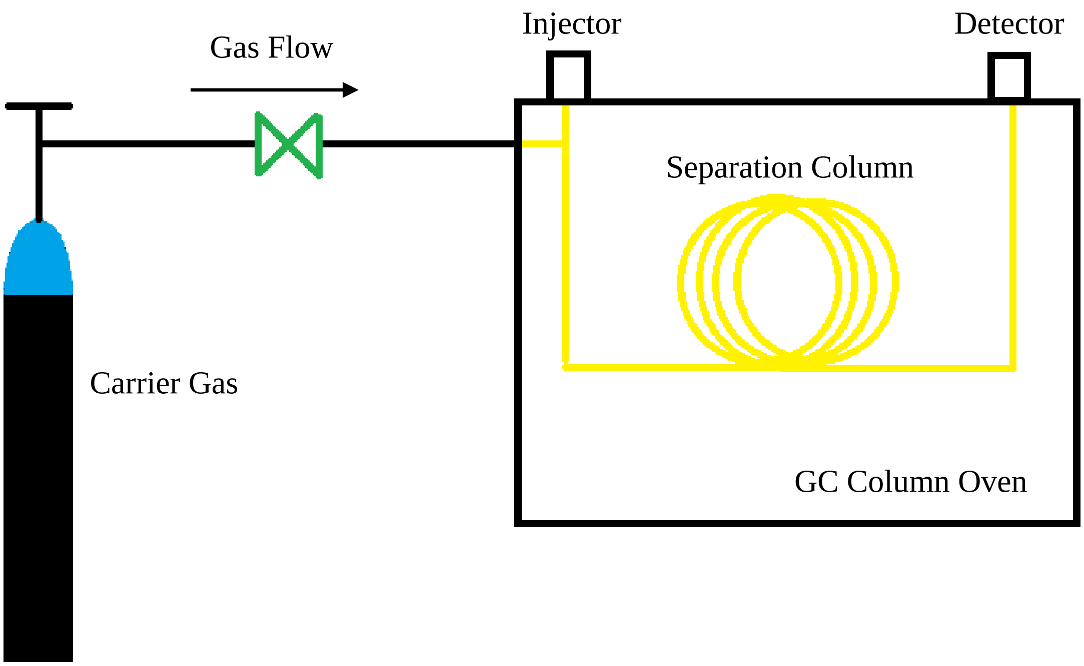

Figure 1-1 Schematic of a typical bench-top GC system.

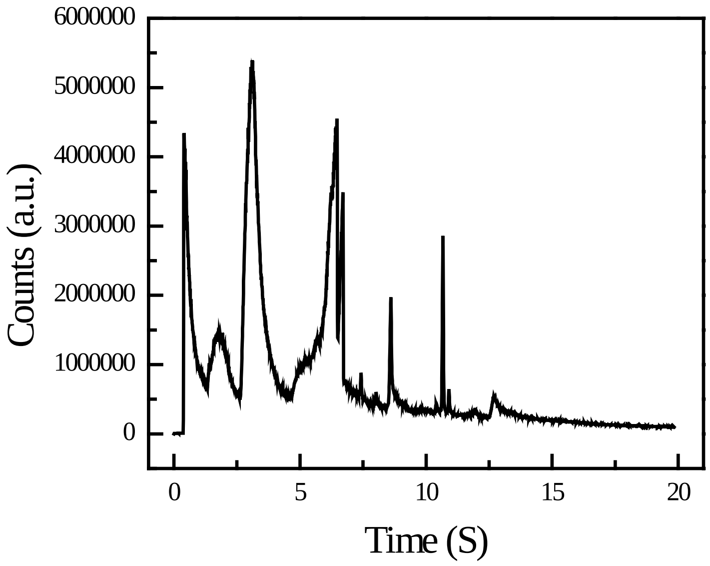

Figure 1-2 Output chromatogram obtained from a GC-MS system.

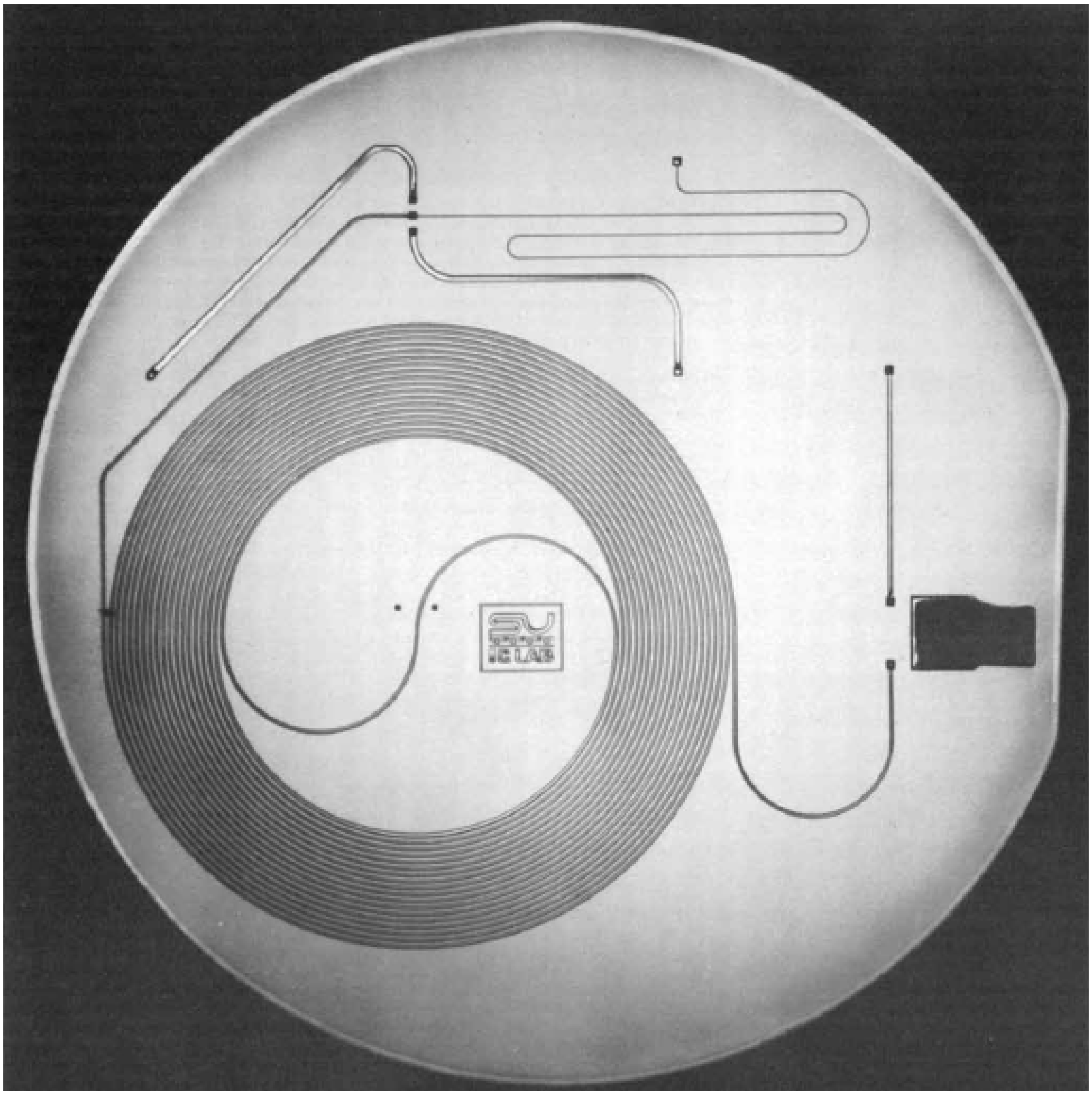

Figure 1-3 Silicon based air analyzer developed by *Terry et al.* Reprinted with permission from [16]. Copyright Elsevier.

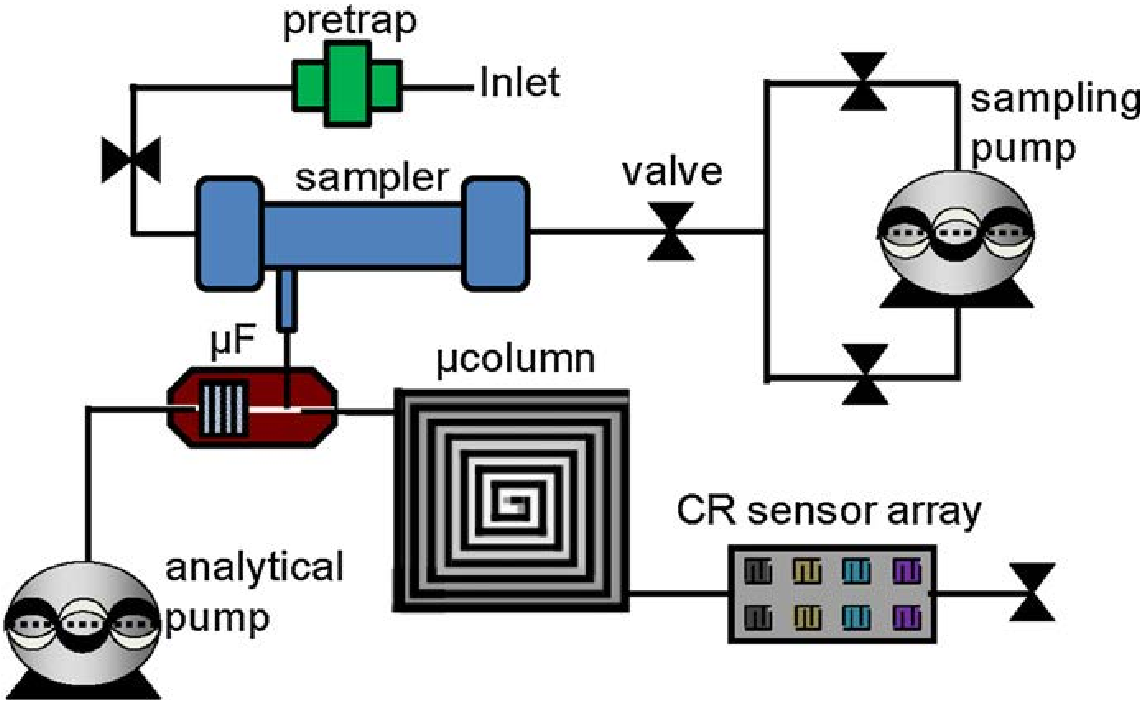

Figure 1-4 Schematic of µGC developed by Zellers *et. al.* Reprinted with permission from [53]. Copyright Elsevier.

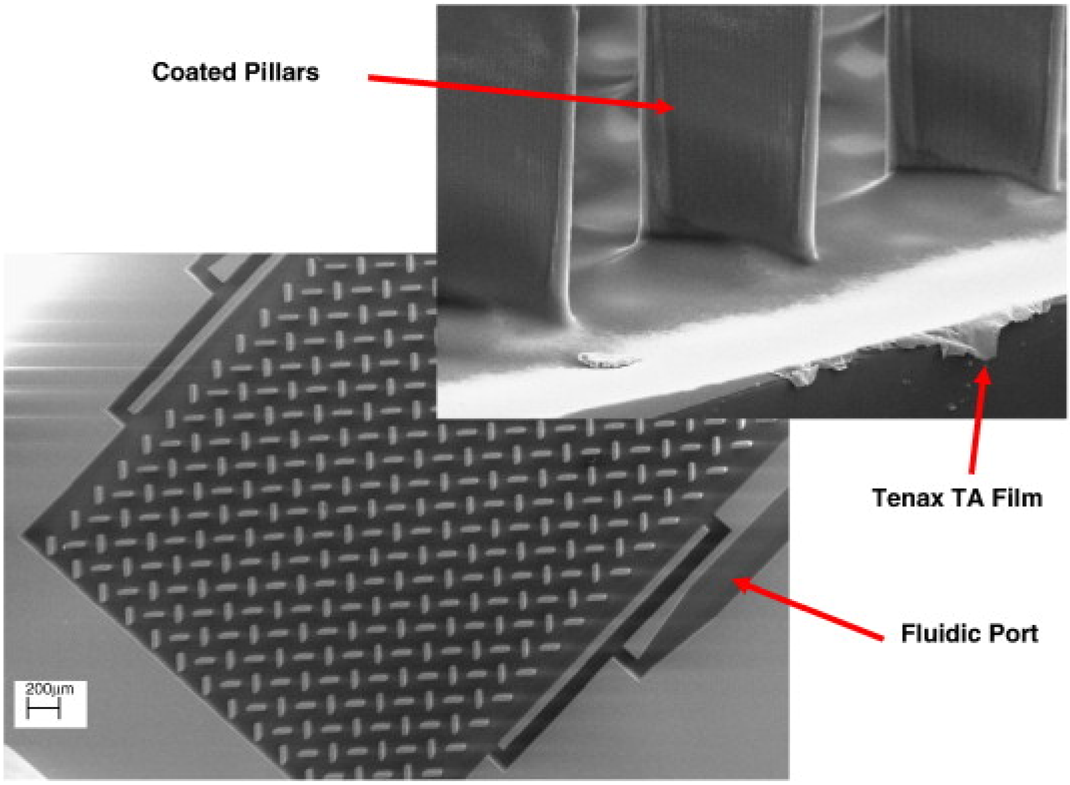

Figure 1-5 SEM image of micro-preconcentrator developed by Agah *et al.* Reprinted with permission from [26]. Copyright Elsevier.

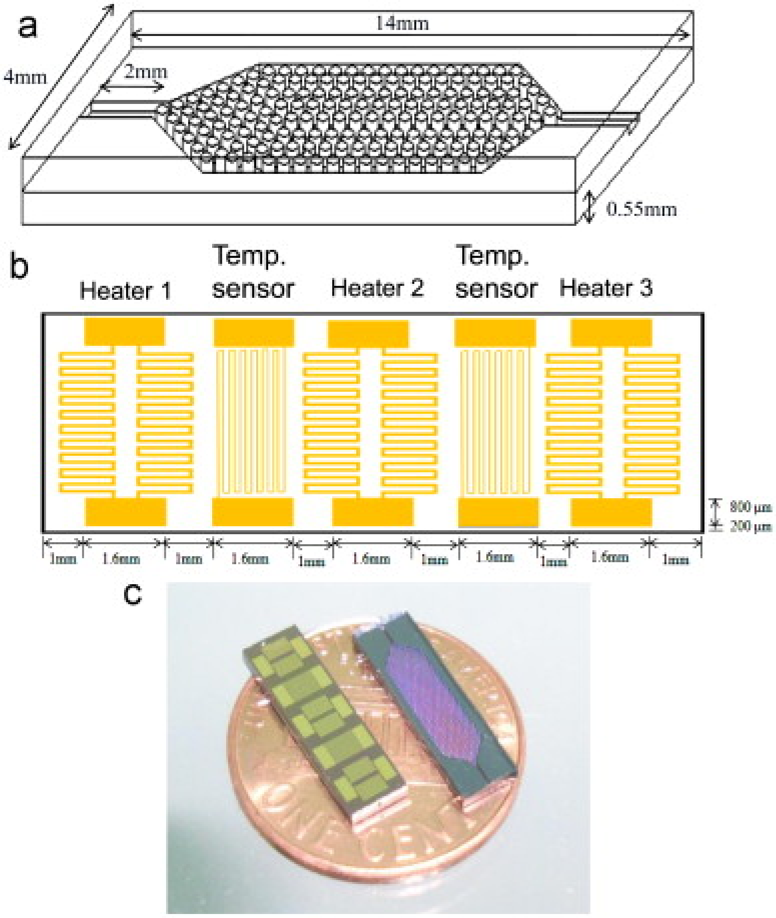

Figure 1-6 Schematic, design and image of multistage stage preconcentrator developed by C-J Lu *et al.* Reprinted with permission from [72]. Copyright Elsevier.

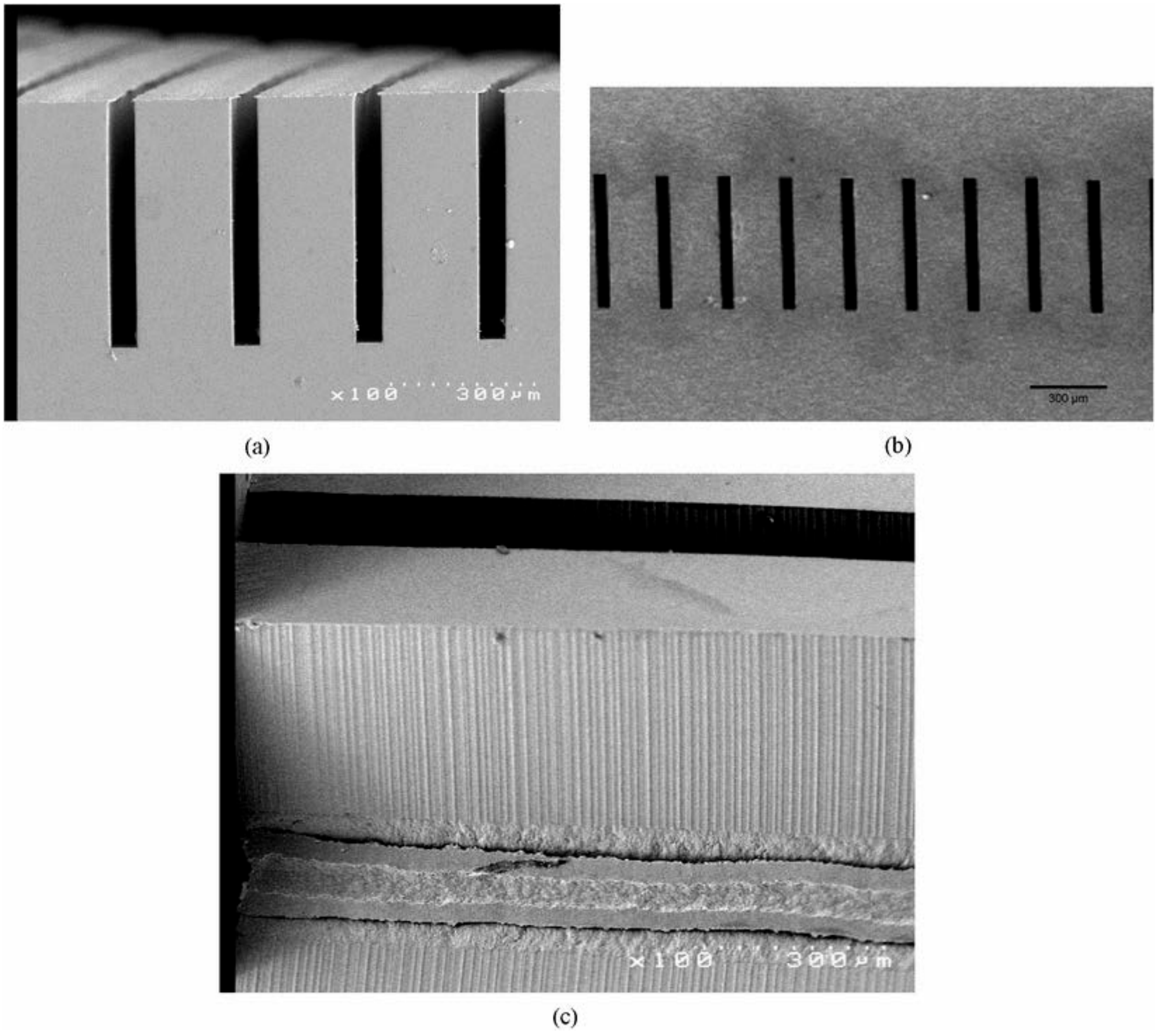

Figure 1-7 SEM of nickel aspect ratio columns. Reprinted with permission from [76]. Copyright 2007 IEEE.

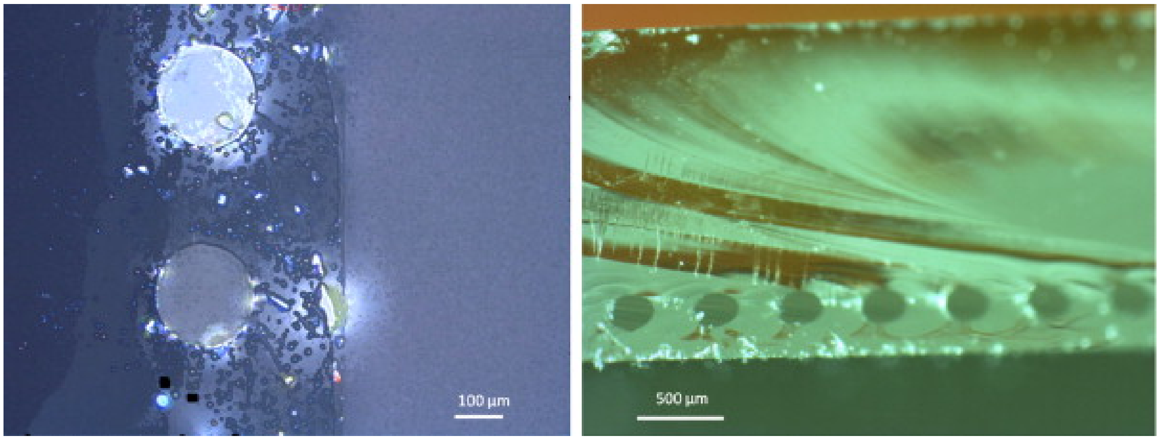

Figure 1-8 SEM image of circular glass micro-columns. Reprinted with permission from [75]. Copyright Elsevier.

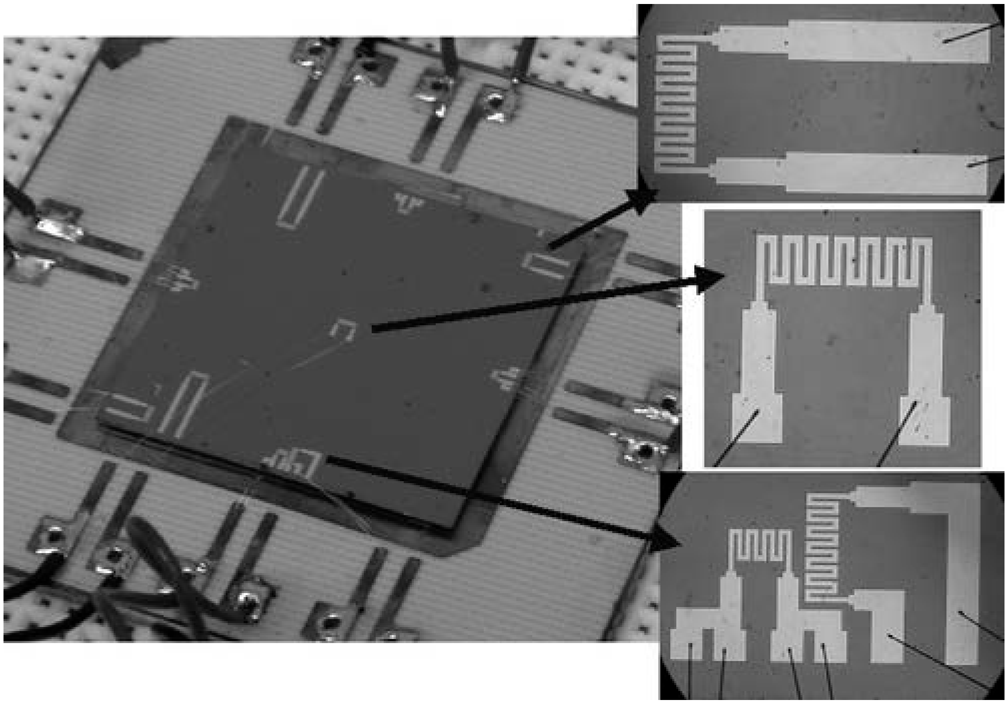

Figure 1-9 Optical image of micro-heaters on a silicon microcolumn. Reprinted with permission from [30]. Copyright 2007 American Chemical Society.

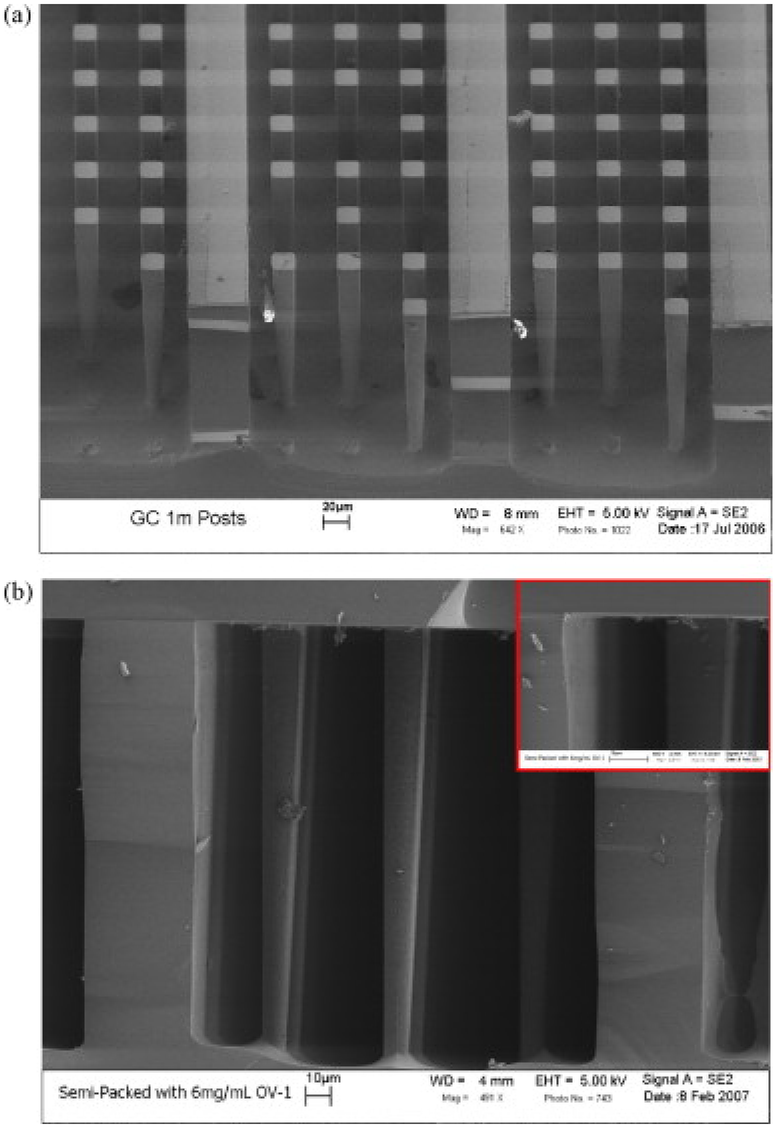

Figure 1-10 SEM of semi packed columns. Reprinted with permission from [78]. Copyright Elsevier.

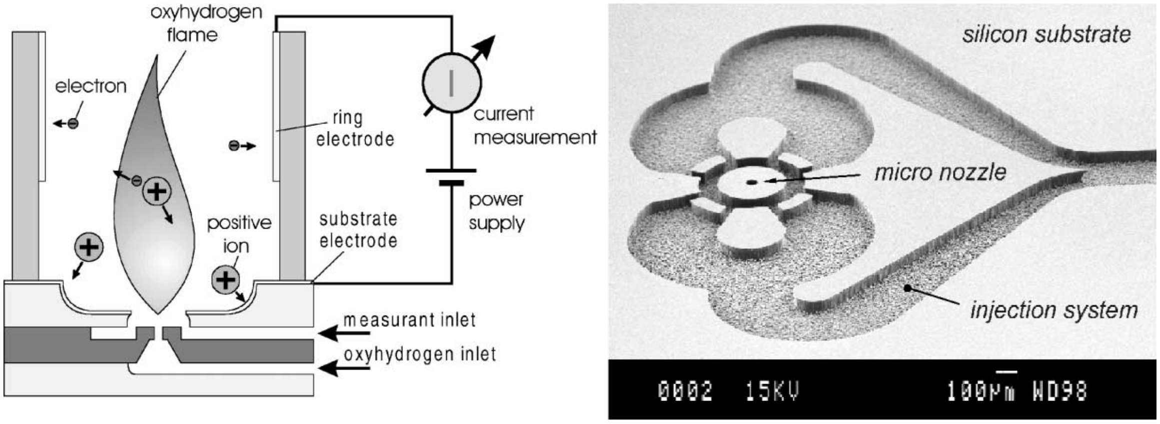

Figure 1-11 Schematic and SEM of a µFID illustrating the fluidics required. Reprinted with permission from [81]. Copyright Elsevier.

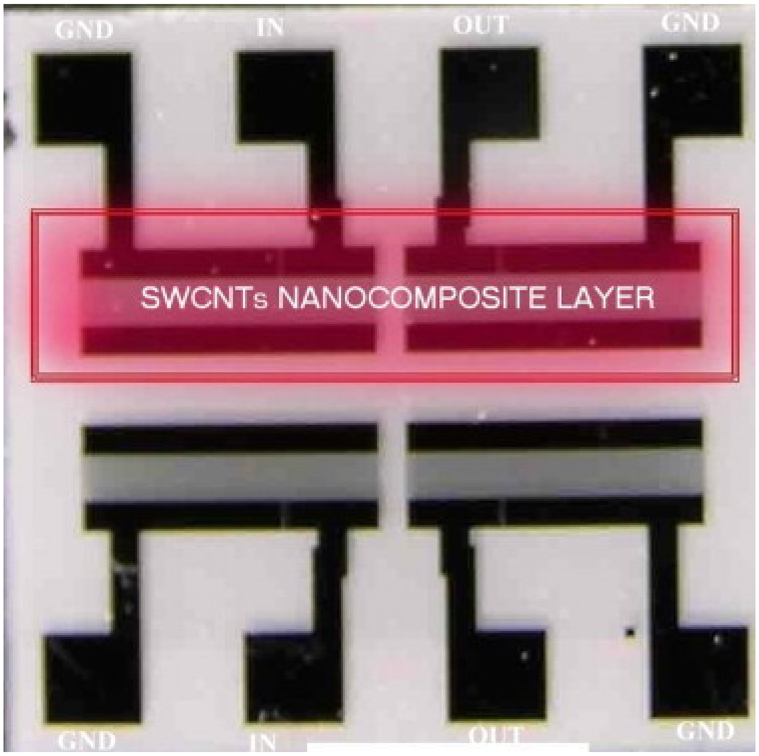

Figure 1-12 Image of two SAW sensors with carbon nanotube piezoelectric delay line. Reprinted with permission from [89]. Copyright Elsevier.

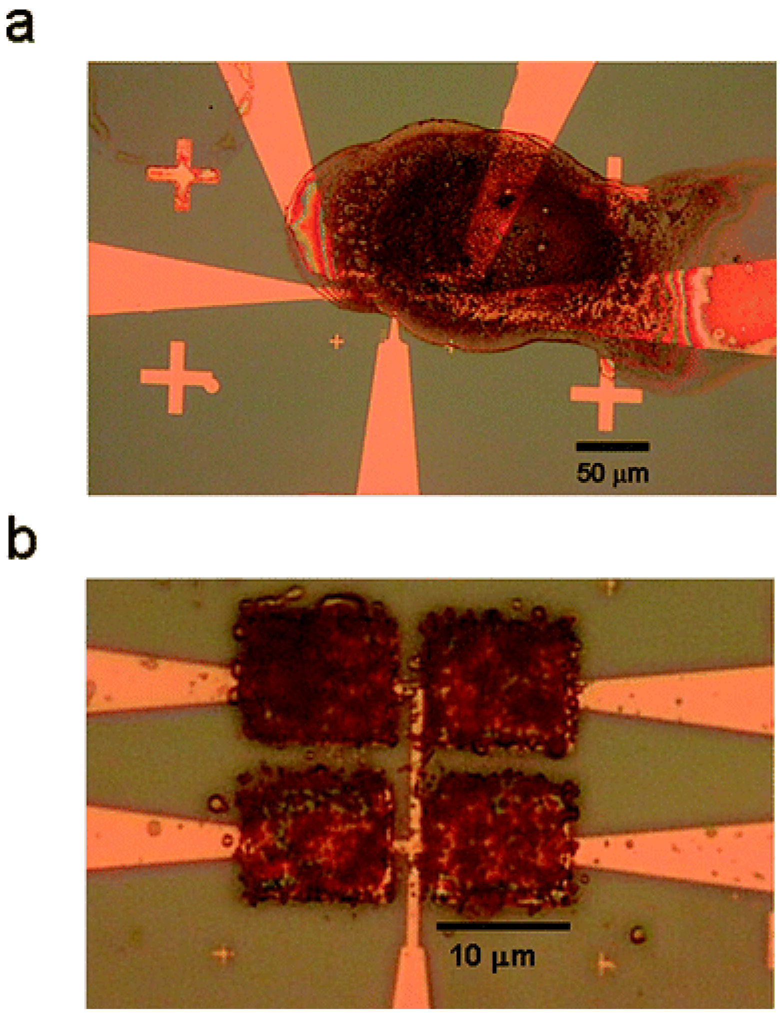

Figure 1-13 Optical micrograph of MPN coated chemiresistors. Reprinted with permission from [110]. Copyright 2011 American Chemical Society

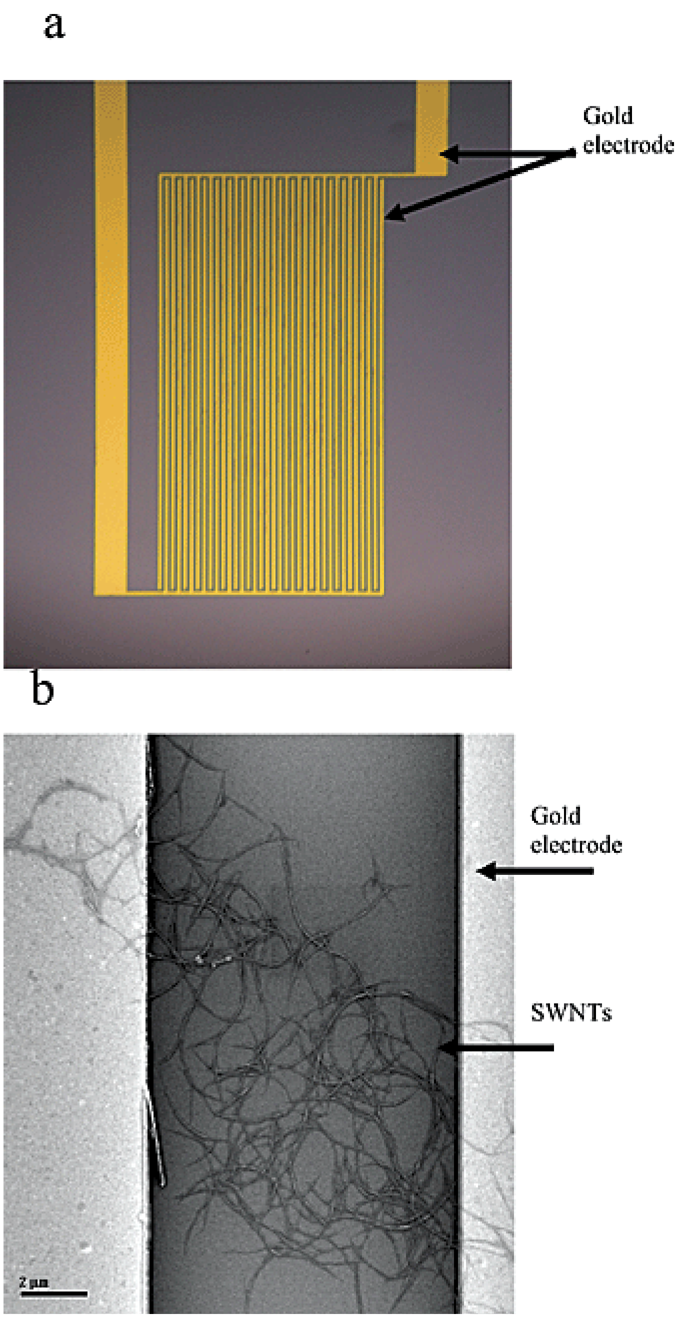

Figure 1-14 Optical and SEM micrographs of single wall carbon nanotube electrical sensors. Reprinted with permission from [46]. Copyright 2003 American Chemical Society.

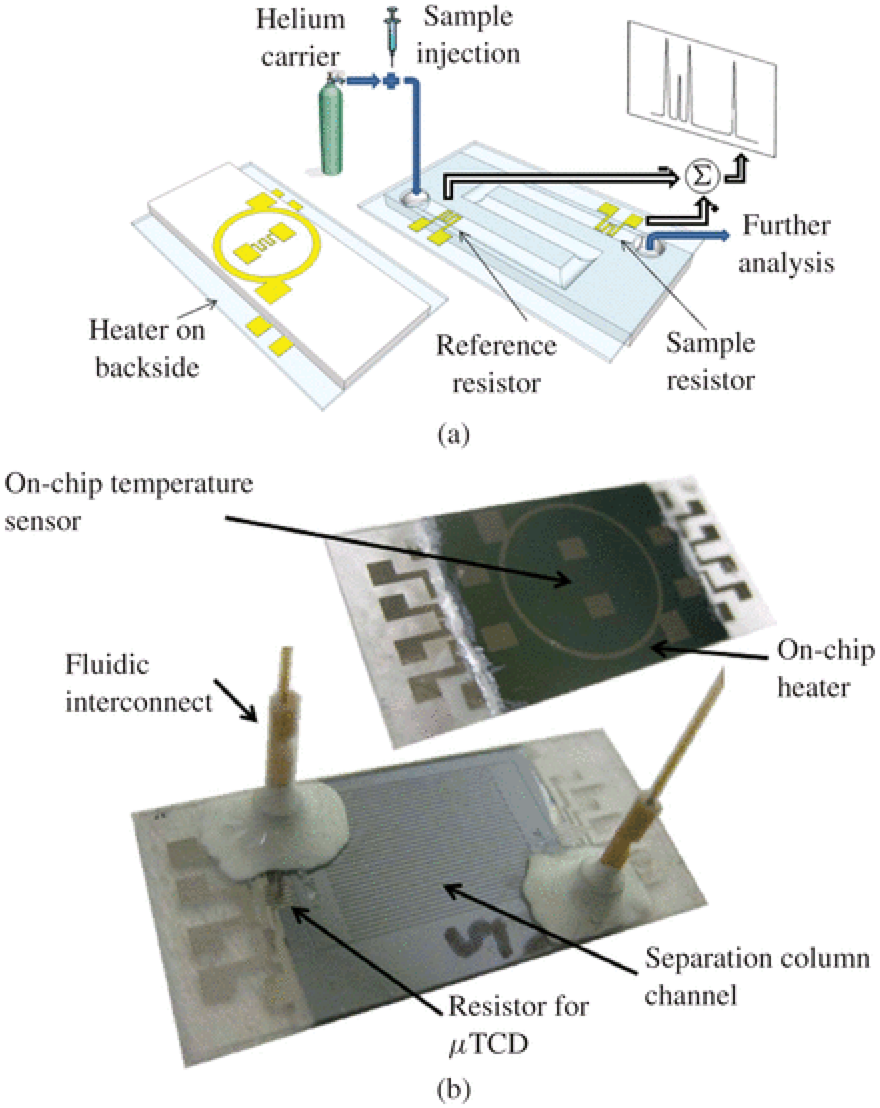

Figure 1-15 Schematic and optical image of separation column with integrated TCD detector. Reprinted with permission from [111]. Copyright 2011 IEEE.

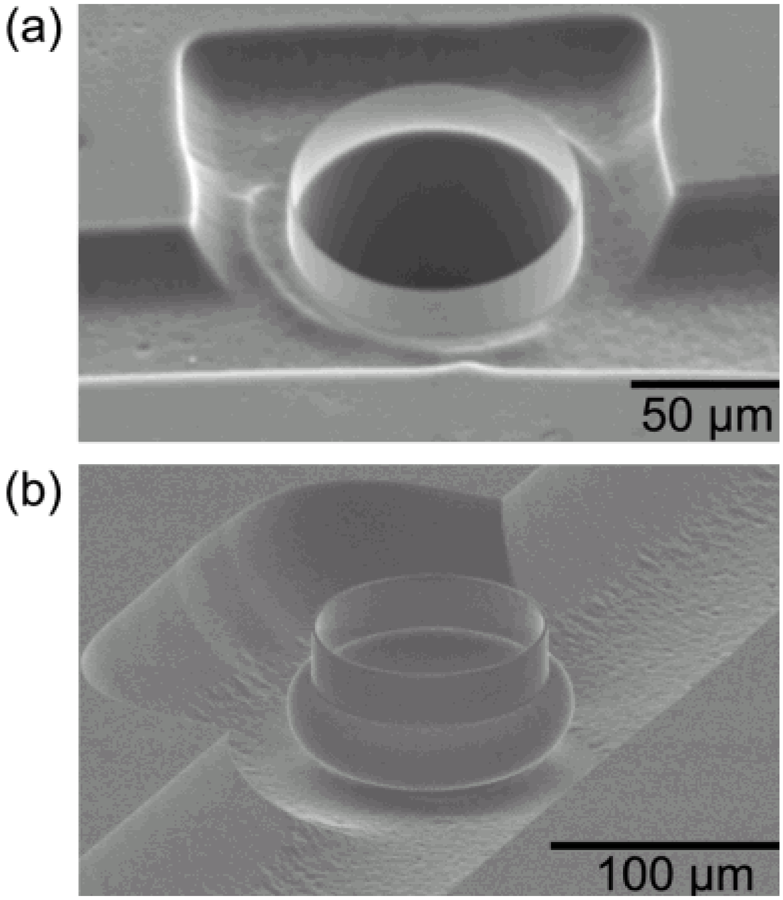

Figure 1-16 SEM image of a µOFRR. Reprinted with permission from [119]. Copyright AIP publishing.

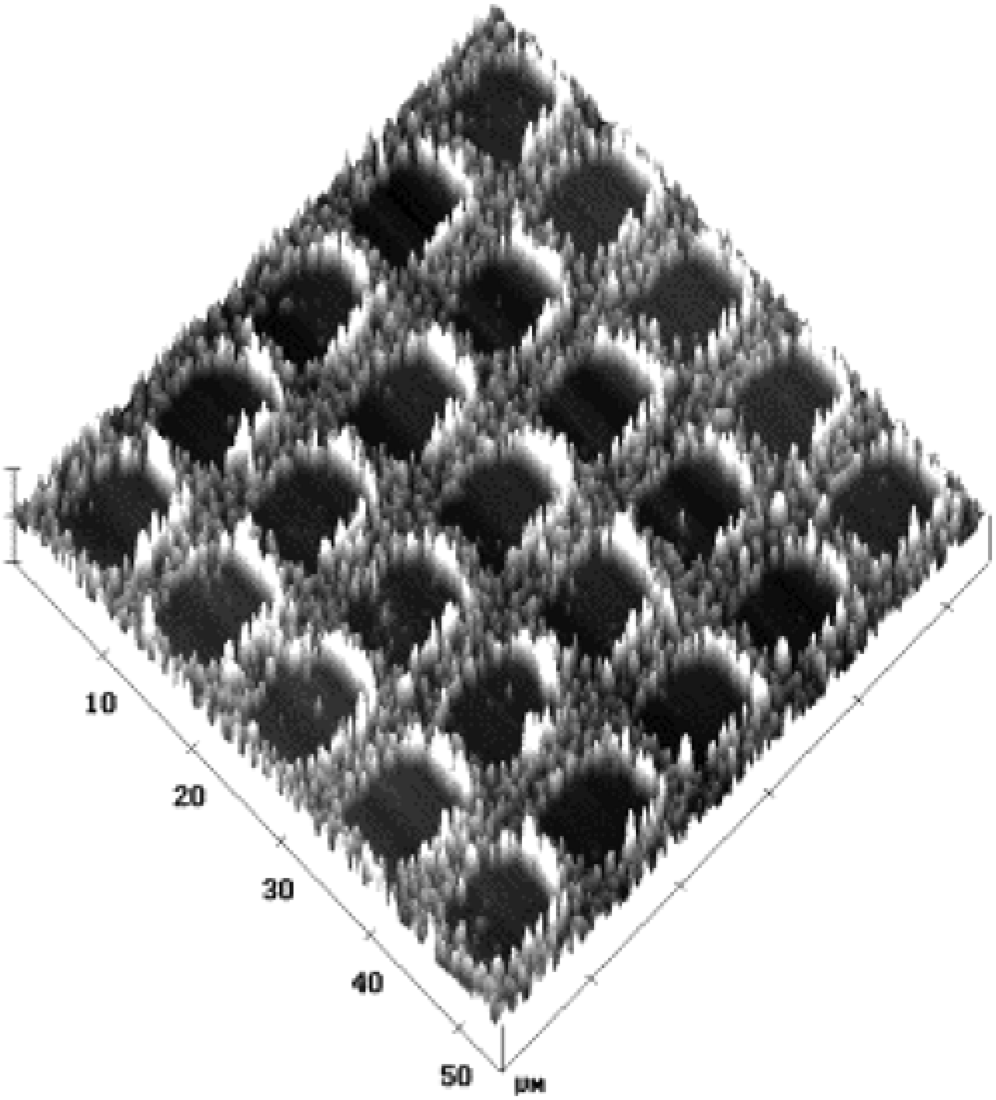

Figure 1-17 Grating structure used as a chemical sensor. Reprinted with permission from [50]. Copyright 2003 American Chemical Society.

References

1. I. G. McWilliam and R. A. Dewar, *Nature*, 1958, **181**.
2. J. Harley, W. Nel and V. Pretorius, *Nature*, 1958, **181**, 2.
3. K. Porter and D. H. Volman, *Anal. Chem.*, 1962, **34**, 748-749.
4. A. Sarafraz-Yazdi, A. H. Amiri and Z. Es'haghi, *Chemosphere*, 2008, **71**, 671-676.
5. D. W. Potter and J. Pawliszyn, *J. Chromatogr. A*, 1992, **625**, 247-255.
6. Y. Masada, *Analysis of essential oils by gas chromatography and mass spectrometry*, 1976.
7. M. P. Fuller and P. R. Griffiths, *Anal. Chem.*, 1978, **50**, 1906-1910.
8. M. D. Erickson, *Appl. Spectrosc. Rev.*, 1979, **15**, 261-298.
9. R. G. Ewing, D. A. Atkinson, G. A. Eiceman and G. J. Ewing, *Talanta*, 2001, **54**, 515-529.
10. M. A. Baim and H. H. Hill, *Anal. Chem.*, 1982, **54**, 38-43.
11. P. J. Hobbs, T. H. Misselbrook and B. F. Pain, *J. Agr. Eng. Res.*, 1995, **60**, 137-144.
12. M. L. Langhorst, *J. Chromatogr. Sci.*, 1981, **19**, 98-103.
13. H. Wohltjen and R. Dessy, *Anal. Chem.*, 1979, **51**, 1465-1470.
14. C. G. Fox and J. F. Alder, *Analyst*, 1989, **114**, 997-1004.
15. S. C. Terry, J. H. Jerman and J. B. Angell, *IEEE T. Electron Dev.*, 1979, **26**, 1880-1886.
16. J. H. Jerman and S. C. Terry, *Environ. Int.*, 1981, **5**, 77-83.
17. P. R. Lewis, R. P. Manginell, D. R. Adkins, R. J. Kottenstette, D. R. Wheeler, S. S. Sokolowski, D. E. Trudell, J. E. Byrnes, M. Okandan, J. M. Bauer, R. G. Manley and C. Frye-Mason, *IEEE Sens. J.*, 2006, **6**, 784-795.
18. R. P. Manginell, P. R. Lewis, D. R. Adkins, R. J. Kottenstette, D. Wheeler, S. Sokolowski, D. Trudell, J. Byrnes, M. Okandan, J. M. Bauer and R. G. Manley, Recent advancements in the gas-phase MicroChemLab, Philadelphia, PA. U.S.A., 2004.
19. J. G. Smits, *Sensor. Actuat. A-Phys.*, 1990, **21**, 203-206.
20. A. A. Astle, H. S. Kim, L. P. Bernal, K. Najafi and P. D. Washabaugh, *Sensor. Actuat. A-Phys.*, 2007, **134**, 245-256.
21. T. Wei-Cheng, H. K. L. Chan, L. Chia-Jung, S. W. Pang and E. T. Zellers, *J. Microelectromech. Sys.*, 2005, **14**, 498-507.
22. C. Pijolat, M. Camara, J. Courbat, J. P. Viricelle, D. Briand and N. F. de Rooij, *Sensor. Actuat. B-Chem.*, 2007, **127**, 179-185.
23. E. H. M. Camara, P. Breuil, D. Briand, L. Guillot, C. Pijolat and N. F. de Rooij, *Sensor. Actuat. B-Chem.*, 2010, **148**, 610-619.
24. J. H. Seo, S. K. Kim, E. T. Zellers and K. Kurabayashi, *Lab Chip*, 2012, **12**, 717-724.
25. B. Alfeeli, D. Cho, M. Ashraf-Khorassani, L. T. Taylor and M. Agah, *Sensor. Actuat. B-Chem.*, 2008, **133**, 24-32.
26. B. Alfeeli, L. T. Taylor and M. Agah, *Microchem. J.*, 2010, **95**, 259-267.
27. G. Lambertus, A. Elstro, K. Sensenig, J. Potkay, M. Agah, S. Scheuering, K. Wise, F. Dorman and R. Sacks, *Anal. Chem.*, 2004, **76**, 2629-2637.

28. M. Agah, J. A. Potkay, G. Lambertus, R. Sacks and K. D. Wise, *J. Microelectromech. Sys.*, 2005, **14**, 1039-1050.
29. M. Stadermann, A. D. McBrady, B. Dick, V. R. Reid, A. Noy, R. E. Synovec and O. Bakajin, *Anal. Chem.*, 2006, **78**, 5639-5644.
30. S. Reidy, D. George, M. Agah and R. Sacks, *Anal. Chem.*, 2007, **79**, 2911-2917.
31. G. R. Lambertus, C. S. Fix, S. M. Reidy, R. A. Miller, D. Wheeler, E. Nazarov and R. Sacks, *Anal. Chem.*, 2005, **77**, 7563-7571.
32. C. M. Matzke, R. J. Kottenstette, S. A. Casalnuovo, G. C. Frye-Mason, M. L. Hudson, D. Y. Sasaki, R. P. Manginell and C. C. Wong, Microfabricated silicon gas chromatographic microchannels: fabrication and performance, 1998.
33. J. A. Potkay, J. A. Driscoll, M. Agah, R. D. Sacks and K. D. Wise, A high-performance microfabricated gas chromatography column, Kyoto, 2003.
34. A. Bhushan, D. Yemane, D. Trudell, E. Overton and J. Goettert, *Microsyst. Technol.*, 2007, **13**, 361-368.
35. A. D. Radadia, R. I. Masel, M. A. Shannon, J. P. Jerrell and K. R. Cadwallader, *Anal. Chem.*, 2008, **80**, 4087-4094.
36. M. A. Zareian-Jahromi and M. Agah, *J. Microelectromech. Sys.*, 2010, **19**, 294-304.
37. G. Lambertus and R. Sacks, *Anal. Chem.*, 2005, **77**, 2078-2084.
38. M. A. Zareian-Jahromi, M. Ashraf-Khorassani, L. T. Taylor and M. Agah, *J. Microelectromech. Sys.*, 2009, **18**, 28-37.
39. S.-J. Kim, S. M. Reidy, B. P. Block, K. D. Wise, E. T. Zellers and K. Kurabayashi, *Lab Chip*, 2010, **10**, 1647-1654.
40. G. Serrano, D. Paul, S.-J. Kim, K. Kurabayashi and E. T. Zellers, *Anal. Chem.*, 2012, **84**, 6973-6980.
41. S.-J. Kim, G. Serrano, K. D. Wise, K. Kurabayashi and E. T. Zellers, *Anal. Chem.*, 2011, **83**, 5556-5562.
42. Q.-Y. Cai and E. T. Zellers, *Anal. Chem.*, 2002, **74**, 3533-3539.
43. Q. Zhong, W. H. Steinecker and E. T. Zellers, *Analyst*, 2009, **134**, 283-293.
44. M. Rapp, J. Reibel, A. Voigt, M. Balzer and O. Bülow, *Sensor. Actuat. B-Chem.*, 2000, **65**, 169-172.
45. J. Reibel, U. Stahl, T. Wessa and M. Rapp, *Sensor. Actuat. B-Chem.*, 2000, **65**, 173-175.
46. J. Li, Y. Lu, Q. Ye, M. Cinke, J. Han and M. Meyyappan, *Nano Lett.*, 2003, **3**, 929-933.
47. K. Chen and Y.-E. Wu, *Sensor. Actuat. A-Phys.*, 2000, **79**, 211-218.
48. J. Liu, Y. Sun and X. Fan, *Opt. Express*, 2009, **17**, 2731-2738.
49. Y. Sun, S. I. Shopova, G. Frye-Mason and X. Fan, *Opt. Lett.*, 2008, **33**, 788-790.
50. R. C. Bailey and J. T. Hupp, *J. Am. Chem. Soc.*, 2002, **124**, 6767-6774.
51. Y. Dan, Y. Lu, N. J. Kybert, Z. Luo and A. T. C. Johnson, *Nano Lett.*, 2009, **9**, 1472-1475.
52. G. Serrano, H. Chang and E. T. Zellers, A micro gas chromatograph for high-speed determinations of explosive vapors, Denver, CO, U.S.A., 2009.
53. G. Serrano, T. Sukaew and E. T. Zellers, *J. Chromatogr. A*, 2013, **1279**, 76-85.
54. D. Technlogies, *http://www.defiant-tech.com/frog-4000.php*, 2013.
55. E. S. Technology, *http://www.estcal.com/spec%20sheets/4600spec.pdf*

2013.
56. Agilent, *http://www.chem.agilent.com/en-US/products-services/Instruments-Systems/Gas-Chromatography/490-Micro-GC/Pages/default.aspx*, 2013.
57. M. P. Siegal, D. L. Overmyer, R. J. Kottenstette, D. R. Tallant and W. G. Yelton, *Appl. Phys. Lett.*, 2002, **80**, 3940-3942.
58. D. W. VanOsdell, M. K. Owen, L. B. Jaffe and L. E. Sparks, *J. Air Waste Manage.*, 1996, **46**, 883-890.
59. F. Blanco, X. Vilanova, V. Fierro, A. Celzard, P. Ivanov, E. Llobet, N. Cañellas, J. L. Ramírez and X. Correig, *Sensor. Actuat. B-Chem.*, 2008, **132**, 90-98.
60. H. Lahlou, X. Vilanova, V. Fierro, A. Celzard, E. Llobet and X. Correig, *Sensor. Actuat. B-Chem.*, 2011, **154**, 213-219.
61. W. A. Groves, E. T. Zellers and G. C. Frye, *Anal. Chim. Acta*, 1998, **371**, 131-143.
62. T. Nakamoto, Y. Isaka, T. Ishige and T. Moriizumi, *Sensor. Actuat. B-Chem.*, 2000, **69**, 58-62.
63. J. H. Lee, Y.-A. Song and J. Han, *Lab Chip*, 2008, **8**, 596-601.
64. R. T. Kelly, Y. Li and A. T. Woolley, *Anal. Chem.*, 2006, **78**, 2565-2570.
65. J. Lee and J. Han, *Microfluid. Nanofluid.*, 2010, **9**, 973-979.
66. I. Voiculescu, M. Zaghloul and N. Narasimhan, *TrAC Trend. Anal. Chem.*, 2008, **27**, 327-343.
67. T. Wei-Cheng, S. W. Pang, L. Chia-Jung and E. T. Zellers, *J. Microelectromech. Sys.*, 2003, **12**, 264-272.
68. J. Koziel, M. Jia, A. Khaled, J. Noah and J. Pawliszyn, *Anal. Chim. Acta*, 1999, **400**, 153-162.
69. J. J. Whiting and R. D. Sacks, *J. Sep. Sci.*, 2006, **29**, 218-227.
70. J. M. Sanchez and R. D. Sacks, *Anal. Chem.*, 2003, **75**, 978-985.
71. D. Technologies, *http://www.defiant-tech.com/canarythree.php*, 2013.
72. M.-Y. Wong, W.-R. Cheng, M.-H. Liu, W.-C. Tian and C.-J. Lu, *Talanta*, 2012, **101**, 307-313.
73. T. Sukaew and E. T. Zellers, *Sensor. Actuat. B-Chem.*, 2013, **183**, 163-171.
74. E. S. Kolesar and R. R. Reston, *IEEE Compon. Pack. B*, 1998, **21**, 324-328.
75. A. C. Lewis, J. F. Hamilton, C. N. Rhodes, J. Halliday, K. D. Bartle, P. Homewood, R. J. P. Grenfell, B. Goody, A. M. Harling, P. Brewer, G. Vargha and M. J. T. Milton, *J. Chromatogr. A*, 2010, **1217**, 768-774.
76. A. Bhushan, D. Yemane, E. B. Overton, J. Goettert and M. C. Murphy, *J. Microelectromech. Sys.*, 2007, **16**, 383-393.
77. N. Hong-seok, P. J. Hesketh and G. C. Frye-Mason, *J. Microelectromech. Sys.*, 2002, **11**, 718-725.
78. B. Alfeeli, S. Narayanan, D. Moodie, P. Zellner, M. McMillan, D. Hirtenstein, G. Rice and M. Agah, *IEEE Sens. J.*, 2013, **PP**, 1-1.
79. H. Shakeel and M. Agah, *J. Microelectromech. Sys.*, 2013, **22**, 62-70.
80. J. Wang, H. Wang, C. Duan and Y. Guan, *Talanta*, 2010, **82**, 1022-1026.
81. S. Zimmermann, S. Wischhusen and J. Müller, *Sensor. Actuat. B-Chem.*, 2000, **63**, 159-166.
82. S. Zimmermann, P. Krippner, A. Vogel and J. Müller, *Sensor. Actuat. B-Chem.*, 2002, **83**, 285-289.

83. J. Kim, B. Bae, J. Hammonds, T. Kang and M. A. Shannon, *Sensor. Actuat. B-Chem.*, 2012, **168**, 111-117.
84. S. S. Brody and J. E. Chaney, *J. Chromatogr. Sci.*, 1966, **4**, 42-46.
85. F. Ahmadi, Y. Assadi, S. M. R. M. Hosseini and M. Rezaee, *J. Chromatogr. A*, 2006, **1101**, 307-312.
86. B. D. Quimby and J. J. Sullivan, *Anal. Chem.*, 1990, **62**, 1027-1034.
87. S. M. Lee and P. L. Wylie, *J. Agr. Food Chem.*, 1991, **39**, 2192-2199.
88. P. L. Wylie and B. D. Quimby, *J. High Res. Chromatogr.*, 1989, **12**, 813-818.
89. M. Penza, P. Aversa, G. Cassano, W. Wlodarski and K. Kalantar-Zadeh, *Sens. Actuat. B-Chem*, 2007, **127**, 168-178.
90. E. J. Staples, *http://www.estcal.com/tech_papers/papers/Environmental/Phenol.pdf*.
91. M. Penza and G. Cassano, *Sensor. Actuat. B-Chem.*, 2003, **89**, 269-284.
92. K-T Tang, C.-H. Li and S.-W. Chiu, *Sensors*, 2011, **11**, 4609-4621.
93. D. Matatagui, J. Martí, M. J. Fernández, J. L. Fontecha, J. Gutiérrez, I. Gràcia, C. Cané and M. C. Horrillo, *Sensor. Actuat. B-Chem.*, 2011, **154**, 199-205.
94. M. Fang, K. Vetelino, M. Rothery, J. Hines and G. C. Frye, *Sensor. Actuat. B-Chem.*, 1999, **56**, 155-157.
95. E. M. K. Arshak, G.M. Lyons, J. Harris, S. Clifford,, *Sens. Rev.*, 2004, **24**, 181-198.
96. Z. Ying, Y. Jiang, X. Du, G. Xie, J. Yu and H. Wang, *Sensor. Actuat. B-Chem.*, 2007, **125**, 167-172.
97. M. Li, E. B. Myers, H. X. Tang, S. J. Aldridge, H. C. McCaig, J. J. Whiting, R. J. Simonson, N. S. Lewis and M. L. Roukes, *Nano Lett.*, 2010, **10**, 3899-3903.
98. I. Bargatin, E. B. Myers, J. S. Aldridge, C. Marcoux, P. Brianceau, L. Duraffourg, E. Colinet, S. Hentz, P. Andreucci and M. L. Roukes, *Nano Lett.*, 2012, **12**, 1269-1274.
99. M. C. Lonergan, E. J. Severin, B. J. Doleman, S. A. Beaber, R. H. Grubbs and N. S. Lewis, *Chem. Mater.*, 1996, **8**, 2298-2312.
100. M. A. Ryan, A. V. Shevade, H. Zhou and M. L. Homer, *MRS Bull.*, 2004, **29**, 714-719.
101. F. Zee and J. W. Judy, *Sensor. Actuat. B-Chem.*, 2001, **72**, 120-128.
102. E. Covington, F. I. Bohrer, C. Xu, E. T. Zellers and C. Kurdak, *Lab Chip*, 2010, **10**, 3058-3060.
103. G. E. Collins and L. J. Buckley, *Synthetic Met.*, 1996, **78**, 93-101.
104. J. V. Hatfield, P. Neaves, P. J. Hicks, K. Persaud and P. Travers, *Sensor. Actuat. B-Chem.*, 1994, **18**, 221-228.
105. D. L. Ellis, M. R. Zakin, L. S. Bernstein and M. F. Rubner, *Anal. Chem.*, 1996, **68**, 817-822.
106. J. Wang and M. Musameh, *Anal. Chem.*, 2003, **75**, 2075-2079.
107. D. R. Kauffman and A. Star, *Angew. Chem. Int. Edit.*, 2008, **47**, 6550-6570.
108. T. Someya, J. Small, P. Kim, C. Nuckolls and J. T. Yardley, *Nano Lett.*, 2003, **3**, 877-881.
109. J. D. Fowler, M. J. Allen, V. C. Tung, Y. Yang, R. B. Kaner and B. H. Weiller, *ACS Nano*, 2009, **3**, 301-306.

110. F. I. Bohrer, E. Covington, C. a. Kurdak and E. T. Zellers, *Anal. Chem.*, 2011, **83**, 3687-3695.
111. Y.-H. Zhang, Y.-B. Chen, K.-G. Zhou, C.-H. Liu, J. Zeng, H.-L. Zhang and Y. Peng, *Nanotechnology*, 2009, **20**, 185504.
112. J. N. Driscoll and J. B. Clarici, *Chromatographia*, 1976, **9**, 567-570.
113. B. C. Kaanta, H. Chen and X. Zhang, *J. Micromech. Microeng.*, 2010, **20**, 055016.
114. S. Narayanan and M. Agah, *Hilton Head*, 2012, 221-224.
115. S. Narayanan, B. Alfeeli and M. Agah, *IEEE Sens. J.*, 2012, **12**, 1893-1900.
116. B. C. Kaanta, H. Chen, G. Lambertus, W. H. Steinecker, O. Zhdaneev and X. Zhang, presented in part at the 22nd IEEE Int. Conf. Micro Electro Mech. Syst., Sorrento, Italy, 2009.
117. S. I. Shopova, I. M. White, Y. Sun, H. Zhu, X. Fan, G. Frye-Mason, A. Thompson and S.-j. Ja, *Anal. Chem.*, 2008, **80**, 2232-2238.
118. Y. Sun, J. Liu, D. J. Howard, G. Frye-Mason, A. K. Thompson, S.-j. Ja and X. Fan, *Analyst*, 2010, **135**, 165-171.
119. K. Scholten, F. Xudong and E. T. Zellers, *Appl. Phys. Lett.*, 2011, **99**, 141108-141108-141103.
120. R. A. Potyrailo, H. Ghiradella, A. Vertiatchikh, K. Dovidenko, J. R. Cournoyer and E. Olson, *Nat. Photon.*, 2007, **1**, 123-128.
121. C.-S. Cheng, Y.-Q. Chen and C.-J. Lu, *Talanta*, 2007, **73**, 358-365.
122. Y.-C. Kim, W. Peng, S. Banerji and K. S. Booksh, *Opt. Lett.*, 2005, **30**, 2218-2220.
123. J. Homola, S. S. Yee and G. Gauglitz, *Sensor. Actuat. B-Chem.*, 1999, **54**, 3-15.
124. R. C. Bailey and J. T. Hupp, *Anal. Chem.*, 2003, **75**, 2392-2398.
125. B. Michael, P.C. Kevin, B. Matrika, R.S. Philip and M. Mokhtar, *IEEE Photon. Technol. Lett.*, 2007, **19**, 255-257.
126. B. Sutapun, M. Tabib-Azar and A. Kazemi, *Sensor. Actuat. B-Chem.*, 1999, **60**, 27-34.
127. K. Schroeder, W. Ecke and R. Willsch, *Opt. Laser Eng.*, 2009, **47**, 1018-1022.
128. H.J. Patrick, A.D. Kersey and F. Bucholtz, *J. Lightwave Technol.*, 1998, **16**, 1606-1612.
129. J. Zhang, X. Tang, J. Dong, T. Wei and H. Xiao, *Sensor. Actuat. B-Chem.*, 2009, **135**, 420-425.

Chapter II

On-chip Fabry-Pérot interferometric sensors for micro-gas chromatography detection

2.1 Introduction

Detection of volatile organic compounds (VOCs) is of importance for many applications in homeland security, environmental and industrial monitoring, healthcare, and battlefields.[1,2] Traditional gas chromatography systems show excellent detection specificity and sensitivity; however, they are bulky and have high power consumption. Applications of on-site, rapid, and real time VOC analysis require innovative portable micro-gas chromatography (μGC) systems, which have been under intense study in the past couple of decades.[3-5] In addition to the development of miniaturized on-chip micro-fabricated columns, micro-pumps, and micro-heaters.[6-10] significant effort has been focused on developing micro-vapor detectors that need to be sensitive, fast in response, small in size, and easily integrated with other μGC components.

Optical based sensors are one of the most promising gas sensing technologies. As compared to their electrical based counterparts, such as chemiresistor sensor arrays,[11]

Published: Karthik Reddy, et al. Sensors and Actuators B: Chemical, 159, 60-65(2011). Elsevier.

carbon black sensors,[12] and carbon nanotube sensors,[13] they are immune to electromagnetic interference and do not generate any electric field that could be undesirable in sensitive environments. Through years of research, various configurations of optical gas sensors have been explored, including surface plasmon resonance (SPR) sensors,[14,15] ring resonator sensors,[16-19] fiber Bragg grating sensors,[20-22] long period fiber grating sensors,[23-25] photonic crystal fiber sensors,[26] and Fabry-Pérot (FP) type sensors.[27-32] While sensitive, the SPR, fiber grating, and photonic crystal based sensors are difficult to integrate with micro-columns due to their relatively bulky configurations. The capillary based thin-walled ring resonator is the first optical gas sensor that can be fully integrated with μGC, as the capillary serves as both GC column and on-column gas detector.[17,18] However, mass-production of those ring resonators with high reproducibility and mechanical strength has yet to be worked out.

In contrast, FP-based sensors are robust, and display the potential for mass production and simple integration with current μGC technology. For an FP sensor, the gas sensing polymer forms part of the FP cavity. When exposed to VOCs, the polymer thickness or refractive index (RI) changes, thus resulting in the sensing transduction signal. Recently, Liu, et al., fabricated fiber tip based FP sensors using the dip-coating method.[30,31] While these sensors can be integrated with μGC systems and are capable of rapid on-column detection of separated analytes with excellent sensitivity,[30] they suffer from lack of control and variability in the deposition of gas sensing polymer layers. Fabrication of the FP gas sensor on a flat glass substrate has also been explored, [27,28,32] in which the gas sensitive polymer can easily be spin-coated on the glass with better thickness control. However, their setups are complicated and slow in response making it difficult to integrate and perform real-time on-column gas measurement with μGC systems. In addition, due to the very small RI difference between the polymer (~1.4) and the glass substrate (~1.5), the sensitivity of those sensors may be compromised.

Here we developed an FP gas sensor fabricated on a silicon wafer, as shown in Fig. 2-1, which can be integrated with a μGC system for rapid and sensitive detection of VOCs. This FP sensor design provides a number of distinct advantages compared to previous ones. First, due to the large RI difference between the polymer (n=1.4-1.7) and silicon (n=3.4-4), a larger contrast in the interference signal and hence higher detection sensitivity can be achieved. Second, use of prime grade silicon wafers as the substrate instead of glass significantly minimizes substrate roughness, which leads to a low noise in detection. Third, spin-coating instead of dip-coating, used in our work, increases polymer film uniformity and fabrication controllability. Fourth, our design enables sub-micron polymer film, which greatly increases the detection speed. Finally, the on-chip design allows for excellent integration with current μGC separation columns fabricated on a silicon wafer and makes it ideal for mass production. Multiple sensors coated with various polymers can be fabricated in an array to further enhance the gas sensing performance.

In this chapter, we report the FP sensor fabrication and integration with a GC column. Characterization of the sensor under pulsed gas flow shows that our sensor is capable of detecting sub-nano-gram mass of vapor analytes with a response time faster than one second. The simultaneous response of the FP sensor array to different analytes is also presented.

2.2 Theory

An FP cavity creates an interference pattern due to reflection at the polymer-air and polymer-silicon interfaces (see Fig. 2-1(A)). The reflected light intensity, $I(\lambda)$, is governed by:

$$I(\lambda) = R_1 + R_2 + 2\sqrt{R_1 R_2}\cos(\phi), \tag{2.1}$$

where I is intensity of light and λ is wavelength. R_1 and R_2 are the reflection coefficients at the polymer-air and polymer-silicon interfaces, respectively. For the normal incident light, R_1 and R_2 are approximately 16% and 5%, respectively.

$$\phi = \frac{4\pi n t \cos(\theta)}{\lambda} \tag{2.2}$$

where n and t are the polymer RI and thickness, respectively. θ is the incident angle in polymer. Any change in polymer RI and thickness due to the interaction with the analyte vapor will cause the interference pattern to shift, which in turn causes a change in intensity of the measured signal for a given wavelength which through differentiating Eq. 2.1 can be shown by as,

$$\Delta I = -2\sqrt{R_1 R_2}\sin(\phi)\Delta\phi \tag{2.3}$$

thus generating quantitative and temporal information about the presence of the analyte.

2.3. Material and methods

2.3.1 Materials

All the analytes used in the experiments were purchased from Sigma (St. Louis, MO) and had purity greater than 97%. GC guard column (part no. 22335, inner diameter 250 µm) was purchased from Restek (Bellefonte, PA). Universal quick seal column connectors were purchased from Varian (Palo Alto, CA). Silicon wafers were purchased from University Wafer (South Boston, MA). Polydimethylsiloxane (PDMS) was purchased from Fluka (St. Louis, MO) and SU-8 2000.5 was purchased from MicroChem Corp. (Newton, MA). Glass slides were purchased from VWR (Radnor, PA). UV-curable optical glue was purchased from Dymax (Torrington, CT). All materials were used as received.

2.3.2 Sensor preparation

The on-chip FP sensor was prepared by spin-coating a polymer layer on a silicon wafer. The silicon wafer was first diced into a 2.5 cm × 2.5 cm piece. It was then cleaned by immersion in sulfuric acid-dichromate solution overnight, followed by deionized water rinsing. Finally, it was placed under UV light for an hour to ensure removal of any residues.

During experiments, we used two polymers, PDMS and SU-8 2000.5, for the FP sensors. PDMS has been extensively used in gas chromatography and SU-8 is a common photoresist used in microfabrication. Both of them can form thin and uniform layers when spin coated [33]. The PDMS was diluted with toluene (PDMS:toluene=1:4), whereas SU-8 was used as it was. After spin coating, PDMS and SU-8 were soft baked at 120 ^{o}C and 95 ^{o}C, respectively, to remove solvents. The polymer thicknesses were 1.2 μm and 0.8 μm for PDMS and SU-8, respectively. To embed the FP sensor inside a microfluidic channel, an open-top channel was first formed by gluing glass slides together using UV-curable glue and subsequently bonded to the FP sensor wafer (see Fig. 2-1(B)). The microfluidic channel was 1 mm deep and 250 μm wide.

For the study of FP sensor array, a silicon wafer was diced into 8 mm × 8 mm pieces, which were spin-coated with the desired polymer according to the procedures described previously. To align the FP sensors inside the microfluidic channel, 8 mm × 8 mm through-holes were etched on another silicon wafer, of the same thickness as the FP sensor wafer, using MA-6 and STS Pegasus Deep Reactive Ion Etching tools for photolithography and etching, respectively. Then the FP sensors were inserted into the etched wafer and bonded into place (see Fig. 2-1(B), (C), and (D)). The FP sensors installed in this manner ensured that the sensing surface (*i.e.*, the polymer layers) was nearly flush with the microfluidic channel surface so as not to disturb the gas flow. In the experiment, an array of two FP sensors coated with PDMS and SU-8 were used. They were separated by 3 mm inside the microfluidic channel.

2.3.3 Experimental setup

The experimental setup is illustrated in Fig. 2-2(A) and (B). Injection of analytes was carried out at the GC injector. The injected mass was calibrated with mass spectrometry. A 5 m long guard column was used to deliver the analytes to the FP sensor module. Helium was used as the carrier gas with a flow rate of 8 mL/min.

For optical detection, a 532-nm diode laser was split into two beams. One was reflected from the FP sensor and the other served as the reference. The intensity of both beams was recorded in real time by photo-detectors for post-analysis. The data acquisition rate was 90 kHz. A white light source aligned co-linearly with the laser was used in conjunction with a spectrometer (Ocean Optics HR-2000) to obtain the interference spectrum, an example of which is depicted in Fig. 2-2(C). This allowed us to optimize the incident angle, thus positioning the laser near the quadrature point of the FP sensor interference spectrum for the most sensitive measurement. For the array of sensors two sensing beams were used to interrogate the two sensors separately, which allowed us to tune the sensors independently to maximize the sensitivity and response of each sensor. In all experiments, the GC column and the FP sensor modules were kept at room temperature.

2.4 Results and discussion

Inset I in Fig. 2-3(A) presents a typical temporal response of an FP sensor to the pulsed analyte. The signal rises quickly upon the arrival of the analyte and returns to baseline, indicating that the analyte is completely purged. The peak value of the response of the two FP sensors coated respectively with PDMS and SU-8 to different analytes is plotted in Fig. 2-3. The sensitivity depends on the interaction of the analyte with polymer, which in turn depends on the nature of the polymer as well as the analyte's polarity, molecular weight, functional groups and volatility. PDMS is a non-polar polymer and exhibits significantly different interactions with toluene, a non-polar analyte, and acetone, a polar analyte (see Fig. 2-3(A)). The response to toluene shows a near linear variation with mass below 20 ng, with sensitivity of about 2,900 μV/ng (see Inset II) and then starts to saturate afterwards. Given the system noise of 600 μV, the above sensitivity results in a detection limit of 200 pg in mass. Based on the retention time (5 s) and the peak width (1.2 s) obtained from Inset I, as well as the inner diameter (250 μm) and length (5 m) of the GC column, the above mass detection limit corresponds to a detection limit of approximately 1.7 ppm in concentration at atmospheric pressure, which is about one to three orders of magnitude better than 30-1,500 ppm reported for the FP sensor in Ref. [32] that used the same polymer. In contrast, the sensitivity for acetone is measured to be only 46 μV/ng, much lower than that for toluene. The corresponding detection limit is 13 ng in mass (or 202 ppm in concentration; see Appendix III for details on calculation). While using the same analyte (acetone), the SU-8 sensor shows a similar linear variation with injected mass. The sensitivity of the SU-8 sensors is approximately 4 μV/ng which leads to a detection limit of about 150 ng in mass (or 2,336 ppm in concentration).

Rapid detection is crucial in μGC development. Since the data acquisition rate can be over 100 kHz, the FP sensor response is mainly determined by the analyte diffusion processes in the polymer. Therefore, thin polymer films will absorb analytes faster and be purged of analytes faster than thicker films. Fig. 2-4(A)-(C) show that the response time (*i.e.*, full width half maximum of the peak) of the PDMS FP sensor for toluene and acetone is 0.9 seconds, and 0.5 seconds, respectively, two orders of magnitude shorter than those reported in Ref. [32], which is too slow to be used in a μGC system due to the much thicker polymer layer (8.2 μm).

Note that as the vapor peak width may get broadened after the vapor pulse travels along the 5 meter long GC column, the intrinsic FP sensor response time may be obscured. To further characterize the sensing performance of the FP sensors, we also used a flame ionization detector (FID) in replacement of the FP sensor module to detect the analyte. FID measures the vapor pulse instantaneously and therefore provides the actual width of the vapor pulse traveling inside the GC column (see Fig. 2-4 (D)). For toluene, the FP sensor is nearly 0.43 seconds broader than the vapor pulse inside the GC column. This additional delay is caused by the relatively slow diffusion process of toluene molecules into and out of PDMS because of their relatively strong interaction. In comparison, the response of the FP sensors to acetone (see Fig. 2-4(B) and (C)) is nearly the same as the vapor pulse width, owing to the weak interaction between acetone and the polymer. The difference in response time agrees well with the different detection sensitivities of the PDMS FP sensor for toluene and acetone, as discussed previously. Additionally, by comparing Inset I in Fig. 2-3(A) and Fig. 2-4(A) we observe significant broadening of the response time, which is more pronounced as the injected mass is increased, and can lead to a response time as large as 3-5 seconds with an injected mass of 1-2 μg. This broadening effect is due to the overloading of analyte in the polymer, as evidenced by the saturation behavior of the FP sensor at large injected mass in Fig. 2-3(A).

Implementation of a sensor array that has different response patterns for different vapor analytes can significantly improve the analyte identification capability of a μGC system.[5] The on-chip FP sensor developed here is well suited for such applications. In the proof-of-concept experiment, the two FP sensors coated respectively with PDMS and SU-8 were embedded within a microfluidic channel and separated by 3 mm (see Fig. 2-1(C)). Since the linear speed of the analyte inside the microfluidic channel is very high (usually a few meters per second), these two sensors detect an analyte traveling along the channel virtually simultaneously. Figure 2-5 shows the response of the two FP sensors to various combinations of VOCs. Both FP sensors exhibit response proportional to the analyte mass. The results show that the rapid response of the sensors can be effectively used to detect analytes separated through the columns while also giving us important quantification information. Additionally different polymers have different sensitivities with different analytes which can be used as a method to differentiate analytes. This method can be quite useful when co-elution of analytes occurs.

2.5 Conclusion

We have presented robust, simple, on-chip FP sensors that can potentially be integrated with a μGC system for rapid and sensitive VOC detection. A sub-nano-gram detection limit and sub-second detection time have been achieved, both of which are a few orders of magnitude better than those previously reported. To fully exploit the potential of this on-chip FP sensor, future work will be focused on the following aspects.

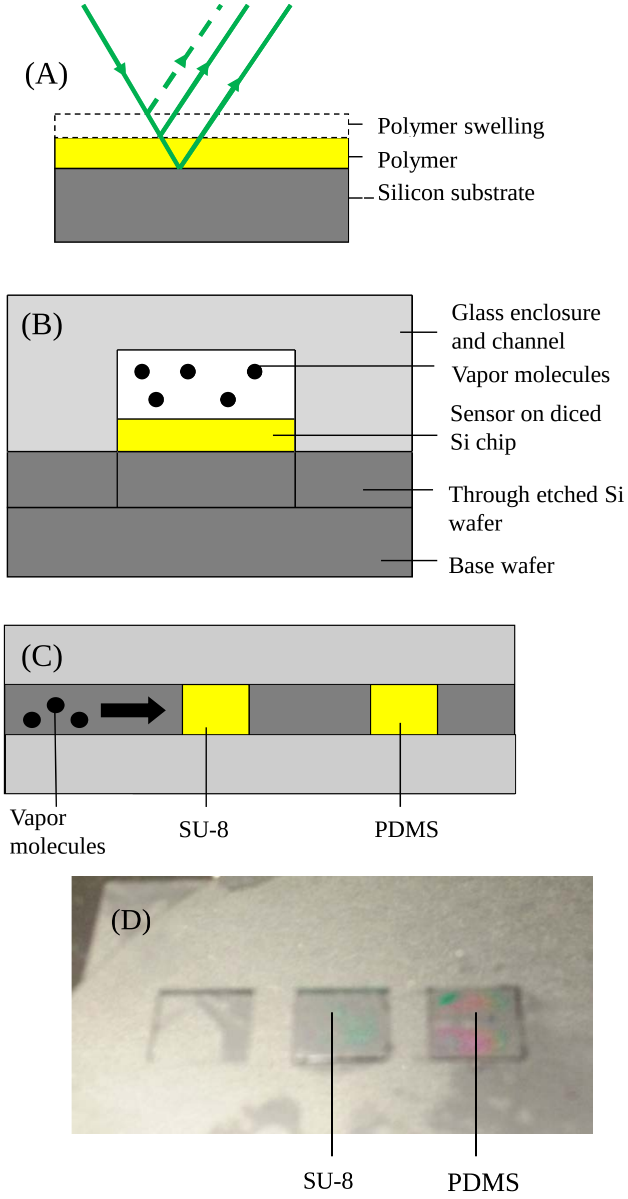

Figure 2-1 (A) Schematic of the Fabry-Pérot (FP) sensor. The polymer spin-coated on a prime grade silicon wafer forms a smooth and controllable vapor sensing layer. The thickness and the RI change in the polymer caused by the absorption of analytes result in a change in the reflected interference signal. (B) Cross-sectional view of the FP sensor configuration inside a microfluidic channel. (C) Top view of the FP sensors coated with different polymer and placed in series. In current experiments, the microfluidic channel was 1 mm deep and 250 μm wide. In the sensor array configuration in (C), two FP sensors were separated by 3 mm. (D) Optical image of device shown in (B) and (C).

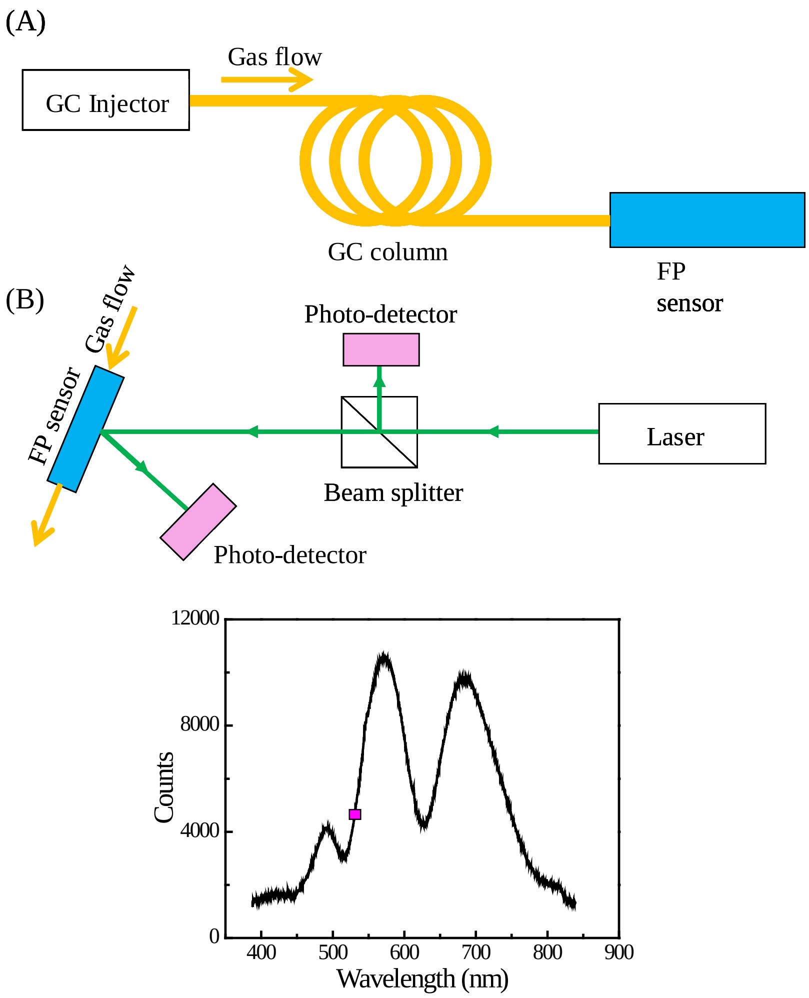

Figure 2-2 (A) Schematic of the flow setup. The FP sensor was encased in a microfluidic channel shown in Fig. 2-1(B), and then connected to a GC injection port through a 5 m long GC guard column. (B) Schematic of the optical detection setup. A 532-nm laser was split into two beams, one for sensing, which measured the reflected intensity change induced by the VOCs inside the channel, and the other one for reference. The incident angle was adjusted to maximize the sensitivity. (C) Example of the interference spectrum from the light reflected from an FP sensor coated with 1.2 μm PDMS film. The incident angle was 10^o. The square on the reflection curve indicates the spectral position of the 532-nm laser used in the experiment.

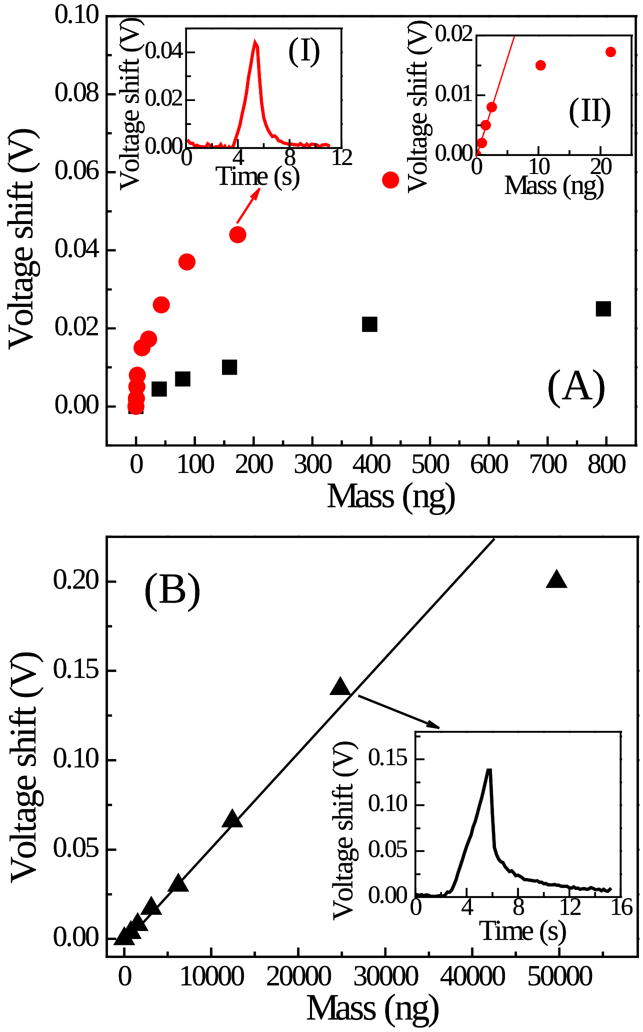

Figure 2-3 (A) Response of PDMS FP sensor to toluene (circles) and acetone (squares) with various injected masses. Inset I: Temporal response of the PDMS FP sensor to the injection of 175 ng of toluene. Inset II: Magnified part shows PDMS sensor response to toluene with injected mass from 1 to 25 ng. The sensitivity of 2,900 μV/ng is obtained through a linear fit shown by the solid line. (B) Response of SU-8 FP sensor to acetone at various injected masses. The sensitivity of 4 μV/ng is obtained through a linear fit shown by the solid line. Inset shows the temporal response of the SU-8 FP sensor to the injection of 23 μg of acetone.

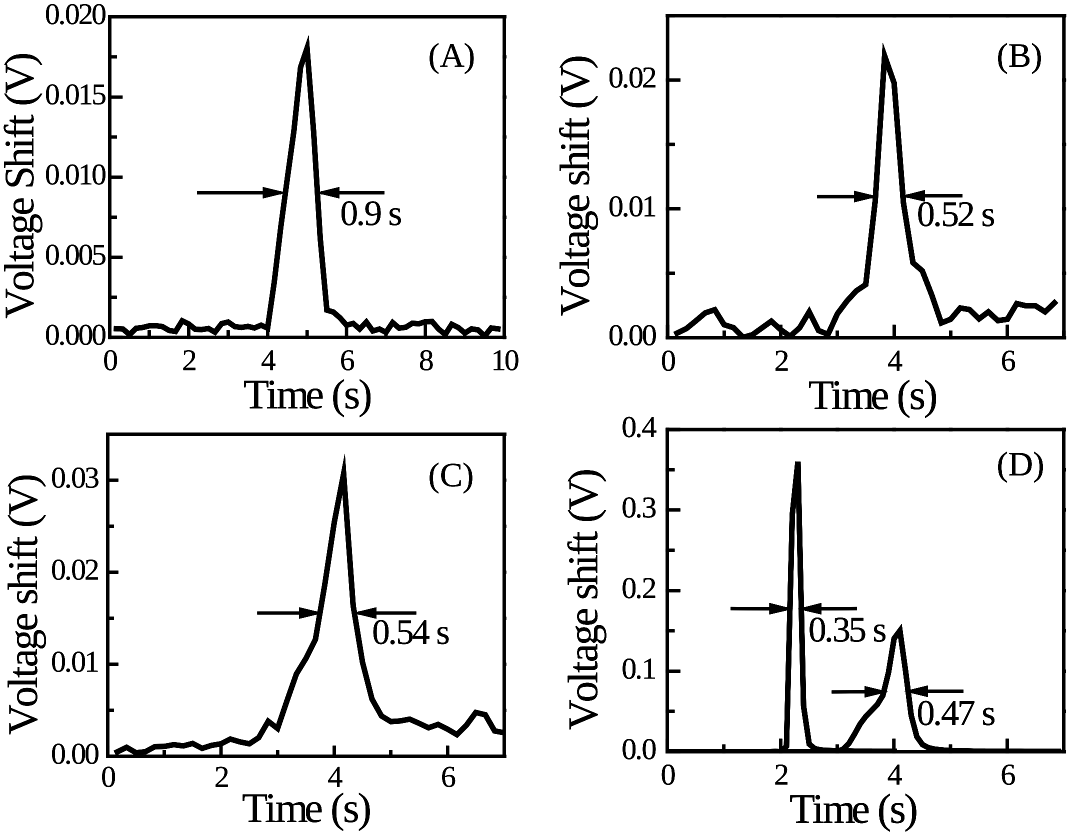

Figure 2-4 Temporal response of PDMS FP sensor to (A) 20 ng of toluene and (B) 390 ng of acetone. (C) Temporal response of SU-8 sensor to 6 μg of acetone. (D) FID response to acetone and toluene. Peaks are horizontally shifted for clarity.

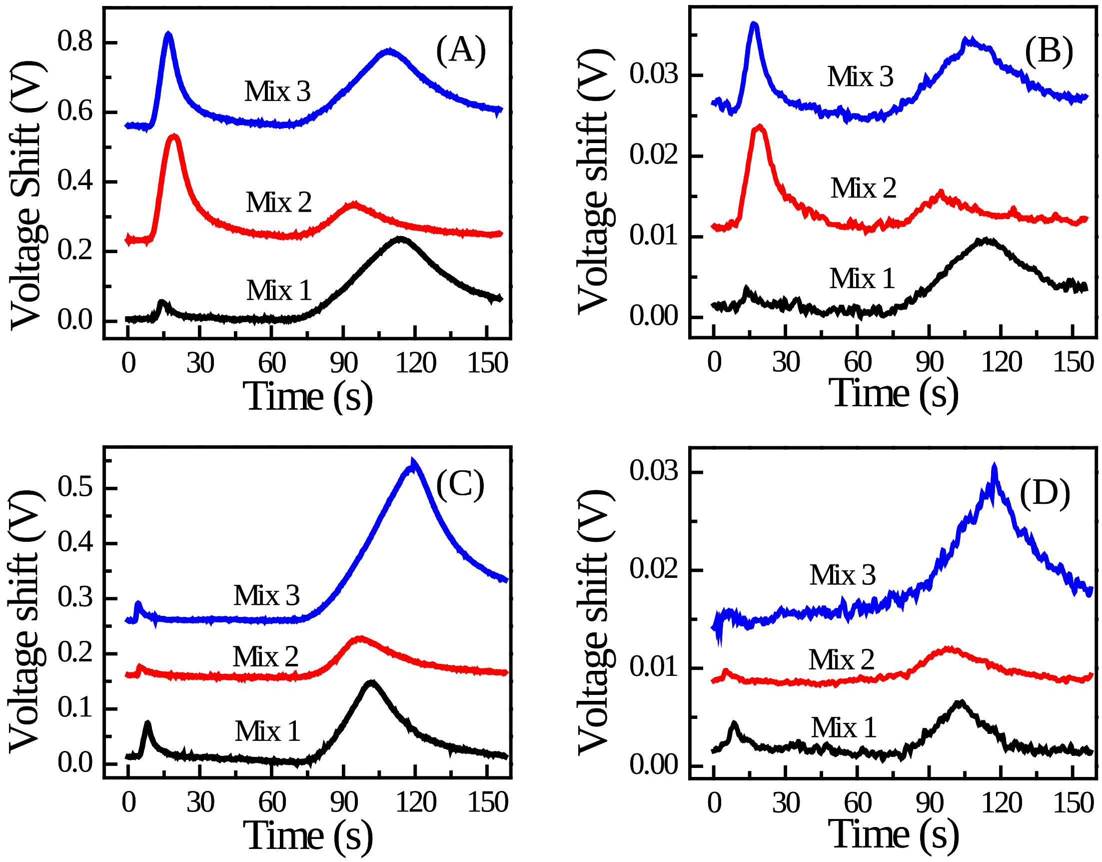

Figure 2-5. (A) and (B) Real time response of the FP sensor array ((A): PDMS and (B): SU-8) to 3 different mixtures of octane and decane. Mix 1: 1.5/3.2 µg, Mix 2: 3.0/1.6 µg, and Mix 3: 3.0/3.2 µg for octane/decane, respectively. (C) and (D) Real time response of the FP sensor array. ((C): PDMS and (D): SU-8) to 3 different mixtures of acetone and decane. Mix 1: 1.6/2.4 µg, Mix 2: 0.8/1.6 µg, and Mix 3: 0.4/3.2 µg for acetone/decane, respectively.

References

1. E.J. Staples and S. Viswanathan, *IEEE Sens. J.*, 2005, **5**, 622-631.
2. F. L. Dorman, J. J. Whiting, J. W. Cochran and J. Gardea-Torresdey, *Anal. Chem.*, 2010, **82**, 4775-4785.
3. E.S. Kolesar Jr. and R.R. Reston, *IEEE Trans. Comp., Pack., and Manu. Tech., Part B: Adv. Pack.,*, 1998, **21**, 324-328.
4. E.B. Overton, K.R. Carney, N. Roques and H.P. Dharmasena, *Field Anal. Chem. & Tech.*, 2001, **5**, 97-105.
5. C-J Lu, J. Whiting, R.D. Sacks and E.T. Zellers, *Anal. Chem.*, 2003, **75**, 1400-1409.
6. S.C. Terry, J.H. Jerman and J.B. Angell, *IEEE Trans. Elec. Dev.*, 1979, **26**, 1880-1886.
7. N. Hong-seok, P. J. Hesketh and G. C. Frye-Mason, *J. Microelectromechanical Sys.*, 2002, **11**, 718-725.
8. M. Agah, J.A. Potkay, G. Lambertus, R. Sacks and K.D. Wise, *J. Microelectromech. Sys.*, 2005, **14**, 1039-1050.
9. G.R. Lambertus, C.S. Fix, S.M. Reidy, R.A. Miller, D. Wheeler, E. Nazarov and R. Sacks, *Anal. Chem.*, 2005, **77**, 7563-7571.
10. S. Reidy, D. George, M. Agah and R. Sacks, *Anal. Chem.*, 2007, **79**, 2911-2917.
11. Q-Y Cai and E. T. Zellers, *Anal. Chem.*, 2002, **74**, 3533-3539.
12. F. Zee and J. Judy, MEMS chemical gas sensor, 1999.
13. M. Stadermann, A. D. McBrady, B. Dick, V. R. Reid, A. Noy, R. E. Synovec and O. Bakajin, *Anal. Chem.*, 2006, **78**, 5639-5644.
14. B. Liedberg, C. Nylander and I. Lunström, *Senor. Actuat.*, 1983, **4**, 299-304.
15. C. de Julián Fernández, M. G. Manera, G. Pellegrini, M. Bersani, G. Mattei, R. Rella, L. Vasanelli and P. Mazzoldi, *Sensor. Actuat. B-Chem.*, 2008, **130**, 531-537.
16. A. Ksendzov, M. L. Homer and A. M. Manfreda, *Elec. Lett.*, 2004, **40**, 63-65.
17. S.I. Shopova, I.M. White, Y. Sun, H. Zhu, X. Fan, G. Frye-Mason, A. Thompson and S-J Ja, *Anal. Chem.*, 2008, **80**, 2232-2238.
18. Y. Sun, J. Liu, D.J. Howard, G. Frye-Mason, A.K. Thompson, S-J Ja and X. Fan, *Analyst*, 2010, **135**, 165-171.
19. N. A. Yebo, P. Lommens, Z. Hens and R. Baets, *Opt. Express* 2010, **18**, 11859-11866.
20. B. Sutapun, M. Tabib-Azar and A. Kazemi, *Sensor. Actuat. B-Chem.*, 1999, **60**, 27-34.
21. B. Michael, P.C. Kevin, B. Matrika, R.S. Philip and M. Mokhtar, *IEEE Phot. Tech. Lett.*, 2007, **19**, 255-257.
22. K. Schroeder, W. Ecke and R. Willsch, *Optics and Lasers in Engineering,* 2009, **47**, 1018-1022.
23. H.J. Patrick, A.D. Kersey and F. Bucholtz, *J. Lightwave Tech.*, 1998, **16**, 1606-1612.
24. A. Cusano, P. Pilla, L. Contessa, A. Iadicicco, S. Campopiano, A. Cutolo, M. Giordano and G. Guerra, *Appl. Phys. Lett.*, 2005, **87**, 234105.

25. J. Zhang, X. Tang, J. Dong, T. Wei and H. Xiao, *Sensor. Actuat. B-Chem.*, 2009, **135**, 420-425.
26. J. Villatoro, M. P. Kreuzer, R. Jha, V. P. Minkovich, V. Finazzi, G. Badenes and V. Pruneri, *Opt. Express*, 2009, **17**, 1447-1453.
27. G. Gauglitz, A. Brecht, G. Kraus and W. Nahm, *Sensor Actuat. B-Chem.*, 1993, **11**, 21-27.
28. D. Reichl, R. Krage, C. Krumme and G. Gauglitz, *Appl. Spectrosc.*, 2000, **54**, 583-586.
29. J. Zhang, M. Luo, H. Xiao and J. Dong, *Chem. of Mat.*, 2005, **18**, 4-6.
30. J. Liu, Y. Sun and X. Fan, *Opt. Express*, 2009, **17**, 2731-2738.
31. J. Liu, Y. Sun, D.J. Howard, G. Frye-Mason, A.K. Thompson, S-J Ja, S-K Wang, M. Bai, H. Taub, M. Almasri and X. Fan, *Anal. Chem.*, 2010, **82**, 4370-4375.
32. C. Martínez-Hipatl, S. Muñoz-Aguirre, G. Beltrán-Pérez, J. Castillo-Mixcóatl and J. Rivera-De la Rosa, *Sensor. Actuat. B-Chem.*, 2010, **147**, 37-42.
33. A. Thangawng, R. Ruoff, M. Swartz and M. Glucksberg, *Biomed. Microdevices*, 2007, **9**, 587-595.

Chapter III

Rapid, sensitive, and multiplexed on-chip optical sensors for micro-gas chromatography

3.1 Introduction

Micro-gas chromatography (μGC) systems have come under intense study for use in a variety of fields including environmental monitoring, homeland security, and healthcare.[1-2] Tremendous progress has been made in μGC development, there are still a few problems in the current μGC systems that need major improvement. First, long sampling and pre-concentration times are required for detection of low concentrations or masses of VOCs. Second, due to the short columns, μGC suffers from the low chromatographic resolution. Several analytes may co-elute within one separation peak, making the analysis and identification of VOCs much more difficult than with a conventional GC system having excellent separation capability. To overcome these drawbacks, it is urgent to develop μGC sensors that are highly sensitive to reduce the sampling time, able to qualitatively analyze VOCs embedded in a co-eluted peak, and compatible with other μGC components for easy device integration and miniaturization.

Published: Karthik Reddy, et al. Lab on a Chip, 12, 901-905, (2012). Royal Chemical Society.

In recent years there has been an increasing focus on the use of arrays of partially sorptive sensors that may have the potential to achieve the above sensor design goals. Chemi-resistors arrays have been shown to effectively discriminate between individual analytes in a mixture.[3-6] However, they are inherently susceptible to electromagnetic interference and have a detection limit of only a few nanograms.[7] Surface acoustic wave (SAW) sensors coated with polymers have also been demonstrated for vapor discrimination,[8-12] but they suffer from the interference between neighboring sensors.[9-10] Furthermore, while a detection limit of 10 pg was reported with an uncoated SAW sensor,[13] the detection limit for the polymer coated sensor increases to the nanogram range.[14] Therefore, the SAW device is still not ideal for vapor sensor array development.

As compared to the chemi-resistor and SAW sensor, the optical vapor sensor is immune to electromagnetic interference and can operate without crosstalk, thus making it a promising candidate for use in μGC sensor arrays. Recent developments in optical vapor sensor technology have seen the implementation of Bragg[15-17] and long period gratings sensors,[18-20] surface plasmon resonance (SPR) sensors,[21-22] localized surface plasmon resonance (LSPR) sensors,[23-24] ring resonator sensors,[25-28] and photonic crystal fiber (PCF) sensors[29] for the detection of VOCs. However, those vapor sensors are either incompatible with μGC components, difficult to fabricate, or complicated in optical design.

The Fabry-Pérot (FP) cavity based optical vapor sensor avoids the pitfalls of the above mentioned optical sensors due to its simple optical configuration, ease of fabrication and high sensitivity.[30-36] As illustrated in Fig. 3-1(A), an FP sensor is formed by a thin layer of vapor sensitive polymer coated on a substrate. The light reflected by the air/polymer and polymer/substrate interface results in an interference spectrum (see Fig. 3-1(B)). The interaction of the VOC and polymer causes a change in the polymer thickness and/or refractive index, which in turn leads to a spectral shift in the characteristic interference spectrum corresponding to the extent of vapor sorption. Therefore, the FP sensor is able to provide quantitative and kinetic information about the vapor flowing inside a microfluidic channel. Previous work has shown that these sensors are capable of rapid sub-second VOC detection with a detection limit in the range of a few tens to a few hundreds of picograms.[34,36]

Here we developed an FP sensor array on chip with significantly improved sensing capability for μGC applications. As shown in Fig. 3-2, using microfabrication technology, we were able to assemble four FP sensors inside a μGC fluidic channel for on-column detection. A CMOS imager was used to simultaneously monitor the FP sensor array in real-time. The FP sensor array described here offers several distinct advantages compared to those previously demonstrated. First, using a sensor array, both qualitative and quantitative analysis of VOCs mixture is possible to enhance the μGC's capability in analyte identification. Second, the sensor is capable of performing on-column multiple polymer interrogation, with no cross talk between signals, using a single imager. Third, one to two orders of magnitude improvement in the detection limit can be achieved, tremendously reducing the amount of time needed for pre-concentration of vapors. Finally, the sensor is robust, cost effective and highly reproducible. Here we used four different polymers (OV-1, OV-73, OV-215 and OV-1701) to fabricate and characterize the FP sensor array on chip. Then four analytes (acetone, methanol, heptane and toluene) were employed as model systems to test the FP sensor array and establish a method to analyze VOC mixtures.

3.2 Material and methods

3.2.1 Materials

All the analytes and solvents used in the experiments were purchased from Sigma (St. Louis, MO) and had purity greater than 97%. GC guard column (part no. 22335, inner diameter 250 µm), RTX-1 column (part no. 40101, inner diameter 180 µm) and RTX-Wax column (part no. 12423, inner diameter 250 µm) were purchased from Restek (Bellefonte, PA). Universal quick seal column connectors were purchased from Varian (Palo Alto, CA). Silicon wafers were purchased from University Wafer (South Boston, MA). OV-1 (Polydimethylsiloxane or PDMS) was purchased from Fluka (St. Louis, MO). OV-73 (Diphenyldimethylsilicone), OV-215 (Trifluoropropylmethylsilicone) and OV-1701 (Dimethylphenyl cyano substituted) were purchased from Ohio Valley Specialty (Marietta, OH). Glass slides were purchased from VWR (Radnor, PA). UV-curable optical glue was purchased from Dymax (Torrington, CT). All materials were used as received.

3.2.2 Sensor preparation

For studies of individual FP sensors, each sensor was prepared using the spin-coating method. First, a silicon wafer was diced to an 8 mm x 10 mm piece using an ADT 7100 dicing saw, which was subsequently immersed overnight in sulfuric acid-dichromate solution to oxidize any contaminants, followed by a rinse with deionized water. Finally, it was placed under UV light for an hour to ensure removal of any residues.

Then OV-1, OV-73, OV215 or OV-1701 was used as the vapor sensing layer. These polymers are commonly used in many GC applications like column stationary phase. The polymer solution was prepared by dissolving the polymer gum in their corresponding solvent. OV-1 was diluted with toluene (PDMS:toluene=1:5), OV-73 and OV-1701 were diluted with pentane (OV-73:pentane=1:6 and OV-1701:pentane=1:5), and OV-215 was diluted with ethyl acetate (OV-215:ethyl acetate=1:5). The polymer was then coated using a spin coater, with spin speed calibrated such that the polymer thickness for all four sensors was in the range of 1-1.2 μm. The polymer was first spun at 1,500-2,000 rpm for 10 seconds and then at 6,600-7,600 rpm for 30 seconds. The initial spin spreads the polymer across the entire silicon chip and the second step removes excess polymer and solvent. The spin-coated chip was then heated for 30 seconds at 80^{o}C to completely remove the solvent. Finally, an open-bottom microfluidic channel assembled from glass slides and UV-curable optical glue was sealed on top of the coated chip. The resultant channel was approximately 1 mm deep and 450 μm wide.

For sensor array preparation, we used the drop-coating method. The overall sensor array layout is illustrated in Fig. 3-2(A) and (B). First, four wells of 1.3 μm deep were etched into a prime grade silicon wafer (8 mm x 6 mm) using an MA-6 and STS Pegasus-4 tools for lithography and etching respectively (Fig. 3-2 (C) and (D)). Each well was 200 μm x 200 μm and was separated by 800 μm so that the entire length can be imaged with a CMOS imager. The previously created polymer solutions were diluted, with the corresponding solvent, to one-tenth of their initial concentrations, and then drop coated into each well using a pulled capillary micro-dropper made in-house. The well acted as a containment barrier for the polymer, ensuring no cross contamination between sensors, and that the sensing surface is nearly flush with the silicon, thereby minimizing disturbance to the gas flow. Finally, an open-bottom microfluidic channel assembled from glass slides and UV-curable optical glue was sealed on top of the coated chip. The resultant channel was approximately 1 mm deep and 450 μm wide.

3.2.3 Experimental setup

The experimental setup is illustrated in Fig. 3-3. To test each individual sensor, individual vapor analyte was injected at the GC injection port and delivered to the sensor module using a 4 m long GC guard column. A Toptica 785 nm laser was used to generate the optical detection beam. The light was aligned using an FC/APC terminated optical fiber and a beam collimator. The reflected beam was collected by a Thorlabs CMOS imager (product no. DCC1545M), with an acquisition rate of 16 frames per second. To acquire information regarding the interference spectrum of the FP sensors and to tune the beam incident angle to increase sensitivity of the sensors, a white light source was placed co-linearly with the laser beam and a spectrometer (Ocean Optics HR-2000) was used at the reflection side to monitor the interference spectrum (see the dashed lines in Fig. 3-3(B)).[36]

To test the sensor array and to examine its collective response to VOCs, a mixture containing different mass combinations of the four vapor analytes was injected at the GC injection port. It was then delivered to a 25 cm long microfabricated GC column (400 μm x 100 μm) coated with OV-1, 2.5 m long Carbowax column, and a 1 m long column OV-

1 column to separate a mixture of acetone, methanol, heptane and toluene before entering the sensor module (the fabrication and the subsequent coating of the microfabricated GC column can be found in Refs. [37-38]). The overall optical detection setup remained the same as previously described, except that a lens (VZM450 from Edmund Optics) was added between the sensor array and the imager, whose field of view is sufficiently large to capture all four sensors so that the response of all sensors to the vapor analyte flowing inside the channel could be obtained instantaneously and simultaneously. The data for each sensor is saved separately and can be processed to form chromatograms for each individual sensor. The reference signal was acquired from the light reflected from bare silicon and used to remove any long term amplitude drifts or false peaks caused by laser instability.

All experiments were carried out at room temperature with no heating of the columns or sensors. Mass of injected analytes was calibrated using the splitter and mass spectroscopy system. Helium was used as the carrier gas with a flow rate of 8 mL/min.

3.3 Results and discussion

3.3.1 Sensor characterization

Each individual FP sensor was tested with four different analytes, acetone, methanol, heptane and toluene injected individually. The insets in Fig. 3-4 show examples of the chromatogram for each analyte. The signal rises rapidly with the increasing presence of analyte and rapidly falls back to the baseline as it is purged from the polymer. Since the CMOS imager was operated at 16 frames per second, a system time resolution of 60 ms can be achieved. During the experiment analyte vapor was sampled using a gas syringe, allowing for control over the volume, and hence mass, of injected analytes. The peak response of each sensor to each injected mass is shown in Fig. 3-4 and Fig. 3-5. At low analyte concentrations, the sensor peak response is linear to the injected mass. When the injected mass increases, the saturation effect occurs and the response curve levels off.

The sensitivity of each sensor depends on the interaction between the analyte and the polymer, which in turn depends on a variety of factors, including polarity of analyte and polymer, volatility of analyte, functional groups, molecular weight, *etc*. For example, as shown in Fig. 3-4(A), there is a clear difference in the responses for each polymer to the same analyte (acetone), with OV-215 showing the strongest interaction and OV-1 showing the weakest interaction. The same phenomenon occurs for the other three analytes. To estimate the detection limit, we use the lowest data point (usually in the picogram range) in combination with the sensor noise level of approximately 0.1 counts. Note that different sensors may have slightly different noise level because of surface roughness of the polymer and scattering of the optical beam. However, these differences are very small and are not a major factor in the different detection limits of each sensor. The detection limit for each analyte is listed in Table 3-1. Generally, our FP sensor shows a detection limit a few orders of magnitude better than previously reported.[35-36] In particular, with OV-73 a sub-picogram detection limit of 0.64 pg and 0.79 pg was achieved for heptane and toluene, respectively. Based on the retention time (4 s) and the peak width (0.125 s) for heptane obtained from the inset in Fig. 3-4(C), as well as the inner diameter (250 μm) and length (4 m) of the GC column, the above detection limit corresponds to about 25 ppb in concentration at atmospheric pressure. Similarly, a concentration detection limit of 28 ppb for toluene can also be derived. Both are a few times better than the best results reported for chemi-resistors,[6] and SAW sensors,[11] and at least one order of magnitude better than previously reported FP sensors.[34-36]

3.3.2 Demonstration of functional sensor array and pattern analysis

From Fig. 3-4 it is clear that the sensitivities of different polymers to analytes vary greatly, which allows the use of response patterns of those polymers to better resolve vapor analytes. The sensor array was constructed by drop-coating the etched wells on a silicon chip, which confines the polymers and prevents cross contamination. The wells were closely arranged so that they can be imaged with a CMOS imager. Fig. 3-6 shows the chromatograms obtained by each sensor for two different mass combinations of the four analytes. Due to the high linear speed of the analyte traveling inside the microfluidic channel, all FP sensors in the array were able to detect the same analyte virtually simultaneously.

The peak heights are used to the extract the response patterns for each analyte. The response pattern shown in Fig. 3-7 corresponds to the injected mixture for Fig. 3-6(A). The response patterns clearly differ for each injected analyte, and match the initial testing results shown in Fig. 3-4. The error bars show a variation of less than 15 percent between runs, which will not impede the use of response patterns as a method of analysis. The response pattern for chromatogram in Fig. 3-5(B) that used a different mass combination is shown in Fig. 3-8. Although the absolute peak height is different between Fig. 3-6(A) and (B), the corresponding response patterns agree very well with each.

3.4 Conclusion

We fabricated and characterized highly sensitive FP sensor array with orders of magnitude improvement in VOC detection limit. The array is robust, reproducible, fast in response and compatible with μGC components. In particular, it has the ability to simultaneously gather information from multiple sensors to conduct pattern analysis for qualitative and quantitative analysis of VOC mixtures.

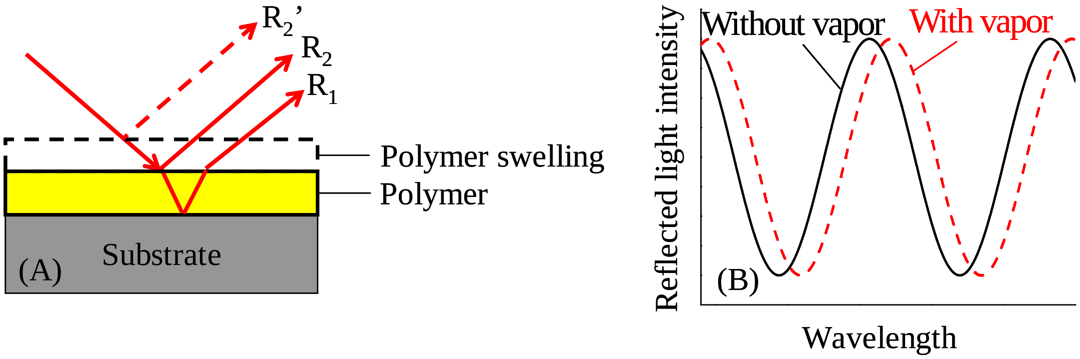

Figure 3-1 (A) Schematic of the Fabry-Pérot (FP) sensor. The absorption of analytes results in a change in the thickness and RI of the polymer film, which in turn leads to a change in the interference pattern. R_1 is the light reflected from the polymer-substrate interface. R_2 and R_2' are the light reflected from the air-polymer interface before and after the polymer change, respectively. (B) Example of the interference pattern generated by an FP and the effect of analyte absorption. At a fixed wavelength the resonance spectral shift can be recorded as an increase or decrease in the reflected intensity.

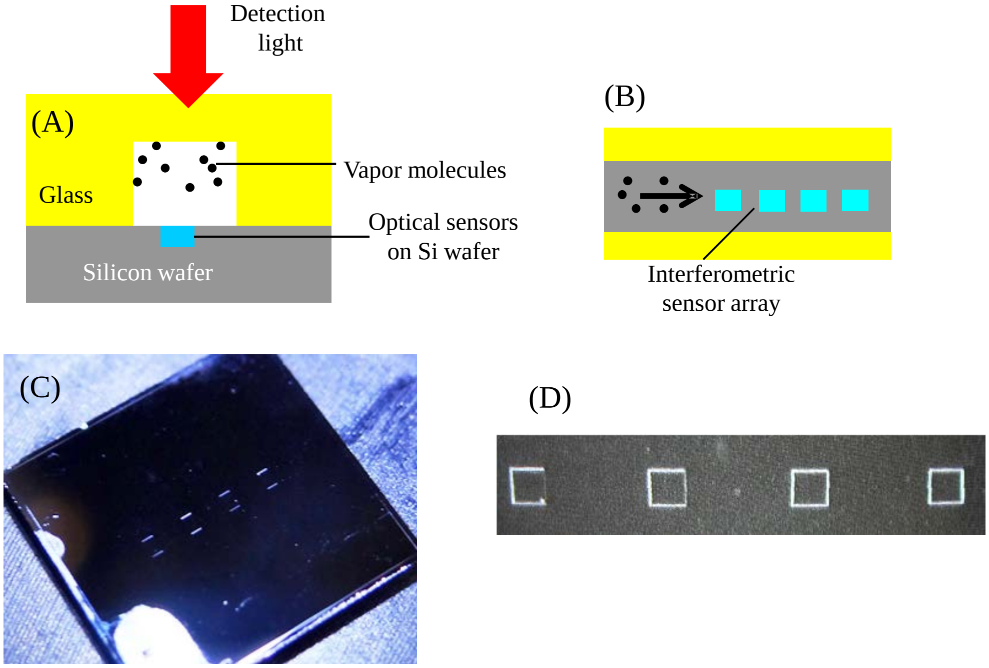

Figure 3-2 (A) Cross-sectional view of the FP sensor array fabricated on etched silicon wafer inside a microfluidic channel of 1 mm deep and 450 µm wide. (B) Top-view of the FP sensor array. Four different polymer solutions were dropped into the etched wells using a micro-dropper. Dimensions are not to scale. (C) Image of an etched silicon chip containing the sensor array. The overall device was 8 mm x 6 mm and has an inlet and an outlet, to which a capillary column could be inserted for fluidic connection. (D) Image of 4 wells on chip. Each well was 200 µm x 200 µm and 1.3 µm deep. The wells were separated by 800 µm.

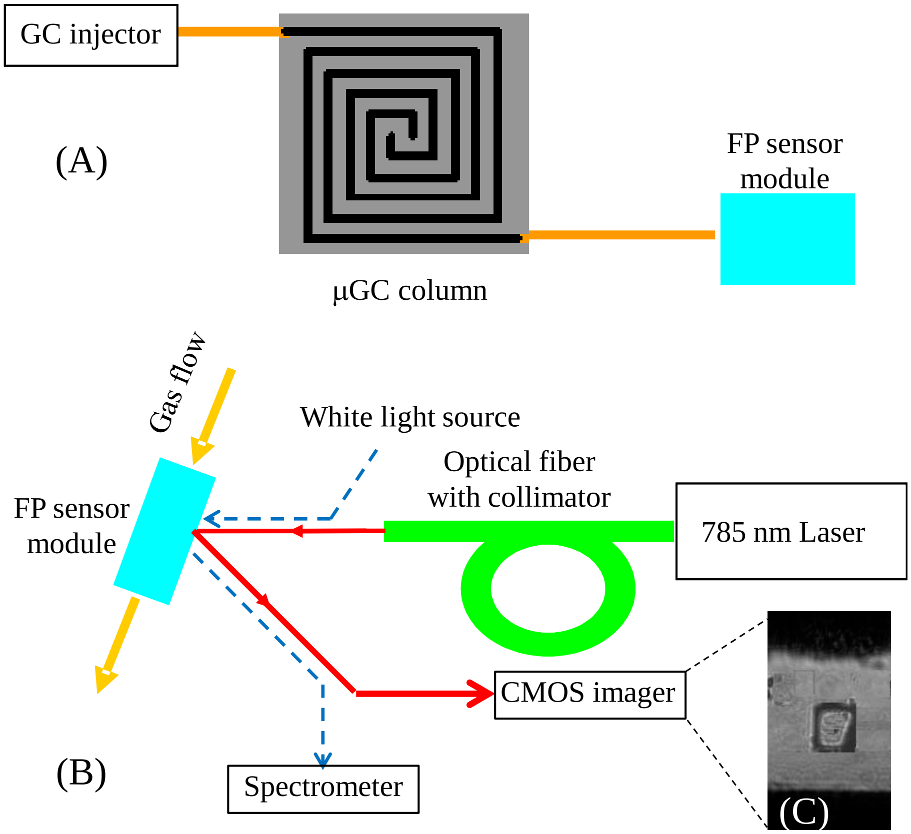

Figure 3-3 (A) Schematic of the µGC setup. The FP sensor module shown in Fig. 3-1(A) was connected to a GC injection port via a standard capillary GC column or microfabricated GC column. (B) Schematic of the optical detection setup. A 785-nm laser was used to interrogate the change in reflected intensity caused by the presence of vapor analyte inside the channel. The incident angle could be adjusted to maximize the sensitivity. The CMOS imager provides quantitative and kinetic information about polymers' response to the vapor analytes. Dashed lines show the path of the white light, which was used to optimize the 785 nm laser alignment. (C) Image of an FP sensor with polymer in an etched well.

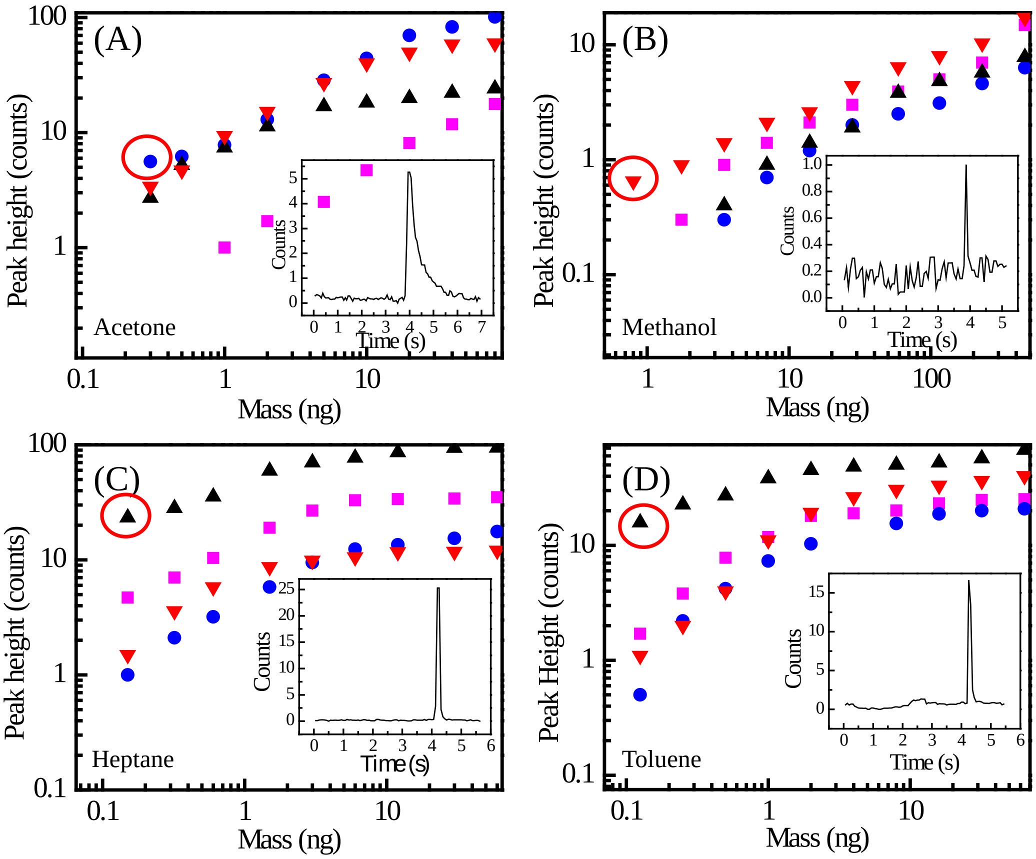

Figure 3-4 Response of four different polymers OV-1 (squares), OV-73 (triangles), OV-215 (circles) and OV-1701 (inverted triangles) to various injected masses of (A) acetone, (B) methanol, (C) heptane and (D) toluene. Insets show the chromatogram corresponding to the circled data point in each figure. Analytes were delivered to the sensor using a 4 m long guard column.

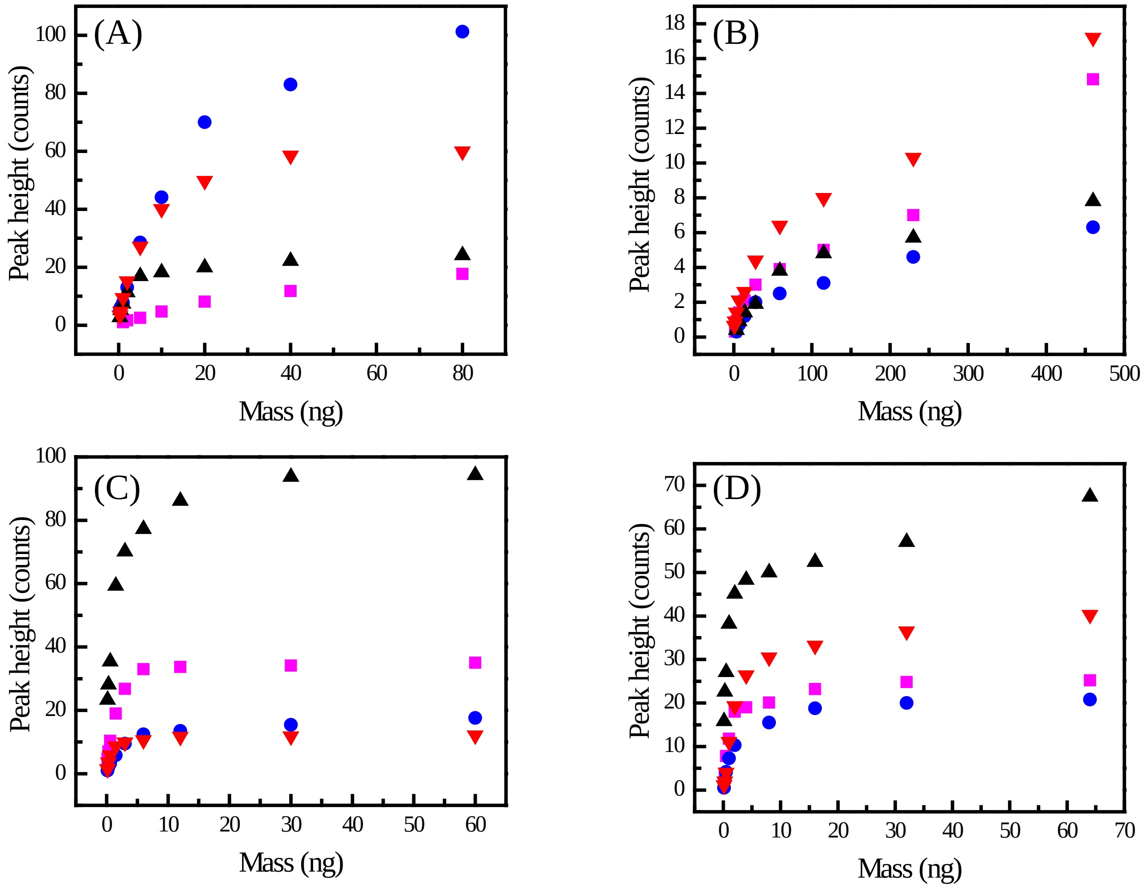

Figure 3-5 Response of four different polymers OV-1 (squares), OV-73 (triangles), OV-215 (circles) and OV-1701 (inverted triangles) to various injected masses of (A) acetone, (B) methanol, (C) heptane and (D) toluene.

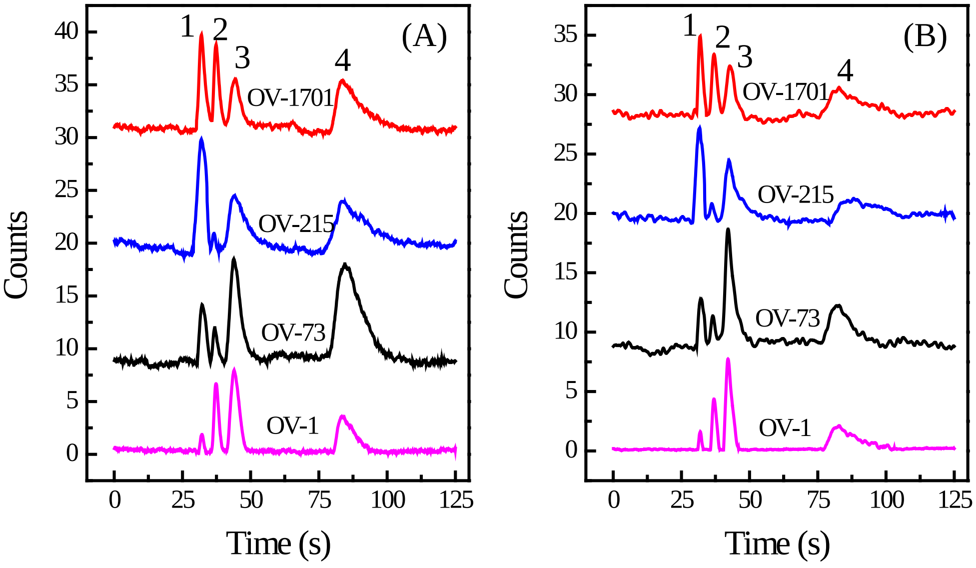

Figure 3-6 Chromatographic response of four FP sensors to a mixture of acetone (#1), methanol (#2), heptane (#3), and toluene (#4). Injected mass ratio for acetone, methanol, heptane, and toluene was (A) 1.4:14:1:2.6 and (B) 0.7:8.6:1:0.7, respectively. Chromatograms are vertically shifted for clarity. Analytes were delivered to the sensors using a series of OV-1 and carbowax columns.

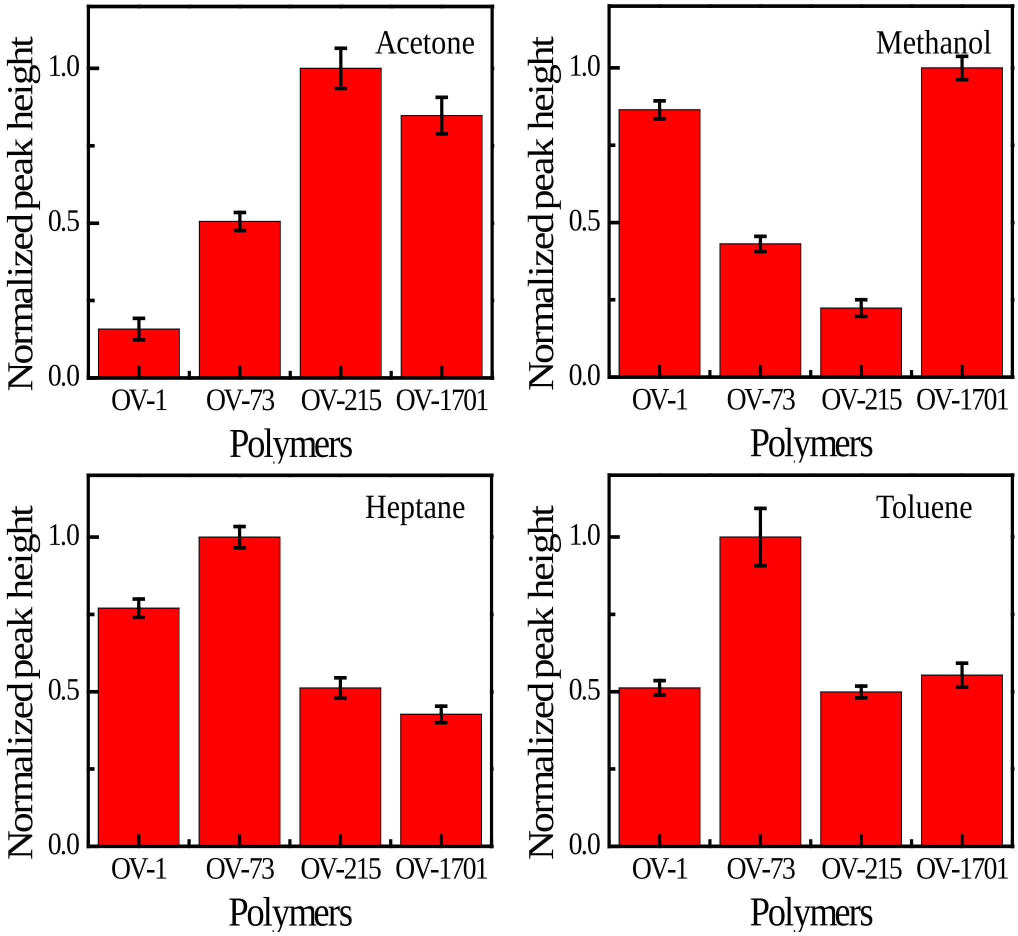

Figure 3-7 Normalized response patterns of each analyte with respect to the four polymers on chip derived from chromatograms shown in Fig. 3-6(A). Error bars show the standard deviation measured over 5 runs. Clear differences can be seen between the response patterns of each analyte, forming a basis of analyte identification.

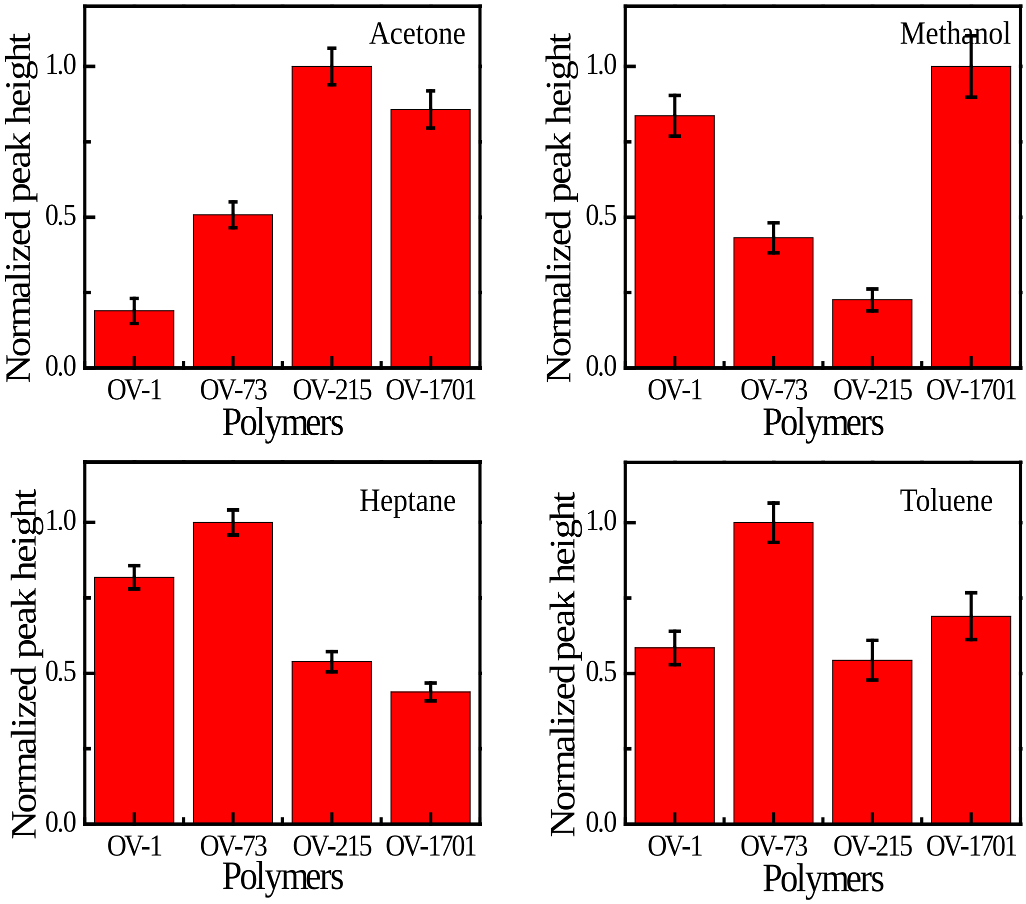

Figure 3-8. Normalized response patterns of each analyte with respect to the four polymers on chip derived from chromatograms shown in Fig. 3-6(B). Error bars show the standard deviation measured over 5 runs.

Detection limits (pg)				
	Acetone	**Methanol**	**Heptane**	**Toluene**
OV-1	100	583	3.2	7.4
OV-73	11	875	0.64	0.79
OV-215	5.4	1,166	15	25
OV1701	8.8	123	10	11

Table 3-1 Detection limits of four analytes with each polymer.

References

1. E.J. Staples and S. Viswanathan, *IEEE Sens. J.*, 2005, **5**, 622-631.
2. F. L. Dorman, J. J. Whiting, J. W. Cochran and J. Gardea-Torresdey, *Anal. Chem.*, 2010, **82**, 4775-4785.
3. M. C. Lonergan, E. J. Severin, B. J. Doleman, S. A. Beaber, R. H. Grubbs and N. S. Lewis, *Chem. Mater.*, 1996, **8**, 2298-2312.
4. E. Covington, F. I. Bohrer, C. Xu, E. T. Zellers and C. Kurdak, *Lab Chip*, 2010, **10**, 3058-3060.
5. C. K. Ho and R. C. Hughes, *Sensors*, 2002, **2**, 23-34.
6. Q.-Y. Cai and E. T. Zellers, *Anal. Chem.*, 2002, **74**, 3533-3539.
7. T. Sukaew, H. Chang, G. Serrano and E. T. Zellers, *Analyst*, 2011, **136**, 1664-1674.
8. M. Penza and G. Cassano, *Sensor. Actuat. B-Chem.*, 2003, **89**, 269-284.
9. M. Rapp, J. Reibel, A. Voigt, M. Balzer and O. Bülow, *Sensor. Actuat. B-Chem.*, 2000, **65**, 169-172.
10. K-T Tang, C.-H. Li and S.-W. Chiu, *Sensors*, 2011, **11**, 4609-4621.
11. D. Matatagui, J. Martí, M. J. Fernández, J. L. Fontecha, J. Gutiérrez, I. Gràcia, C. Cané and M. C. Horrillo, *Sensor. Actuat. B-Chem.*, 2011, **154**, 199-205.
12. M. Fang, K. Vetelino, M. Rothery, J. Hines and G. C. Frye, *Sensor. Actuat. B-Chem.*, 1999, **56**, 155-157.
13. E. J. Staples, *http://www.estcal.com/tech_papers/papers/Environmental/Phenol.pdf.*
14. E. J. Staples, T. Matsuda and S. Viswanathan, *Environ. Strat. 21st Cent., Asia Pacific Conf.*, 1998.
15. B. Sutapun, M. Tabib-Azar and A. Kazemi, *Sens. Actuators, B*, 1999, **60**, 27-34.
16. B. Michael, P.C. Kevin, B. Matrika, R.S. Philip and M. Mokhtar, *IEEE Photon. Technol. Lett.*, 2007, **19**, 255-257.
17. K. Schroeder, W. Ecke and R. Willsch, *Opt. Laser Eng.*, 2009, **47**, 1018-1022.
18. H.J. Patrick, A.D. Kersey and F. Bucholtz, *J. Lightwave Technol.*, 1998, **16**, 1606-1612.
19. A. Cusano, P. Pilla, L. Contessa, A. Iadicicco, S. Campopiano, A. Cutolo, M. Giordano and G. Guerra, *Appl. Phys. Lett.*, 2005, **87**, 234105.
20. J. Zhang, X. Tang, J. Dong, T. Wei and H. Xiao, *Sensor. Actuat. B-Chem.*, 2009, **135**, 420-425.
21. B. Liedberg, C. Nylander and I. Lunström, *Sensor. Actuat.*, 1983, **4**, 299-304.
22. C. de Julián Fernández, M. G. Manera, G. Pellegrini, M. Bersani, G. Mattei, R. Rella, L. Vasanelli and P. Mazzoldi, *Sensor. Actuat. B-Chem.*, 2008, **130**, 531-537.
23. K.-J. Chen and C.-J. Lu, *Talanta*, 2010, **81**, 1670-1675.
24. T. Karakouz, A. Vaskevich and I. Rubinstein, *The Journal of Physical Chemistry B*, 2008, **112**, 14530-14538.
25. A. Ksendzov, M. L. Homer and A. M. Manfreda, *Electron. Lett.*, 2004, **40**, 63-65.
26. S.I. Shopova, I.M. White, Y. Sun, H. Zhu, X. Fan, G. Frye-Mason, A. Thompson and S-J Ja, *Anal. Chem.*, 2008, **80**, 2232-2238.

27. Y. Sun, J. Liu, D.J. Howard, G. Frye-Mason, A.K. Thompson, S-J Ja and X. Fan, *Analyst*, 2010, **135**, 165-171.
28. N. A. Yebo, P. Lommens, Z. Hens and R. Baets, *Opt. Express* 2010, **18**, 11859-11866.
29. J. Villatoro, M. P. Kreuzer, R. Jha, V. P. Minkovich, V. Finazzi, G. Badenes and V. Pruneri, *Opt. Express*, 2009, **17**, 1447-1453.
30. G. Gauglitz, A. Brecht, G. Kraus and W. Nahm, *Sensor. Actuat. B-Chem.*, 1993, **11**, 21-27.
31. R. K. D. Reichl, C. Krumme, and G. Gauglitz, *Appl. Spectrosc.*, 2000, **54**, 583-586.
32. J. Zhang, M. Luo, H. Xiao and J. Dong, *Chem. Mater.*, 2006, **18**, 4-6.
33. J. Liu, Y. Sun and X. Fan, *Opt. Express*, 2009, **17**, 2731-2738.
34. J. Liu, Y. Sun, D.J. Howard, G. Frye-Mason, A.K. Thompson, S-J Ja, S-K Wang, M. Bai, H. Taub, M. Almasri and X. Fan, *Anal. Chem.*, 2010, **82**, 4370-4375.
35. C. Martínez-Hipatl, S. Muñoz-Aguirre, G. Beltrán-Pérez, J. Castillo-Mixcóatl and J. Rivera-De la Rosa, *Sensor. Actuat. B-Chem.*, 2010, **147**, 37-42.
36. K. Reddy, Y. Guo, J. Liu, W. Lee, M. K. Khaing Oo and X. Fan, *Sensor. Actuat. B-Chem.*, 2011, **159**, 60-65.
37. M. Agah, J.A. Potkay, G. Lambertus, R. Sacks and K.D. Wise, *J. Microelectromech. Sys.*, 2005, **14**, 1039-1050.
38. J. Liu, N. K. Gupta, K. D. Wise, Y. B. Gianchandani and X. Fan, *Lab Chip*, 2011, **11**, 3487-3492.

Chapter IV

Self-referenced composite Fabry-Pérot cavity vapor sensors

4.1 Introduction

The Fabry-Pérot (FP) cavity holds great promise in developing on-chip miniaturized sensor arrays for non-destructive, rapid, and sensitive vapor detection.[1-7] It is particularly attractive for on-column sensing applications in micro-gas chromatography (μGC), as it is highly compatible with microfluidics.[3,4,6,7] An FP vapor sensor consists of a vapor sensitive polymer coated on a solid substrate (*e.g.*, silicon wafer or glass slide). As shown in Fig. 4-1, light reflected from the air-polymer interface and polymer-substrate interface forms an interference pattern. The interaction between the polymer and vapor analyte causes a change in the polymer thickness and refractive index (RI), which in turn results in a change in the reflection spectrum (Fig. 4-1(B)). Thus, by measuring the reflection spectrum shift, the change in the polymer thickness and RI, and hence the concentration of the analyte, can be quantified. Usually such spectral domain measurements involve a bulky spectrometer, and are often slow and limited by the spectral resolution of the spectrometer. A tunable diode laser has also been employed to

Published: Karthik Reddy, et al. Optics Express, 20, 901-905 (2012). The Optical Society.

measure the FP sensor spectral shift.[3] While providing a high spectral resolution, the tunable diode laser is expensive and has a limited tuning speed and range.

A third method is to fix the incident laser wavelength at a quadrature point of the FP interference spectrum and then monitor the light intensity change (see Fig. 4-1(B)).[4,6,7] This method is simple, fast, sensitive, and amenable to integration of all components (light source, sensor, and detector) on a single chip. However, in practice, the light intensity measurement method encounters a hurdle. While most experimental conditions can be controlled precisely, the thickness of the polymer layer, which is usually deposited on a solid substrate through drop-coating, dip-coating, or spin-coating, may vary significantly from batch to batch. Such variations adversely cause the detection wavelength to deviate from the most sensitive quadrature point and thus results in different detection sensitivities that negate analyte quantitation. This problem is exacerbated when an array of sensors is employed with different polymer coatings that may have different thicknesses (and different RIs, as well).[6,7] Simultaneously achieving the optimal detection conditions for all those sensors becomes virtually impossible.

Here, we develop a self-referenced composite FP cavity sensor that enables precise measurement of the change in the polymer thickness and RI, and hence quantification of analytes, without prior knowledge of the polymer thickness. The composite FP is illustrated in Fig. 4-2. It is formed by two juxtaposed independent FPs with a slight polymer thickness offset. Although the polymer thicknesses (t and t+d in Fig. 4-2) are unknown, the offset (d in Fig. 4-2) can be precisely controlled during the fabrication, thus allowing us to accurately extract the change in the polymer thickness and RI upon exposure to the vapor analyte. This design retains all the benefits of standard single FP sensors, including ease of fabrication and implementation, excellent compatibility with micro-gas chromatography (μGC) components,[8-12] and rapid detection of analytes, while providing several significant advantages. First, the composite FP is able to precisely measure the thickness and RI change of the polymer, regardless of the polymer thickness, RI, and light incident angle and wavelength, thus enabling accurate vapor quantitation. Second, the detection becomes much more flexible, as nearly any wavelength and incident angle can be used without the need for precisely interrogating the sensor at a quadrature. Third, since the composite FP provides the actual change in polymer thickness and RI, it has a larger dynamic range, as compared to the measurement at a quadrature.

In this chapter we first discuss the underlying detection theory, and report the fabrication and characterization of the composite FP sensor. Then the tests of the composite FP sensor are performed under the pulsed vapor analyte flow at two different light incident angles. Rapid and consistent measurement of the polymer changes is achieved with three different analytes of various concentrations. The detection limit is found to be on the order of a few picograms.

4.2 Theory

Referring to Fig. 4-2, the reflected light intensity at FP #1 is given by:

$$I_1(\lambda) = R_{a-p} + R_{p-s} + 2 \times \sqrt{R_{a-p} R_{p-s}} \cos\phi, \qquad (4.1)$$

where $R_{a\text{-}p}$ and $R_{p\text{-}s}$ are the reflectivity at the air-polymer interface and polymer-substrate interface, respectively. $\phi = 4\pi \cdot n \cdot t \cdot \cos\delta / \lambda$, where n and t are the polymer RI and thickness, respectively. δ and λ are the incident angle in the polymer and the wavelength in vacuum, respectively. The light intensity change caused by the vapor-polymer interaction is described by:

$$\Delta I_1 = -8\pi \cos\delta / \lambda \times \sqrt{R_{a-p} R_{p-s}} \sin(\phi) \Delta(nt), \tag{4.2}$$

In vapor sensing applications, $\Delta(nt)$ can be used to quantify the analyte. However, in a regular FP sensor, since the polymer thickness (and hence ϕ) varies significantly, relating the intensity change, ΔI_1, to $\Delta(nt)$ becomes quite challenging.

This obstacle can be overcome by introducing another FP sensor, adjacent to the first one, with an additional thickness, d. Similar to Eq. (4.2) and under the assumption that the vapor causes the same polymer response ($\Delta(nt)$) in FP #2, we have,

$$\Delta I_2 = -8\pi \cos\delta / \lambda \times \sqrt{R_{a-p} R_{p-s}} \sin(\phi + \theta) \Delta(nt), \tag{4.3}$$

where $\theta = 4\pi \cdot n \cdot d \cdot \cos\delta / \lambda$. From Eqs. (4.1) - (4.3), we obtain:

$$\Delta(nt) = A \frac{\sqrt{(\Delta I_1)^2 + (\Delta I_2)^2 - 2\cos\theta \cdot \Delta I_1 \cdot \Delta I_2}}{\sin\theta}, \tag{4.4}$$

where A is a constant that contains the information about the light incident angle, wavelength, reflectivities at the two interfaces, and the detector responsivity. Note that in Eq. (4), $\Delta(nt)$ is no longer dependent upon the polymer thickness, t, but only the polymer thickness difference, *d*. As shown later, *d*, can be created through the micro/nanolithographic method with high precision and high reproducibility. Therefore, $\Delta(nt)$ can be obtained uniquely by measurement of the reflected light intensity change at the two sensors, thus enabling rapid and accurate quantification of the vapor analyte. Also note that in the above derivation, we assume that the vapor causes the same polymer response (*i.e.*, $\Delta(nt)$) in both FP #1 and #2. This is true when the vapor is in the pulsed format and the exposure time of the polymer to the vapor is short so that only the superficial layer of polymer is affected.

4.3 Experimental

4.3.1 Sensor preparation

The fabrication procedure for the composite FP is illustrated in Fig. 4-3(A). The prime grade silicon wafers are spin-coated with a photoresist and lithographically patterned using an MA-6. The wafers are then etched using a Pegasus deep reactive ion etching (DRIE) tool (etch depth, d=1.3 μm). The etched wells are 400 μm long and 200 μm wide. The first layer of photoresist is removed, and the wafer is then recoated with photoresist and patterned with precise alignment using the MA-6. The wafers are once again etched using the DRIE tool (etch depth, t=1 μm). The resulting etched area is 400 μm long and 400 μm wide, and is aligned to overlap with the previously etched area. This results in a staggered etch, with half of the total etched area etched to a depth of 2.3 μm and the other half etched only 1 μm (Fig. 4-3(B)). The resultant silicon wafer is then diced into 8 mm x 10 mm pieces using an ADT 7100 dicing saw. These pieces are immersed overnight in sulfuric acid-dichromate solution to oxidize any contaminants, followed by a rinse with deionized water, and finally placed under UV light for an hour to ensure removal of any residues. Then OV-215 (Ohio Valley Specialty, 1057) is chosen as the vapor sensing layer, as it is a commonly used in many GC applications and vapor sensors.[7,13] The polymer solution is prepared by dissolving the polymer gum in ethyl acetate (OV-215:ethyl acetate=1:3 in mass). The polymer is then coated using a spin coater to achieve a smooth layer. The polymer solution is first spun at 1,300 rpm for 10 seconds and then at 6,000 rpm for 30 seconds. The spin-coated chip is subsequently heated for 60 seconds at 60 ^{o}C to completely remove the solvent. Finally, an open-bottom microfluidic channel assembled from glass slides and UV-curable optical glue is used to seal the silicon chip (Fig. 4-3(C)). The resulting channel is approximately 1 mm deep and 600 μm wide.

4.3.2 Experimental setup

The experimental setup is illustrated in Fig. 4-3(D). Analytes are injected using a standard GC injection port and the analyte in the pulsed format is then delivered to the sensor via a 4 m long GC guard column (inner diameter: 250 μm). The detection beam from a Toptica 785 nm laser is aligned using an FC/APC terminated optical fiber and a beam collimator. A Thorlabs CMOS imager, with an acquisition rate of 16 frames per second, is used to acquire the light reflected from each FP sensor through a lens (Edmund Optics, VZM450). The precise and instantaneous transduction signal from the FP sensor is captured for post-analysis. All experiments are carried out at room temperature. Mass of the injected analytes is calibrated using a mass spectroscopy system. Helium is used as the carrier gas with a flow rate of 8 mL/min.

4.4 Results and discussion

In the experiment, we choose to use two different incident angles, 21^{o} and 26^{o}, to intentionally create a situation that deviates from the traditional quadrature detection. The temporal response of each individual sensing element (FP #1 and #2 in Fig. 4-2) of the composite FP sensor is shown in Fig. 4-4. Introduction of analyte from the GC injection port leads to a rapid rise in the measured signal, corresponding to the shift in the interference spectrum. This increase is attributed to the change in polymer thickness and RI as the analyte is absorbed by the polymer. Subsequently, the gas flow in the GC and microfluidic column rapidly purges the analyte from the polymer, resulting in a rapid decline back to the baseline in the measured signal. The chromatograms reveal a sub-second response time when each individual FP sensing element is interrogated at both 21^o and 26^o angles of incidence. However, comparison among Fig. 4-4(A)-(D) shows the strong influence of polymer thickness and angle of incidence on the sensor response to the injected vapor analyte. According to Fig. 4-4(A) and (B), at 21^o incident angle, FP #1 has a peak height of 25.15, while FP #2 has a peak height of 17.12. This difference is due to the different thickness of polymer layer in each individual FP sensing element. Similar difference (23.11 counts vs. 13.5 counts) can also be found for FP #1 and #2 at 26^o incident angle, as shown in Fig. 4-4(C) and (D). Likewise, different incident angles also cause different sensitivities even in the same FP sensor due to the slight light path difference in the polymer. These variations highlight the difficulties in obtaining accurate quantitation of the vapor analyte.

In contrast, by using the information gained from the self-referenced composite FP sensor (*i.e.*, both FP #1 and #2), Δ(nt) can be calculated very precisely. Based on Eq. (4-4), Δ(nt) in Fig. 4-4 is 26.88 and 26.72 for the 21^o and 26^o incident angle, respectively, which represents a variation of only 0.4%. Fig 4-5 presents the calculated Δ(nt) at 21^o and 26^o for three different vapor analytes, acetone, heptane, and toluene, at various injected masses. It clearly shows that for each analyte the calculated Δ(nt) is nearly equal at both angles of incidence across the entire range of injected mass. Therefore, Δ(nt) can be used for analyte quantitation regardless of the polymer thickness or incident angle (Note: for some angles at which $\sin(\theta)=0$, our approach becomes invalid). Linear response is obtained when the injected mass is below approximately 4 ng. At higher injected masses, $\Delta(nt)$ levels off due to the polymer saturation. Additionally, these sensors maintain the high sensitivity and low detection limits previously reported. Given the noise level of 0.38, the detection limit for acetone, heptane, and toluene is about 5.7 pg, 9 pg, and 11 pg or, based on the retention time (~4 s) and the peak width (0.125-0.15 s), as well as the inner diameter and length of the GC column, which correspond to approximately 200 ppb, 335 ppb, and 405 ppb in concentration, respectively (Appendix III).[7] These results are comparable to the best results demonstrated by traditional single FP sensors under the optimal quadrature detection condition.[7]

4.5 Conclusion

We have developed a self-referenced composite FP vapor sensor to overcome the sensitivity variations caused in batch to batch processing of polymers. The sensor provides accurate measurement of the change in polymer thickness and RI, thus enabling vapor quantitation. The sensor can be used with nearly any polymer thickness, RI, and light incident angle and wavelength. These advantageous features, coupled with the use of a single optical source and single optical detector (CMOS imager), make the composite FP sensor a promising technology platform in various applications, including vapor sensing as demonstrated in this chapter, pressure sensing, protein detection,[14] and photo-acoustic imaging.[15,16]

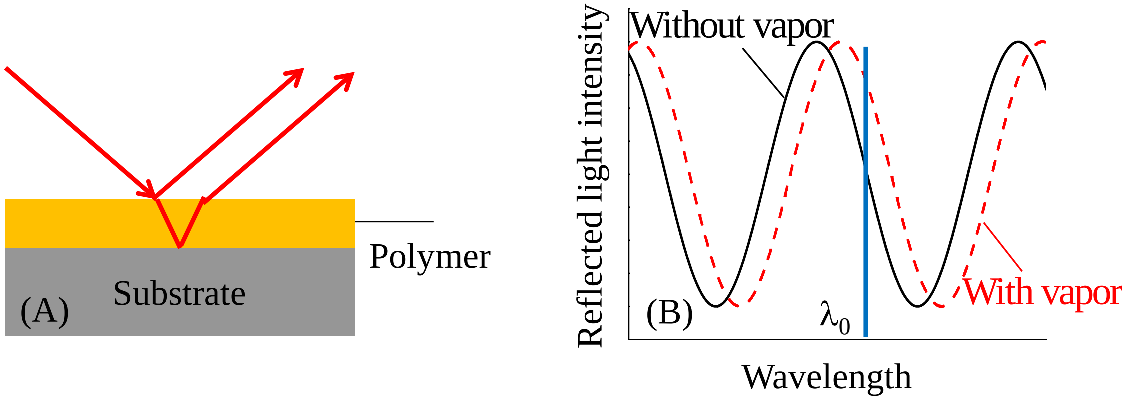

Figure 4-1 (A) Side view of an on-chip Fabry-Pérot (FP) sensor. Absorption of analytes by polymer results in a change in thickness and/or refractive index of the polymer, which in turn leads to a change in the characteristic FP spectrum as shown in (B). The shift in the spectrum can be measured as a change in reflected intensity at a fixed wavelength.

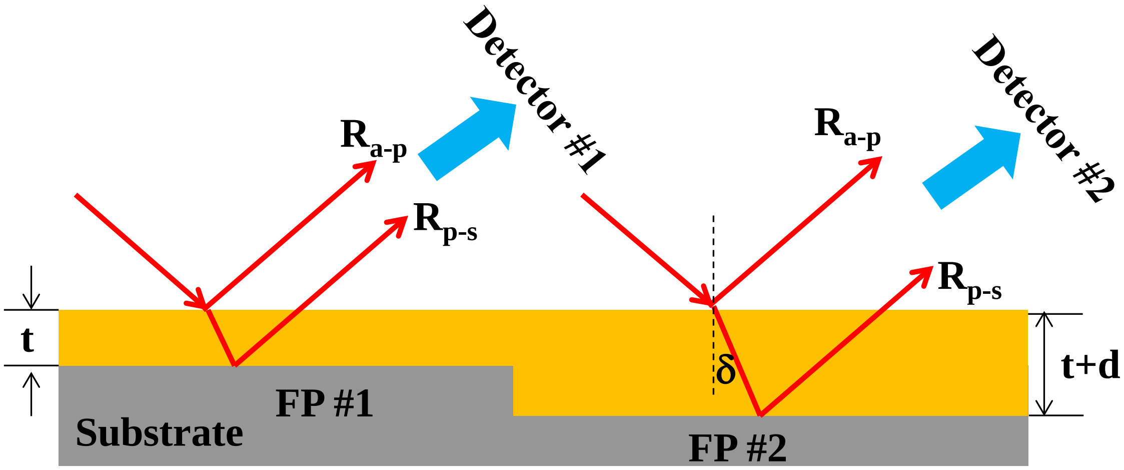

Figure 4-2 Schematic of the self-referenced composite FP sensor.

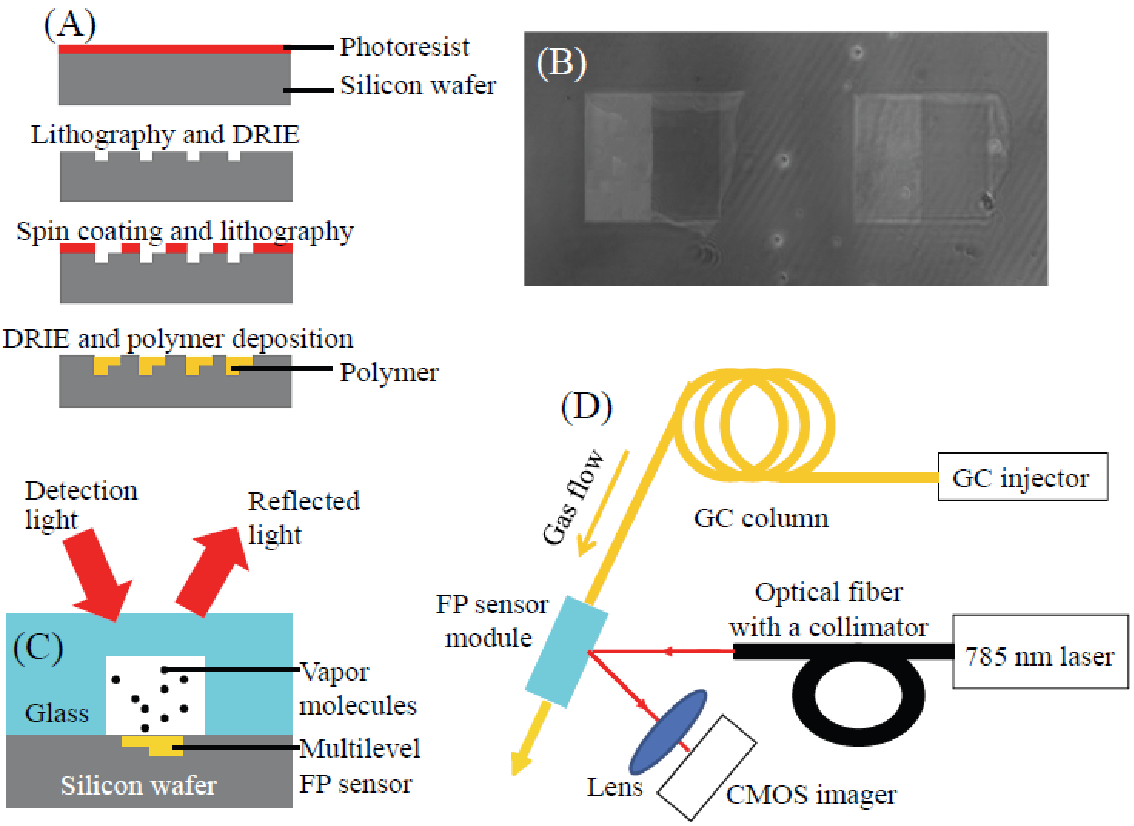

Figure 4-3 (A) Fabrication of a composite FP sensor. The sensors are fabricated using a two-step lithography and deep reactive etching process. Polymers are spin-coated or drop-coated on the wafer. (B) Image of the composite FP sensor acquired using a CMOS imager. Each well is 400 μm long and 200 μm wide. The depth offset (*i.e.*, d in Fig. 2) is 1.3 μm. (C) Cross-sectional view of the composite FP sensor on a silicon substrate enclosed by an open-bottom glass microfluidic channel (1 mm deep and 600 μm wide). (D) Schematic of the experimental setup.

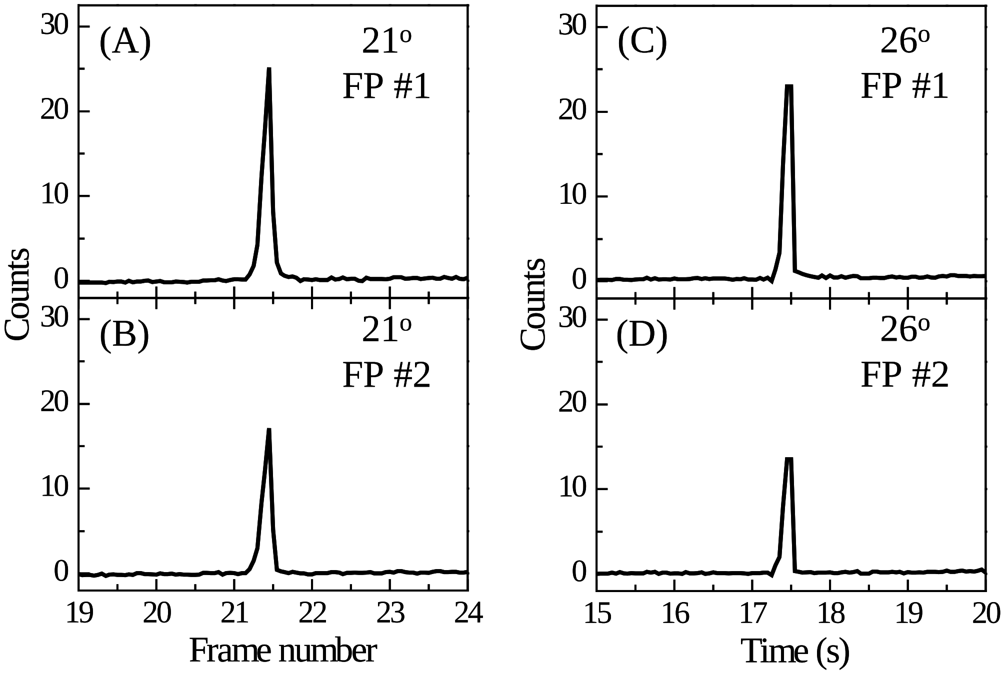

Figure 4-4 Response of individual FP sensing elements in the composite FP sensor to 40 ng of acetone at the incident angle of 21° and 26°. In all cases the sensors demonstrate a rapid response time in the sub-second range. Δ(nt) at 21° is 27.09 and Δ(nt) at 26° is 27.20, based on Eq. (4.4) (assuming that A=1 in Eq. (4.4)).

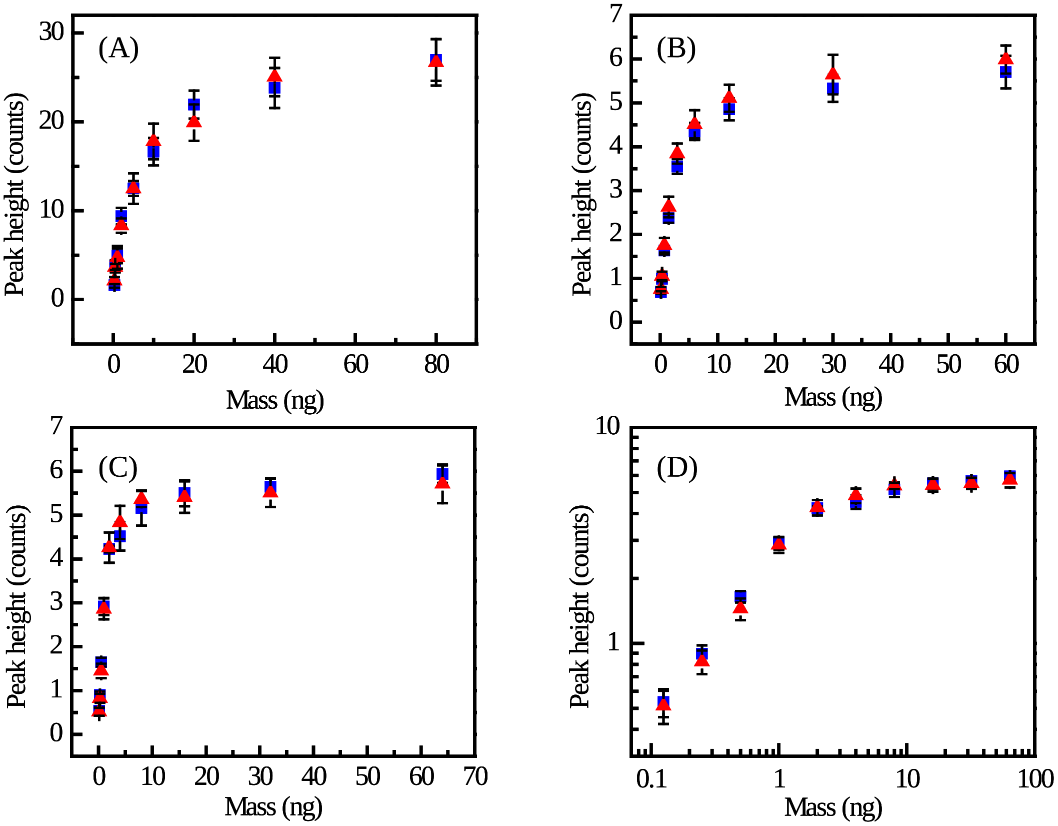

Figure 4-5 Response of sensors at 21° (squares) and 26° (triangles) to various injected masses of (A) acetone, (B) heptane, (C) toluene. (D) Log-log plot corresponding to (C). Error bars are obtained from 5 tests.

References

1. G. Gauglitz, A. Brecht, G. Kraus and W. Nahm, *Sensor. Actuat. B-Chem.*, 1993, **11**, 21-27.
2. D. Reichl, R. Krage, C. Krumme and G. Gauglitz, *Appl. Spectrosc.*, 2000, **54**, 583-586.
3. J. Liu, Y. Sun and X. Fan, *Opt. Express*, 2009, **17**, 2731-2738.
4. J. Liu, Y. Sun, D. J. Howard, G. Frye-Mason, A. K. Thompson, S.-J. Ja, S.-K. Wang, M. Bai, H. Taub, M. Almasri and X. Fan, *Anal. Chem.*, 2010, **82**, 4370-4375.
5. C. Martínez-Hipatl, S. Muñoz-Aguirre, G. Beltrán-Pérez, J. Castillo-Mixcóatl and J. R.-D. l. Rosa, *Sens. Actuators B*, 2010, **147**, 37-42.
6. K. Reddy, Y. Guo, J. Liu, W. Lee, M. K. Khaing Oo and X. Fan, *Sensor. Actuat. B-Chem.*, 2011, **159**, 60-65.
7. K. Reddy, Y. Guo, J. Liu, W. Lee, M. K. Khaing Oo and X. Fan, *Lab Chip*, 2011, **12**, 901-905.
8. H.-s. Noh, P. J. Hesketh and G. C. Frye-Mason, *J. Microelectromech. Syst.*, 2002, **11**, 718-725.
9. M. Agah, J. A. Potkay, G. Lambertus, R. Sacks and K. D. Wise, *J. Microelectromech. Syst.*, 2005, **14**, 1039-1050.
10. S. C. Terry, J. H. Jerman and J. B. Angell, *IEEE Trans. Electron Devices*, 1979, **26**, 1880-1886.
11. G. R. Lambertus, C. S. Fix, S. M. Reidy, R. A. Miller, D. Wheeler, E. Nazarov and R. Sacks, *Anal. Chem.*, 2005, **77**, 7563-7571.
12. S. Reidy, D. George, M. Agah and R. Sacks, *Anal. Chem.*, 2007, **79**, 2911-2917.
13. E. T. Zellers, S. A. Batterman, M. Han and S. J. Patrash, *Anal. Chem.*, 1995, **67**, 1092-1106.
14. E. Özkumur, J. W. Needham, D. A. Bergstein, R. Gonzalez, M. Cabodi, J. M. Gershoni, B. B. Goldberg and M. S. Ünlü, *Proc. Natl. A. Sci.*, 2008, **105**, 7988-7992.
15. P. C. Beard, *Meas. Sci. Technol.*, 2003, **14**, 1998.
16. Y. Hou, S.-W. Huang, R. Witte, M. O’Donnell and S. Ashkenazi, *J. Biomed. Opt.*, 2008, **13**, 064033-064038.

Chapter V

Integrated separation columns and Fabry-Pérot sensors for micro-gas chromatography systems

5.1 Introduction

The increasing need for on-site volatile organic compound (VOC) detection has led to intense development of micro-gas chromatography (μGC) systems.[1-4] A typical μGC system utilizes several silicon or MEMs based components, including pre-concentrators,[5-7] separation columns,[8-13] and detectors.[14-23] Traditionally, each of those components is fabricated separately and then connected together. While fabrication of stand-alone components is relatively straightforward, the subsequent assembly is mainly accomplished manually, which is time-consuming, prone to errors, and incompatible with future mass-production. In addition, the system such made is not only large in footprint, but also has a dead volume resulting from interconnects,[24-26] which may adversely affect the μGC performance. Therefore, a monolithic sub-system that integrates multiple components on a single-chip is highly desirable.

Published: Karthik Reddy, et al. IEEE Journal of Microelectromechanical Systems, 5. IEEE.

As the first step towards a completely integrated μGC system, here we aim to incorporate the separation columns with vapor sensing elements. In particular, we are interested in developing an on-column non-destructive vapor sensor (or sensors) that can detect VOCs traveling through the microfluidic channel without interruption to or interference with the flow, thus providing unique capability for novel μGC designs.[27] On-column non-destructive vapor sensors have previously been demonstrated using thermal conductivity detectors (TCDs).[28] In particular, progress has recently been made towards integrating the TCD with the separation columns.[29-31] On-column non-destructive vapor sensing has also been carried out with optical sensors such as capillary based optical ring resonators,[20,32-34] Fabry-Pérot (FP) sensors fabricated on an optical fiber facet,[27,35-37] and stand-alone FP sensors fabricated on a silicon chip,[19,38] which have very small footprint (micron size), an excellent detection limit (~1 pg), and ability to perform arrayed detection.

In this work, we introduce two designs that integrate the μGC separation column with on-chip FP sensors. In the first design illustrated in Fig. 5-1(A), the microfabricated column is coated with a layer of polymer that serves as both the stationary phase and the FP sensor. The advantages of this design include (1) significantly simplified integration of the column and vapor sensor, (2) elimination of the dead volume arising from the column/sensor connection, and (3) built-in vapor sensor along the column (detection can be carried out at any location and multiple detection positions can also be implemented so that the separation process can be monitored in real-time[20]). On the other hand, this design has several drawbacks because it lacks flexibility in selecting polymers (as the polymer is the same as that for the stationary phase) and it may be difficult to simultaneously optimize the polymer coating for both separation and sensing. Usually the polymer and its coating processes are optimized for best separation. As a result, the sensing performance may be compromised.

Another design illustrated in Fig. 5-1(B) overcomes the aforementioned issues. The separation column and sensors are fabricated on the same monolithic chip. Meanwhile, different polymers and coating processes are used so that both stationary phase and FP sensor are optimized for best separation and sensing, respectively. In addition, multiple FP sensors can be built with different polymers to generate response patterns for better identification of VOCs.[19]

5.2 Materials, fabrication and methods

5.2.1 Materials

Silicon and Pyrex wafers were purchased from University Wafer (South Boston, MA). UV-curable optical glues were purchased from Dymax (Torrington, CT) and Norland (Cranbury, NJ). OV-1 (Polydimethylsiloxane or PDMS), OV-215 (Trifluoropropylmethylsilicone), and OV-1701 (Dimethylphenyl cyano substituted) were purchased from Ohio Valley Specialty (Marietta, OH). GC guard column (part no. 10029, inner diameter 250 µm) was purchased from Restek (Bellefonte, PA) and universal quick seal column connectors were purchased from Varian (Palo Alto, CA). All analytes and solvents used in the experiments were purchased from Sigma (St. Louis, MO) and had purity greater than 97%. All materials were used as received.

5.2.2 Fabrication

OV-1 and OV-215 were chosen for use as the stationary phase and OV-1, OV215, or OV-1701 was used as the vapor sensing polymer coating. The polymer solutions were prepared by dissolving the polymer gum in their corresponding solvent. For use in separation column stationary phase, OV-1 was diluted with a mixture of 1:1 (v:v) pentane and dichloromethane (OV-1:pentane/dichloromethane=10 mg:3 mL), whereas OV-215 solution was prepared by dissolving 20 mg OV-215 and 0.2 mg dicumyl peroxide in a 5 mL mixture of 1:4 (v:v) ether and ether acetate. For the purpose of the sensors OV-1 was diluted with toluene (PDMS:toluene=10 mg:1 mL), OV-1701 was diluted with pentane (OV-1701:pentane=10 mg:1 mL), and OV-215 was diluted with ethyl acetate (OV-215:ethyl acetate=10 mg:1 mL).

For the first design, the µGC column was fabricated using an MA-6 and STS Pegasus-4 for lithography and deep reactive ion etching of a 25-cm channel, with a footprint of only 1.1 cm^2. Then a Pyrex cover sheet was anodically bonded to the silicon substrate to seal the channel. The rectangular cross section of the channel was 150 µm by 240 µm. Finally the channel was coated with the desired polymer by (OV-1 or OV-215) (1) filling the column with the previously prepared coating solution and holding for 5 min; (2) evaporating the solution from one end of the column using a vacuum pump while the sealing the other end with a septum; (3) cross-linking the polymer to the inner wall of the column by ramping the column temperature from 160 ^oC to 180 ^oC at a rate of 0.2 ^oC/min and staying at 180 ^oC for one hour. The resultant column coating had a uniform thickness of around 200 nm. The fabricated column is shown in Fig. 5-1(C).[39]

The complete fabrication procedure for the second design (*i.e.*, the integrated separation column and FP sensor array) is illustrated in Fig. 5-2 and Fig. 5-3. First, three 1.2-µm deep wells were etched into the prime grade silicon. These wells were designed to act as containment for polymers as well as visual markers for subsequent optical vapor detection (see Section 2.3). Each well was 200 µm x 200 µm and were separated by 800 µm. Next, the silicon was patterned and etched to form the serpentine separation column. Close attention was paid to alignment so that the etched wells were within the column. The column was approximately 400 µm deep and 120 µm wide. The higher aspect ratio of these columns compared to the first design allows for better performance at higher flow rates. There is no change in sensitivity of the polymers to analytes arising from the change in column dimensions. Then, a shadow mask was fabricated by through-etching a silicon wafer such that the holes aligned with the containment wells on the first silicon wafer. After alignment, we created an FP sensor array by spray-coating the aforementioned polymer solutions, using an Iwada HP-B+ airbrush, onto the pre-etched wells. The polymer thickness can be controlled by the coating time and polymer solution concentration. For the present work, all polymer coatings were approximately 1 µm thick. By using the shadow mask and spray-coating, cross contamination of polymers between the adjacent wells is eliminated. In the final step, a diced Pyrex wafer was bonded to the silicon wafer using UV-curable optical glue prior to static coating of the column with OV-1. The optical glue was carefully applied to the devices to minimize contamination of the channels. Also, once cured the optical glue is very inert and should have no effect on the analytes. The bond can tolerate up to at least 10 psi flow pressure which is sufficient for µGC applications. The optical glue used has a thermal limit of 190 ^{o}C, which imposes an upper limit on the maximum operating temperature of this system.

To prevent any overflow of the stationary phase solution onto the sensor array we designed a stationary phase solution outlet near the end of the separation column (see Fig. 5-1 (B)), through which the polymer solution was withdrawn from the gas inlet side while sealing the distal end of the device (*i.e.*, gas outlet near the FP sensor array). The detail of the stationary phase coating process is described in Fig. 5-3. The completed device is shown in Fig. 5-1(D). The dead volume due to the presence of the stationary phase solution outlet, which was sealed after the coating process was complete, is estimated to be less than 1 nL, much smaller than micro-liter dead volumes reported previously.[24-26]

The fabrication procedure which involves depositing polymer prior to bonding the silicon and glass substrates precludes the use of anodic bonding due to the high temperatures involved in the process. However, using an optical epoxy to bond the substrates lowers the yield and throughput substantially compared to regular µGC column fabrication. Issues arise from improper bonding and gaps in the substrate which necessitates extreme care during application of the adhesive. Additionally, we studied the potential outgassing effects of the adhesive the column during temperature ramping. In this case, a standard GC guard column, an anodically bonded µGC column coated with PDMS, and an uncoated µGC column bonded using an optical adhesive were tested with an FID. According to Fig. 5-4, the guard column shows a small change in the chromatographic response under temperature ramping, about 2 mV, the effect of the anodically bonded PDMS coated µGC column is about 6 times greater than the guard column, about 11 mV, and the uncoated optical adhesive bonded column has a response about 5 times larger than the anodically bonded column, about 55 mV. The above results indicate that there is indeed an outgassing effect due to the adhesive which will eventually affect the detection limit of the sensors. However the slow increase in the baseline and subsequent plateau that the baseline reaches when the temperature stabilizes does not resemble the sharp peaks the analytes produce.

5.2.3 Experimental setup

The experimental setup is illustrated in Fig. 5-5. Analytes were injected at the GC injection port and delivered to the FP sensors or sensors array through a 4-m long GC guard column. To illuminate the FP sensors a Toptica 785 nm laser was aligned using an FC/APC terminated optical fiber and a beam collimator. The principle of the FP vapor sensor is described in Chapter 2. The reflected beam was collected by a Thorlabs CMOS imager (product no. DCC1545M), attached to a lens (VZM450 from Edmund Optics) to capture all FP sensors simultaneously. The reference signal was also acquired from the laser light reflected from the bare silicon surface and used to remove any long term laser intensity drifts or false peaks caused by laser instability. The acquisition rate on the imager was set at 20 frames per second for all tests. To maximize the sensors' sensitivity by tuning the beam incident angle, a white light source was placed co-linearly with the laser beam and at the reflection side a spectrometer (Ocean Optics HR-2000) was used to monitor the interference spectrum (dashed lines in Fig. 5-5). The flow rate for testing individual analytes was set at 8 mL/min.

To test the separation capability of the columns, a liquid mixture containing multiple analytes was injected at the GC injection port. It was delivered to the microfabricated GC column to separate the mixture before detection by the FP sensor. The overall optical detection setup remained the same, as previously described. To enhance separation of analytes, the flow rate was done a multiple flow rates ranging from 1 mL/min to 4 mL/min. All experiments were carried out at room temperature with no heating of the columns or sensors. Mass of injected analytes was calibrated using a splitter and mass spectroscopy system. Helium was used as the carrier gas in all experiments.

5.3 Results and discussion

First, we tested the separation and sensing capability of the first design (Fig. 5-1(A)), where the stationary phase was also used as the vapor sensing polymer. Fig. 5-6(A & C) and Fig. 5-7 show the chromatograms obtained by injecting a mixture of three analytes (toluene, octane, and decane). The response rose rapidly in the presence of analyte and rapidly fell back to the baseline as the analyte was purged. The above result suggests that the polymer coating inside a μGC column can indeed be used for dual purposes (*i.e.*, stationary phase and sensing). Since the CMOS imager was operated at 20 frames per second, a system time resolution of 50 ms can be achieved. The sensitivity curves of the OV-1 and OV-215 stationary phase FP sensor are plotted in Fig. 5-6(B) and Fig. 5-6(D), respectively, revealing the dependence of the peak height on the injected analyte mass. To estimate the detection limit, we used the lowest data point in Fig. 5-6(B) in combination with the sensor noise level of approximately 0.1 counts. Decane exhibited the best detection limits of 2.6 ng and 6.1 ng for the OV-1 and OV-215 sensors, respectively, while octane and toluene had a detection limit of 4.6 ng and 10 ng, with OV-1 and 11.5 ng and 9.4 ng with OV-215. The principle of this design is valid regardless of polymer or its thickness.

While the design demonstrated above is superior in its level of integration and detection simplicity, the sensitivity is inferior to the optical vapor sensors that we have developed.[19] This low sensitivity can be attributed to thickness of the polymer (~200 nm), which is far thinner than previously demonstrated FP sensors, and the insufficient polymer coating uniformity when compared to spin or spray coated polymer layers, and therefore poses a challenge for this design to be considered in a viable μGC system without further significant improvement in the sensitivity.

In the second design (Fig. 5-1(B)), by separating the sensing element and separation column while keeping them on the same chip we can overcome the aforementioned issues and develop an integrated separation and sensing system. To characterize the device’s sensitivity, we placed the FP sensor array right after the 4-m long guard column by inserting it to the gas outlet on the chip (see Fig. 5-1(B)), thus bypass the μGC column. Each FP sensor was tested with three different analytes (acetone, toluene, and octane). The peak response of each sensor and analyte is shown in Fig. 5-8. The response is linear at lower injected mass and tends to saturate as the injected mass is increased. At the higher masses there is also peak broadening, which appears to indicate sensor overloading.

The interaction of analytes with polymers is affected by various factors including their polarities, functional groups, molecular weight, and volatility, *etc*. By using three different polymers with varying polarities it is possible to build a sensor array. Using a sensor array can be a valuable aid in analyte identification. Additionally, the sensor array can comprise polymers that are different from the polymer stationary phase, thereby increasing the flexibility of the system. From the sensitivity curves shown in Fig. 5-8 and Fig. 5-9, it is clear that different polymers have different sensitivities and different detection limits, depending on their interaction with each analyte. The best detection limit, calculated by using the lowest data point and a noise level of 0.1 counts, was found to be 40 pg for OV-1 and octane. While OV-1 also had the best detection limit for toluene at 44 pg, the best detection limit for acetone was exhibited by OV-215 at 80 pg. Based on the retention time (4-5 s) and the peak width (~0.25-0.4 s), as well as the inner diameter (250 µm) and length (4 m) of the GC guard column, the above detection limits, in concentration at atmospheric pressure, corresponds to about 504 ppb for octane, 700 ppb for toluene, and 900 ppb for acetone. While the detection limits of these sensors are not as low as those demonstrated by us previously (~30 ppb),[19,40] they are similar to the reported results for micro-TCD,[28] and carbon-nanotube FETs,[22] and better than those for chemi-resistors,[14] SAW sensors,[18] and microplasma detectors,[21] as well as the nano-resonator sensors developed recently that has a sub-ppb or attogram detection limit in theory, but only 1 ng detection limit in practical GC applications.[23] It is important to note that while different FP sensors may have slightly different noise levels, because of surface roughness of the polymer and scattering of the optical beam, these differences are very small and are not a major factor in the different detection limits of each sensor.

To demonstrate the separation capability of the column along with the rapid simultaneous detection of eluted analytes by the sensor array. Fig. 5-10(A) and Fig. 5-11 show the chromatograms obtained from each polymer for a mixture of 5 analytes separated, at different flow rates, by the integrated column/sensor system (Fig. 5-1(B) and (D)). Due to the high linear speed of the analyte traveling inside the microfluidic channel, all FP sensors in the array were able to detect the same analyte virtually simultaneously. The peak height is used to extract response patterns for each analyte. Figure 5-10(B-F) illustrate the response patterns for the injected mixture shown in Fig. 5-10(A). The response patterns clearly differ for each injected analyte, and concur with the previous testing results shown in Fig. 5-8 and Fig. 5-9. The error bars show a variation of less than 16% among runs, which will not limit the use of response patterns as a method of analyte identification in conjunction with the analyte retention time.

5.4 Conclusion

We have fabricated and characterized two sub-system designs that integrates the μGC column and FP sensor (array), which are robust, reproducible, and fast in response, and can potentially improve the efficiency and reduce the size of μGC systems. In particular, the second design where a sensor array was used demonstrates the ability to separate multiple analytes and simultaneously gather information from multiple sensors to conduct pattern analysis for qualitative and quantitative detection of VOC mixtures. The detection limit for the sensor is on the order of tens of picograms. Future work will focus on fabrication procedures, particularly polymer coating and low temperature substrate bonding, such as eutectic bonding,[41] to improve the yield and sensitivity. In addition, a subsystem with a higher level of integration will be developed, which will include on-chip pre-concentrators,[6,42,43] and on-chip thermal modulators or injector,[44] as well as temperature ramping.[45]

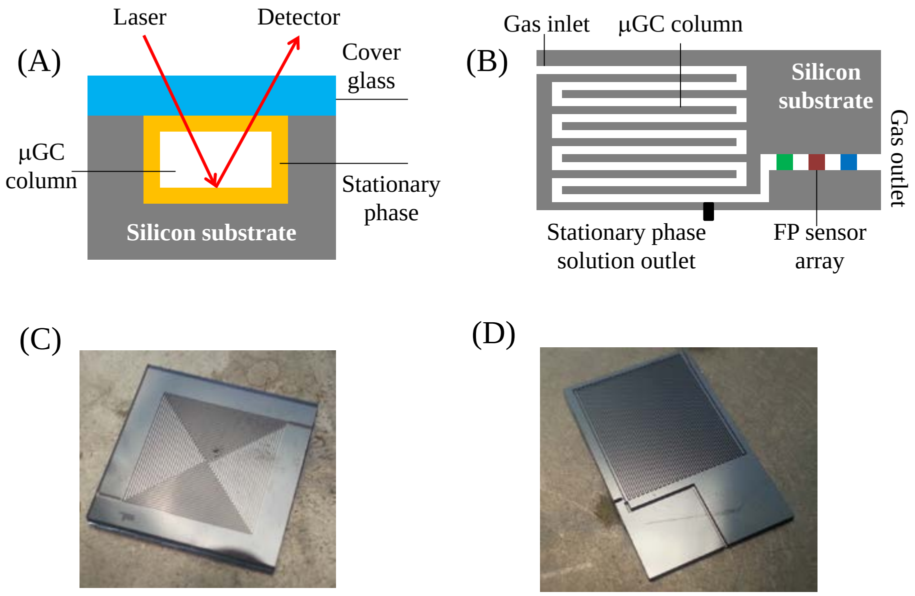

Figure 5-1 (A) Cross-sectional view of the first design to integrate the µGC column with the on-column vapor sensor, in which the polymer coating is used as both the stationary phase and the on-column FP vapor sensor. Detection can be carried out at any location along the column. (B) Top view of the second design to integrate the µGC column with the on-column FP vapor sensor array. Different polymer coating can be used for column and FP sensors. (C) Image of a 25-cm long µGC separation column fabricated on silicon based on the first design illustrated in (A). Column depth=150 µm and width=240 µm. (D) Image of fabricated integrated µGC separation column and the FP sensors based on the second design illustrated in (B). Column length=30 cm, depth=400 µm, and width=120 µm.

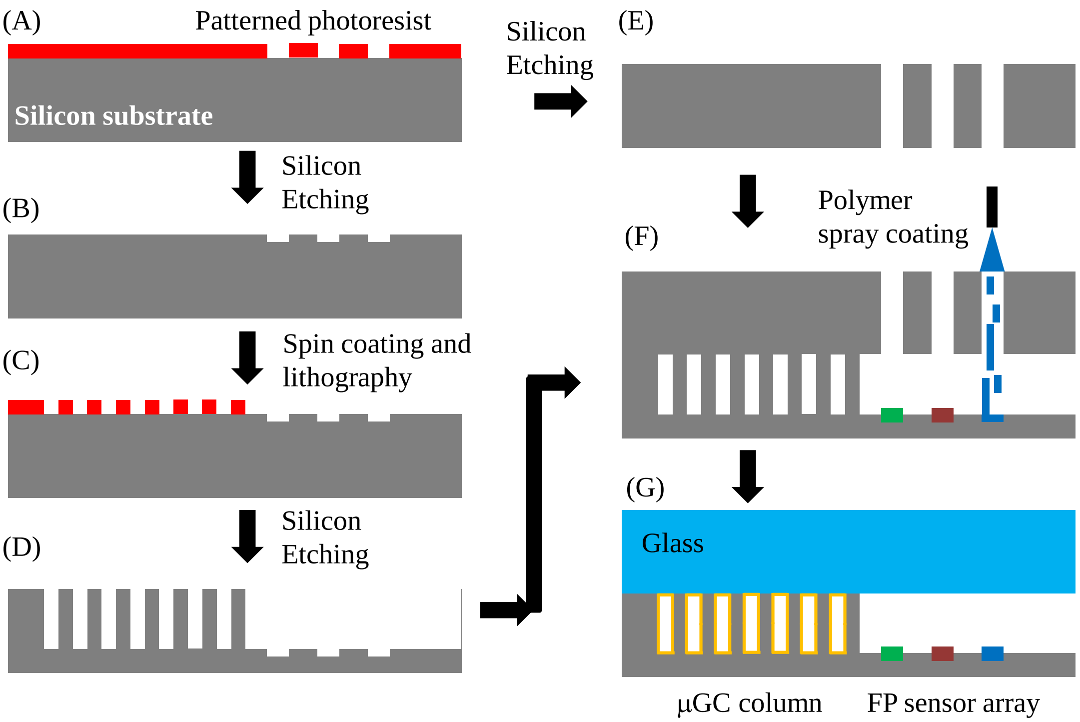

Figure 5-2 Fabrication process of the device for the second design. (A) Photoresist was spun onto silicon and patterned using UV photolithography. (B) 1-µm deep reactive ion etching (DRIE) of silicon to define the sensor area. (C) Photoresist was spun on the etched wafer and patterned with UV lithography. (D) The column was etched using DRIE. (E) Shadow mask fabricated by DRIE through etching of another silicon wafer. (F) Spray-coating of the sensor polymers at desired locations with aid of the shadow mask. (G) Glass top wafer was bonded to the silicon wafer and the column was coated with polymer as a stationary phase.

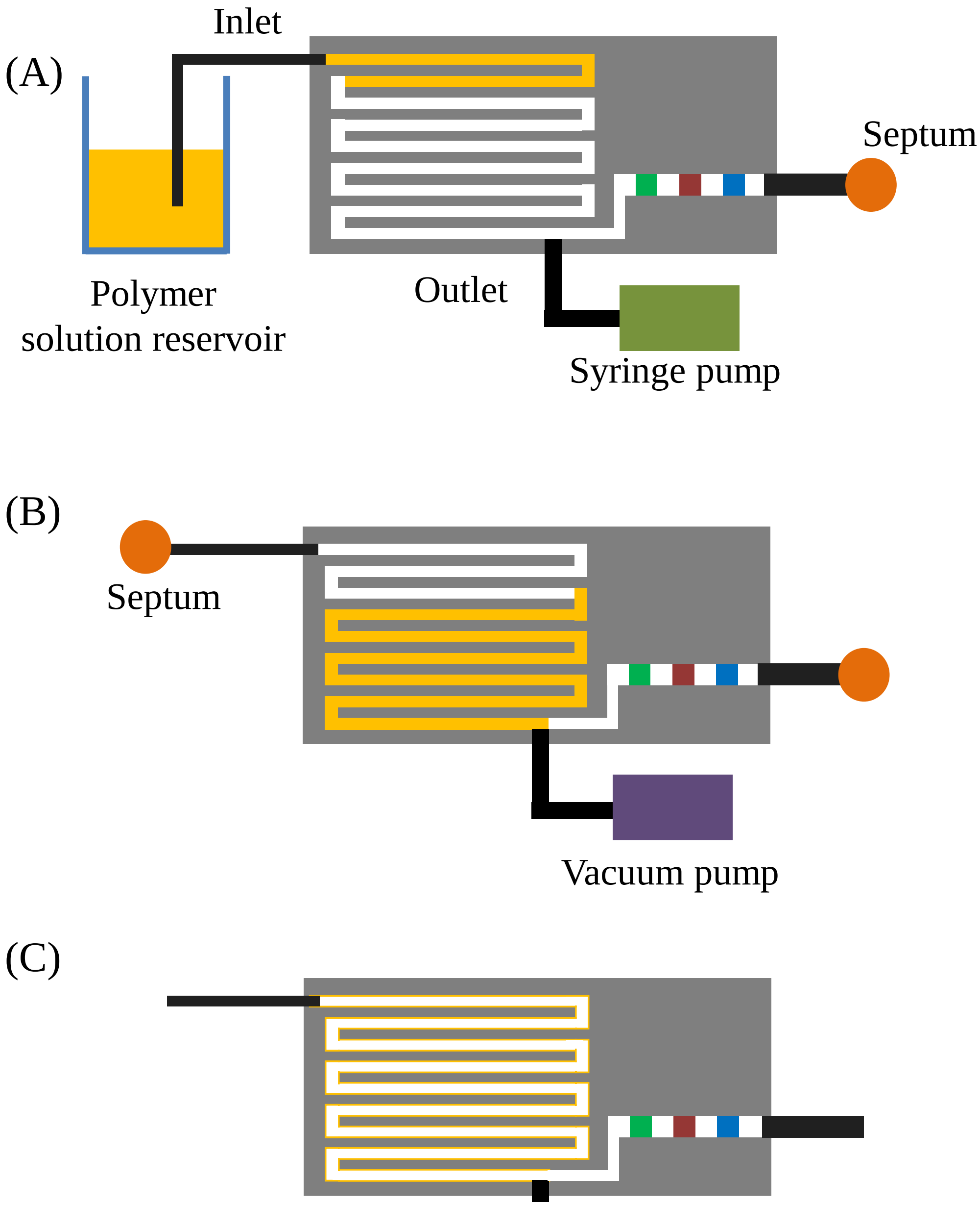

Figure 5-3 The channel was coated with the desired polymer by (OV-1) (A) Sealing the distal end of the chip and filling the column with the previously prepared coating solution, using a syringe pump and holding for 5 min; (B) Evaporating the solution from one end of the column using a vacuum pump while sealing the inlet with a septum; cross-linking the polymer to the inner wall of the column by ramping the column temperature from 160 ^{o}C to 180 ^{o}C at a rate of 0.2 ^{o}C/min and staying at 180 ^{o}C for one hour. (C) Finally, the septum was removed and the outlet was permanently sealed with optical glue. The resultant column coating had a uniform thickness of around 200 nm. The dead volume introduced by the solution outlet is less than 1 nL.

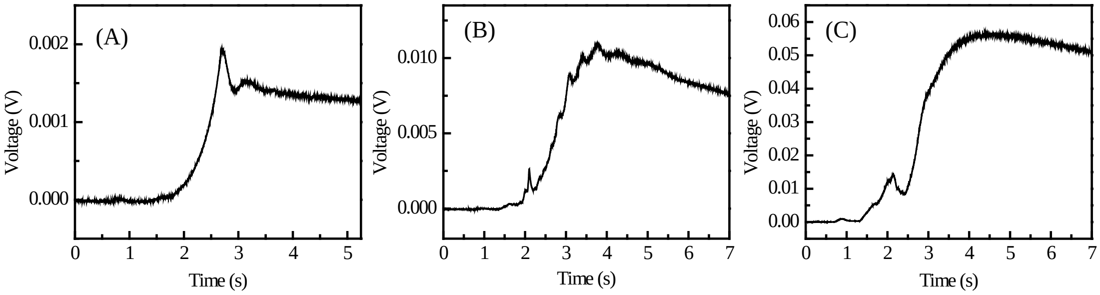

Figure 5-4 FID response to temperature ramping (32°C to 46°C at 50°C/min to 150°C at 50°C/min) through (A) Standard GC guard column, (B) PDMS coated anodically bonded µGC column, and (C) uncoated µGC column bonded using optical adhesives. Helium was used as carrier gas.

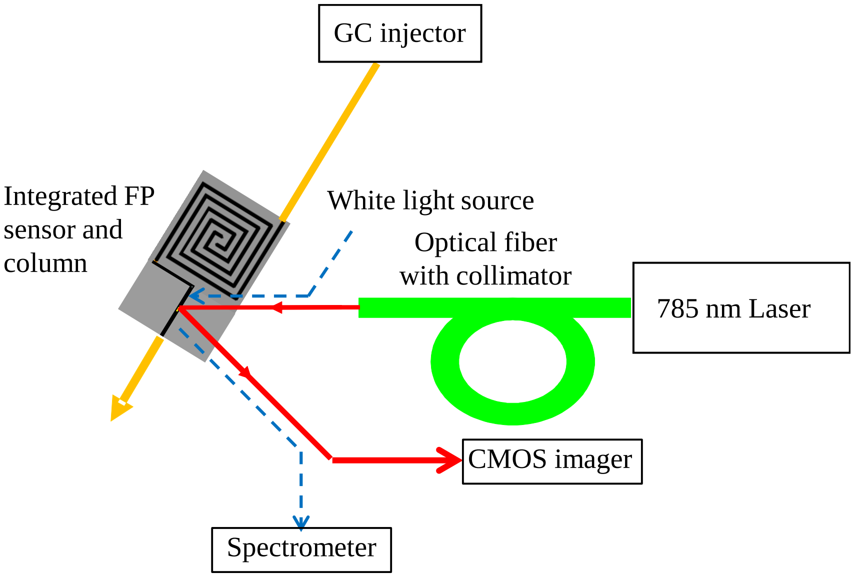

Figure 5-5 Schematic of the fluidic and optical detection setup. A 785-nm laser was used to illuminate the entire FP sensor array. White light co-linear with the laser beam was used to adjust the incident angle to maximize sensitivity. The CMOS imager was used to simultaneously monitor the change in reflected intensity in all three FP sensors caused by the interaction between the vapor analyte with the FP sensors.

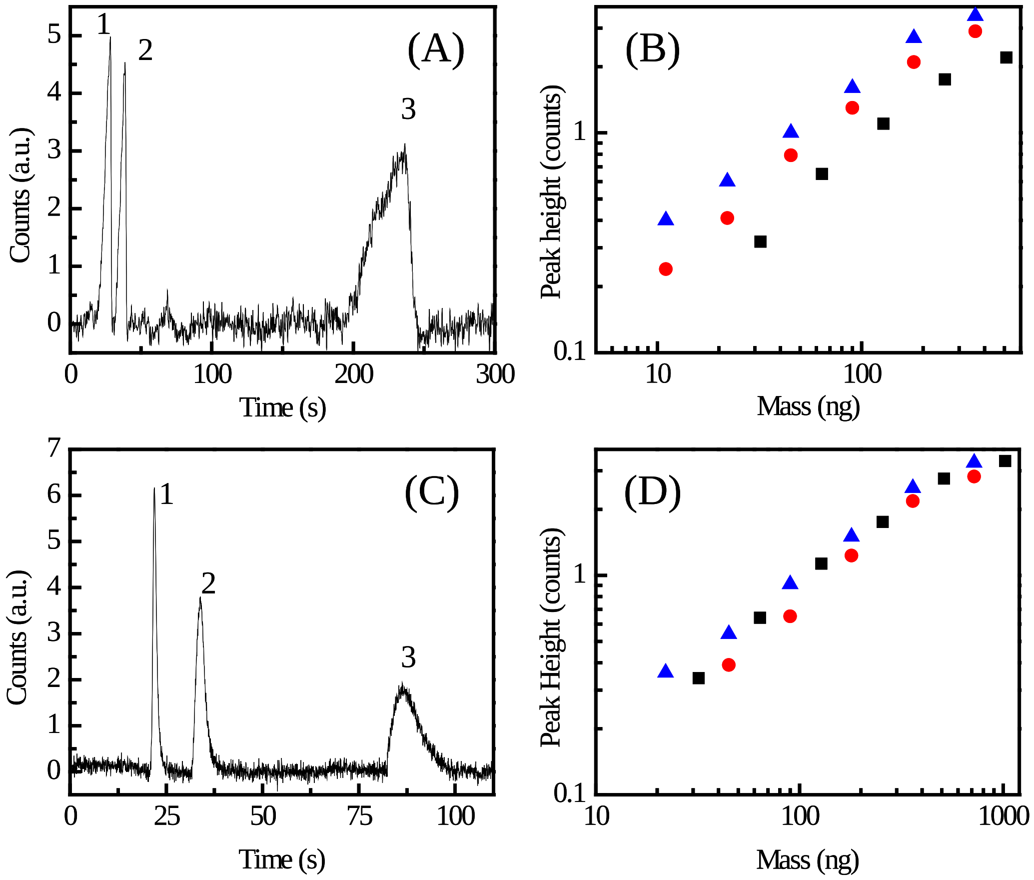

Figure 5-6 (A) Chromatographic response of the OV-1 polymer coating inside a µGC column to a mixture of toluene (1.6 µg, #1), octane (1.4 µg, #2), and decane (2 µg, #3) at 2mL/min. (B) Response of the OV-1 polymer coating inside a µGC column to toluene (squares), octane (circles), and decane (triangles). (C) Chromatographic response of the OV-215 polymer coating inside a µGC column to a mixture of octane (2 µg, #1), toluene (1.6 µg, #2), and decane (1.8 µg, #3) at 2 mL/min. (D) Response of the OV-215 polymer coating inside a µGC column to toluene (squares), octane (circles), and decane (triangles).

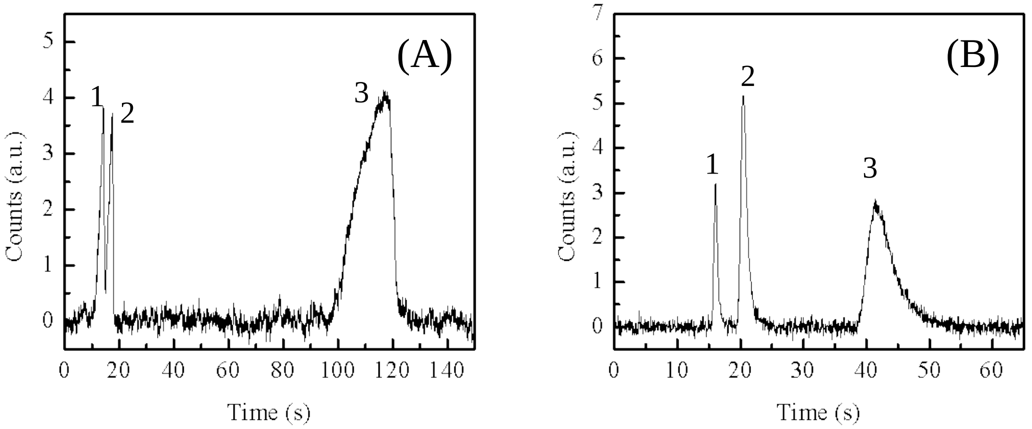

Figure 5-7. (A) Chromatographic response of the OV-1 polymer coating inside a µGC column to a mixture of toluene (0.8 µg, #1), octane (0.72 µg, #2), and decane (2.2 µg, #3) at 3.8 mL/min. (B) Chromatographic response of the OV-215 polymer coating inside a µGC column to a mixture of octane (0.7 µg, #1), toluene (1.3 µg, #2), and decane (1.8 µg, #3) at 3.7 mL/min.

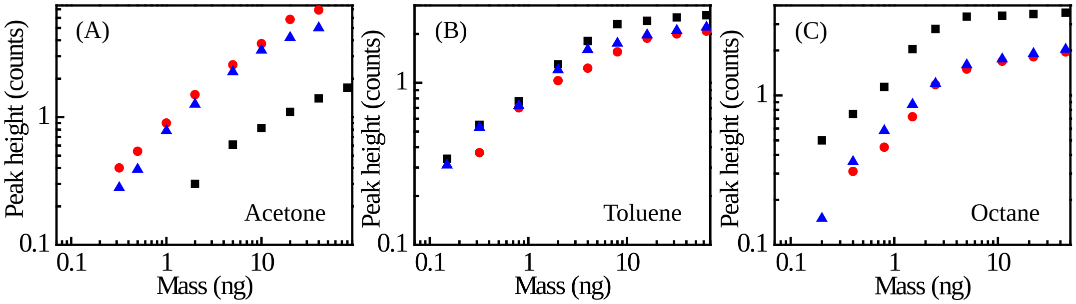

Figure 5-8. Logarithmic response of three different polymers OV-1 (squares), OV-215 (circles), and OV-1701 (triangles) to various injected masses of (A) acetone, (B) toluene, and (C) octane.

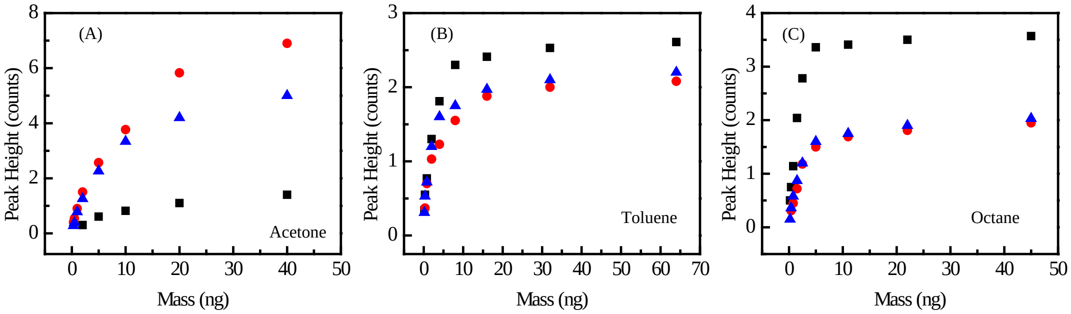

Figure 5-9 Linear Response of three different polymers OV-1 (squares), OV-215 (circles), and OV-1701 (triangles) to various injected masses of (A) acetone, (B) toluene, and (C) octane.

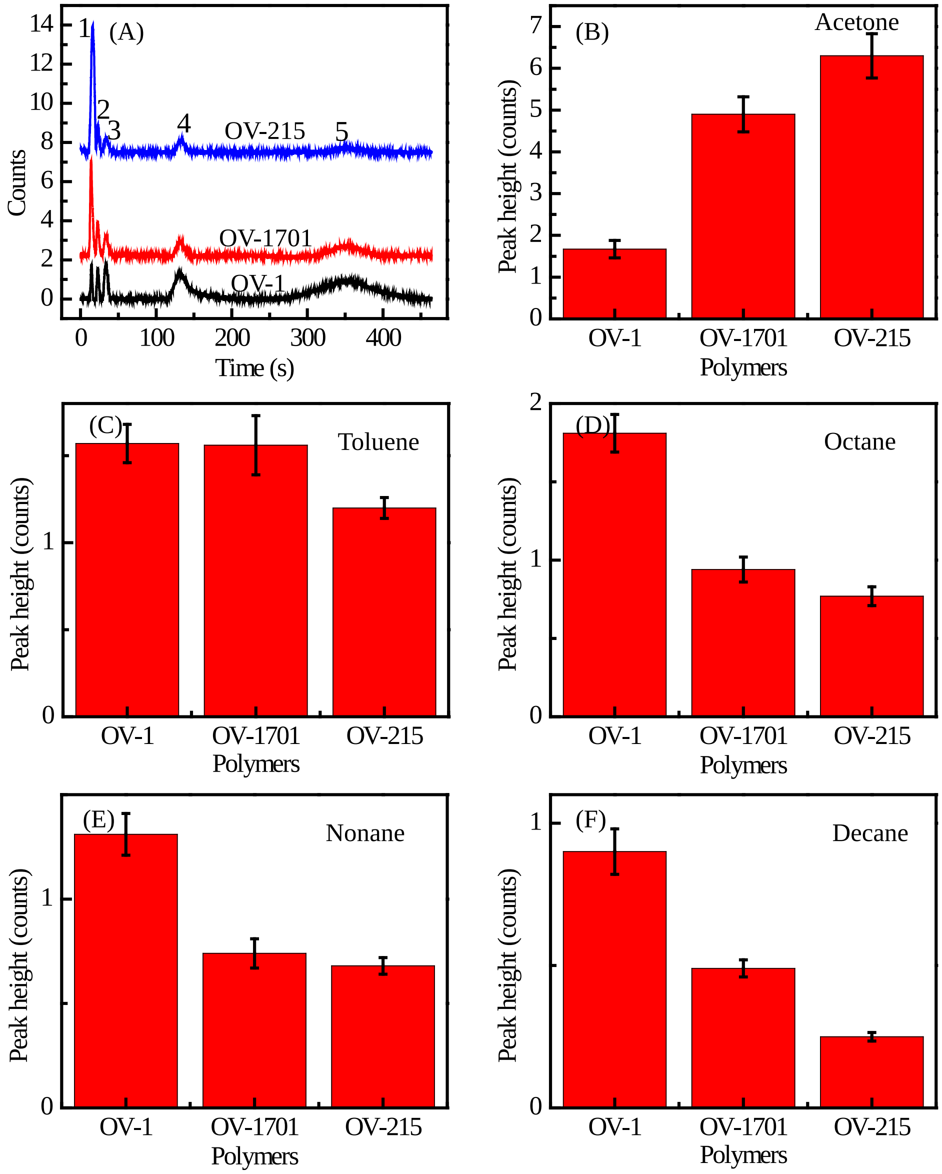

Figure 5-10 (A) Chromatographic response of three polymers on-chip to a mixture of acetone (60 ng, #1), toluene (45 ng, #2), octane (25 ng, #3), nonane (45 ng, #4), and decane (50 ng, #5) at 2 mL/min. (B-F) Response patterns of each analyte with respect to the three polymers on chip for chromatogram shown in (A). Error bars show the standard deviation of 5 runs.

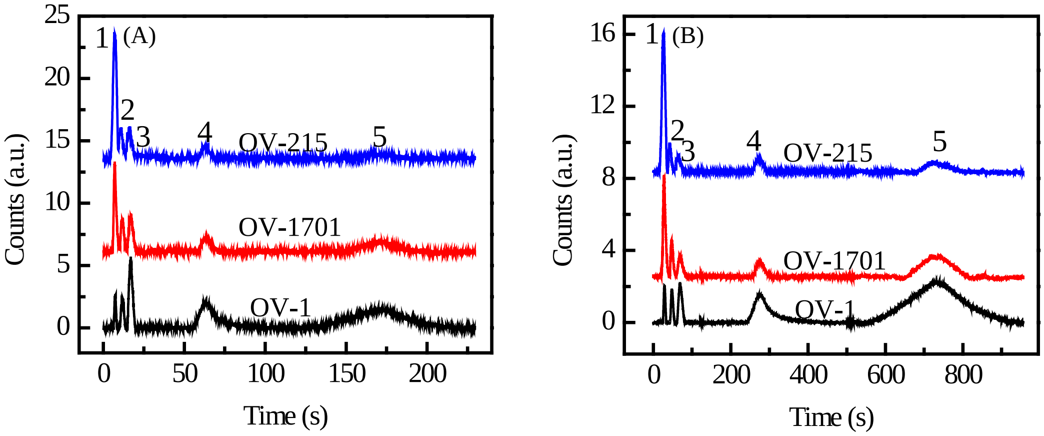

Figure 5-11 (A) Chromatographic response of three polymers on-chip to a mixture of acetone (45 ng, #1), toluene (30 ng, #2), octane (30 ng, #3), nonane (32 ng, #4), and decane (35 ng, #5) at 3.8 mL/min. (B) Chromatographic response of three polymers on-chip to a mixture of acetone (100 ng, #1), toluene (90 ng, #2), octane (55 ng, #3), nonane (110 ng, #4), and decane (220 ng, #5) at 1.1 mL/min.

References

1. F. L. Dorman, J. J. Whiting, J. W. Cochran and J. Gardea-Torresdey, *Anal. Chem.*, 2010, **82**, 4775-4785.
2. E. J. Staples, T. Matsuda and S. Viswanathan, *Environ. Strat. 21st Cent., Asia Pacific Conf.*, 1998.
3. K. Hanseup, W. H. Steinecker, S. Reidy, G. R. Lambertus, A. A. Astle, K. Najafi, E. T. Zellers, L. P. Bernal, P. D. Washabaugh and K. D. Wise, A Micropump-Driven High-Speed MEMS Gas Chromatography System, 2007.
4. R. Manginell, J. Bauer, M. Moorman, L. Sanchez, J. Anderson, J. Whiting, D. Porter, D. Copic and K. Achyuthan, *Sensors*, 2011, **11**, 6517-6532.
5. B. Alfeeli and M. Agah, *IEEE Sens. J.*, 2009, **9**, 1068-1075.
6. J. H. Seo, S. K. Kim, E. T. Zellers and K. Kurabayashi, *Lab Chip*, 2012, **12**, 717-724.
7. T. Sukaew, H. Chang, G. Serrano and E. T. Zellers, *Analyst*, 2011, **136**, 1664-1674.
8. G. Lambertus, A. Elstro, K. Sensenig, J. Potkay, M. Agah, S. Scheuering, K. Wise, F. Dorman and R. Sacks, *Anal. Chem.*, 2004, **76**, 2629-2637.
9. M. Agah, J. A. Potkay, G. Lambertus, R. Sacks and K. D. Wise, *J. Microelectromech. Sys.*, 2005, **14**, 1039-1050.
10. N. Hong-seok, P. J. Hesketh and G. C. Frye-Mason, *J. Microelectromech. Sys.*, 2002, **11**, 718-725.
11. M. A. Zareian-Jahromi, M. Ashraf-Khorassani, L. T. Taylor and M. Agah, *J. Microelectromech. Sys.*, 2009, **18**, 28-37.
12. J. A. Potkay, G. R. Lambertus, R. D. Sacks and K. D. Wise, *J. Microelectromech. Sys.*, 2007, **16**, 1071-1079.
13. J. A. Potkay, J. A. Driscoll, M. Agah, R. D. Sacks and K. D. Wise, A high-performance microfabricated gas chromatography column, 2003.
14. Q.-Y. Cai and E. T. Zellers, *Anal. Chem.*, 2002, **74**, 3533-3539.
15. C. K. Ho and R. C. Hughes, *Sensors*, 2002, **2**, 23-34.
16. E. Covington, F. I. Bohrer, C. Xu, E. T. Zellers and C. Kurdak, *Lab Chip*, 2010, **10**, 3058-3060.
17. M. Fang, K. Vetelino, M. Rothery, J. Hines and G. C. Frye, *Sens. Actuators, B*, 1999, **56**, 155-157.
18. D. Matatagui, J. Martí, M. J. Fernández, J. L. Fontecha, J. Gutiérrez, I. Gràcia, C. Cané and M. C. Horrillo, *Sens. Actuators, B*, 2011, **154**, 199-205.
19. K. Reddy, Y. Guo, J. Liu, W. Lee, M. K. Khaing Oo and X. Fan, *Lab Chip*, 2012, **12**, 901-905.
20. Y. Sun, J. Liu, D. J. Howard, X. Fan, G. Frye-Mason, Shiou-jyh Ja and A. K. Thompson, *Analyst*, 2010, **135**, 165-171.
21. J. C. T. Eijkel, H. Stoeri and A. Manz, *Anal. Chem.*, 2000, **72**, 2547-2552.
22. C. Y. Lee, R. Sharma, A. D. Radadia, R. I. Masel and M. S. Strano, *Angew. Chem. Int. Ed.*, 2008, **47**, 5018-5021.
23. M. Li, E. B. Myers, H. X. Tang, S. J. Aldridge, H. C. McCaig, J. J. Whiting, R. J. Simonson, N. S. Lewis and M. L. Roukes, *Nano Lett.*, 2010, **10**, 3899-3903.
24. E. T. Zellers, M. Morishita and Q.-Y. Cai, *Sens. Actuators B*, 2000, **67**, 244-253.

25. C.-J. Lu, J. Whiting, R. D. Sacks and E. T. Zellers, *Anal. Chem.*, 2003, **75**, 1400-1409.
26. C.-J. Lu, W. H. Steinecker, W.-C. Tian, M. C. Oborny, J. M. Nichols, M. Agah, J. A. Potkay, H. K. L. Chan, J. Driscoll, R. D. Sacks, K. D. Wise, S. W. Pang and E. T. Zellers, *Lab Chip*, 2005, **5**, 1123-1131.
27. J. Liu, M. K. Khaing Oo, K. Reddy, Y. B. Gianchandani, J. C. Schultz, H. M. Appel and X. Fan, *Anal. Chem.*, 2012, **84**, 4214−4220.
28. B. C. Kaanta, H. Chen, G. Lambertus, W. H. Steinecker, O. Zhdaneev and X. Zhang, presented in part at the 22nd IEEE Int. Conf. Micro Electro Mech. Syst., Sorrento, Italy, 2009.
29. B. C. Kaanta, H. Chen and X. Zhang, *J. Micromech. Microeng.*, 2010, **20**, 055016.
30. S. Narayanan, B. Alfeeli and M. Agah, *IEEE Sens. J.*, 2012, **12**, 1893-1900.
31. S. Narayanan and M. Agah, *Hilton Head*, 2012, 221-224.
32. S. I. Shopova, I. M. White, Y. Sun, H. Zhu, X. Fan, G. Frye-Mason, A. Thompson and S-J Ja, *Anal. Chem.*, 2008, **80**, 2232-2238.
33. Y. Sun, J. Liu, G. Frye-Mason, S.-j. Ja, A. K. Thompson and X. Fan, *Analyst*, 2009, **134**, 1386-1391.
34. Y. Sun and X. Fan, *Anal. Bioanal. Chem.*, 2011, **399**, 205-211.
35. J. Liu, Y. Sun and X. Fan, *Opt. Express*, 2009, **17**, 2731-2738.
36. J. Liu, Y. Sun, D. J. Howard, G. Frye-Mason, A. K. Thompson, S.-j. Ja, S.-K. Wang, M. Bai, H. Taub, M. Almasri and X. Fan, *Anal. Chem.*, 2010, **82**, 4370–4375.
37. J. Liu, N. K. Gupta, K. D. Wise, Y. B. Gianchandani and X. Fan, *Lab Chip*, 2011, **11**, 3487-3492.
38. K. Reddy, Y. Guo, J. Liu, W. Lee, M. K. Khaing Oo and X. Fan, *Sens. Actuators B*, 2011, **159**, 60-65.
39. S. Reidy, G. Lambertus, J. Reece and R. Sacks, *Anal. Chem.*, 2006, **78**, 2623-2630.
40. K. Reddy and X. Fan, *Opt. Express*, 2012, **20**, 966–971.
41. C. C. Lee, C. Y. Wang and G. Matijasevic, *IEEE Trans. Compon. Hybr.*, 1993, **16**, 311-316.
42. B. Alfeeli and M. Agah, *IEEE Sens. J.*, 2011, **11**, 2756-2762.
43. J. H. Seo, J. Liu, X. Fan and K. Kurabayashi, *Analytical Chemistry*, 2012, **84**, 6336-6340.
44. G. Serrano, D. Paul, S.-J. Kim, K. Kurabayashi and E. T. Zellers, *Analytical Chemistry*, 2012, **84**, 6973-6980.
45. Note: the polymers used by the FP sensors are routinely used in GC columns as the stationary coating. Therefore, no polymer degradation is expected to arise from temperature ramping.

Chapter VI

Vapor discrimination with a single functionalized nanoparticle film sensor

6.1 Introduction

The optical properties of devices or materials with nanoscale features have been the focus of several studies in the sensing of biological and chemical analytes.[1,2] Absorbance, reflectance, or Raman scattering has been implemented using metallic,[3,4] organometallic,[5-7] and polymeric nanoparticles[8] as well as photonic crystals[9] and lamellar gratings or reflectors.[10] All these schemes have been used as a basis for sensing volatile organic compounds (VOC). The utility of localized surface plasmon resonances (LSPR) in liquid-phase (bio)chemical analyses has been recognized for some time,[2,11,12] but has only recently been applied to the detection of gases[13] and VOCs.[3,5-7,10,14]

Previous studies have shown that for unmodified grating structures[10] or surface-patterned metal nano-islands with either polymer overlay films[3] or thiolate-monolayer functionalization,[14] that LSPR spectral shifts differ among VOCs depending on the

Published: Kee Scholten, Karthik Reddy et al. Analytical Methods 5, 4268-4272, (2013)
Royal Society of Chemistry. Collaborative work with Kee Scholten and Prof. Edward Zellers

differential adsorption of the VOC in the interstitial matrix. Potyrailo *et al*. measured visible reflectance changes due to vapor exposure in unmodified naturally occurring lamellar gratings (i.e., Morpho butterfly wings), and extracted responses at four selected wavelengths to discriminate among high concentrations of methanol, ethanol and water vapor, and among the three isomers of dichloroethylene.[10] Karakouz *et al*. demonstrated polymer-coated gold nano-islands showing differences in the magnitude of LSPR maxima (λ_{max}) shifts with polar and non-polar polymers according to vapor affinity,[3] and Chen *et al*. used thiolate-monolayer functionalized gold nano-islands to detect terpene vapors.[14]

Others have used films of discrete thiolate-monolayer-protected gold nanoparticles (MPN) as plasmonic interface materials,[5-7] complementing the well-documented use of MPNs as vapor-sorptive layers on chemiresistors (CR) and thickness shear mode resonators (TSMR).[15-21] Lu *et al*. used monolayer films of various metal MPNs to detect several VOCs by measuring changes in total absorbance or shifts in λ_{max}.[5] Dalfovo *et al*. demonstrated different changes in shifts of the LSPR λ_{max} of tetraoctylammonium bromide (TOAB) functionalized MPN films upon exposure to toluene and ethanol based on the film swelling/shrinkage and RI changes by the two VOCs.[7]

Based on previous studies it can be inferred that it is possible to discriminate between VOCs using a single MPN coated optical sensor. By using two lasers and a CMOS imager we can avert the need for a spectrometric detector, thereby facilitating a small, portable system suitable for field deployment. Here, we describe such a device and present preliminary results demonstrating such capabilities. First the LSPR of an *n*-

octanethiolate (C8) MPN film was measured, using a spectrophotometer, before, during, and after exposure to vapors of toluene and n-heptane and the spectrums are presented to demonstrate the nature of the spectral changes and reversibility of the vapor-film interaction. Then we present laser reflectance measurements at two discrete wavelengths, flanking the LSPR peak, to illustrate the discrimination of the two VOCs on the basis of the ratios of responses at these wavelengths.

6.2 Materials and methods

6.2.1 Sensor preparation

C8-MPNs were synthesized by Lindsay Amos according to the method of Rowe, *et al.*,[15] with an average Au core diameter of 4.3 ± 0.9 nm. Polydimethylsiloxane (PDMS, Fluka, St. Louis, MO) was used as a reference material. Toluene and *n*-heptane (99%, Sigma Aldrich, St. Louis, MO) were used as received. RI of toluene is 1.496, density 0.867 g/mL, and vapor pressure at rom temperature is 2.91 kPa. Similarly for n-heptane, 1.387, 0.684 g/mL and 4.63kPa and 1-octanethiol has a RI of 1.45.[22]

A glass slide was diced manually to dimensions of 45 × 10 mm to fit inside a 3-mL cuvette, and 8 × 8 mm chips of Si were diced from a 4-inch wafer with a dicing saw. Substrates were cleaned sequentially in acetone and isopropanol, dried, and then exposed to vapors of hexamethyldisilazane (HMDS) to promote adhesion of the C8-MPN or PDMS films. Films were deposited from dilute (5 mg/mL) solutions of C8-MPNs in toluene by spray coating with an airbrush with air at approximately 140 kPa as the propellant. Thickness and uniformity were measured by optical microscopy and laser interferometry (LEXT, Olympus, Tokyo, Japan). PDMS was spin-coated at 7600 rpm onto a Si chip from a 5 mg/mL toluene solution. The thickness was optically measured to be 1-1.2 µm.

6.2.2 Experimental setup and procedure

The MPN-coated glass slide was placed vertically in the plastic cuvette and the absorbance spectrum, from 400 nm to 800nm, was measured with a Beckman COulter DU800 UV-Vis spectrophotometer. Approximately 1.5 µL of liquid VOC was placed in the lid of the cuvette and used to quickly cap the cuvette so that the film was exposed to a high concentration of the vapor. The spectrum was collected and then the lid was removed to and the cuvette left to sit for about 20 min allowing the vapor to dissipate before collecting another spectrum. Separate exposures to toluene and n-heptane were performed in duplicate, which were superimposable.

To embed the sensors inside a microfluidic channel, an open-top channel was first formed by using optical epoxy to glue glass slides together and subsequently bonding it to the sensor (MPN or polymer) substrate. The microfluidic channel was 1mm deep and 800 µm wide (similar to the setup described in previous chapters). A 5-m-long, fused silica guard column (250-µm i.d., Restek, Bellefonte, PA) was used to deliver analytes from the injection port of a benchscale gas chromatograph (3800, Varian, inc., Palo Alto, CA) to the inlet of the microfluidic enclosure and sealed. Helium was used as the carrier gas with a flow rate of 8 mL/min.

The optical setup is shown in Fig. 6-1. The coated Si chip was illuminated in succession by a 785 nm tunable diode laser and a 488 nm diode pumped solid state laser, and the intensity of the reflected beam was measured by a CMOS detector (Thor Labs

DCC1240M, Newton, NJ) with an acquisition time of 1-4 µs and a save rate of 20 frames/s. The wavelengths used flank the measured LSPR peak λ_{max} for the C8-MPN film. A angle of incidence of approximately 30º was found to give the largest responses at both wavelengths, and was fixed for all experiments. Reflected intensity at each wavelength was recorded during separate dynamic exposures to toluene and *n*-heptane by injecting 40, 80, 150 and 200 µL (corresponding to 4.3-22 µg of toluene and 8.6-43 µg of *n*-heptane) of headspace with a gas-tight syringe. The GC injection port oven was set at 250º C and the injector split was set at 0 for MPN sensor testing and 10,000:1 for the PDMS testing, due to the higher sensitivity of polymer sensors. Injected mass was calculated assuming saturation of the headspace at 20 °C. Each test was repeated 4-5 times to ensure accurate results.

6.3 Results and discussion

6.3.1 MPN film characterization

Figure 6-2 (A) illustrates a spray coated C8-MPN sensor substrate. The C8-MPN are distributed as dense, multilayer coated sections surrounded by areas of uncoated substrate. Laser interferometry at five locations on the MPN coated substrate indicated an average film thickness (coated regions) of 260 nm with a standard deviation (SD) of 90 nm. Figure 6-2 (B) shows the absorbance spectrum of a glass substrate coated C8-MPN sensors with an LSPR peak, λ_{max}, at 536.0 nm. The spectrum of C8 MPNs of similar Au-core size in toluene solution was reported to give a λ_{max} of 517 nm.[15] The increased optical coupling between the Au cores, caused by reduced inter-particle distance explains the observed red shift λ_{max} and change in broadness of the absorbance spectrum of the airbrushed film.[23]

6.3.2 Responses to vapors: absorbance spectra

Static exposure of the C8-MPN to high concentrations of toluene and *n*-heptane generated blue shifts of 5.4 nm and 2.6 nm in λ_{max} to 530.6 nm and 533.4 nm respectively. There are two primary causes for shifts in λ_{max}: a change in the inter-particle distance due to film swelling/shrinking and a change in the RI of the medium surrounding the nanoparticles.[22] Swelling of a film will cause a blue shift in λ_{max} and the effect of the change in RI will depend on the RI difference between the inter-particle matrix of the MPN film and the sorbed vapor; if the RI of the sorbed vapor is higher than that of the nanoparticle matrix, then a red shift is expected, and if it is lower, then a blue shift is expected. The blue shift in λ_{max} for *n*-heptane is consistent with its RI being lower than that of the C8 monolayer and its ability to swell the film. The blue shift in λ_{max} for toluene, whose RI is higher than that of C8, indicates that a large swelling behavior dominates the optical response. A similar result (and explanation) was reported by Dalfovo *et al*. for 4.4-nm TOAB-MPN films exposed to saturated toluene vapor,[7] in spite of the RI for TOAB (i.e., n = 1.42) being lower than that of toluene. Due to the higher partition coefficient and swelling efficiency of toluene compared to *n*-heptane it is expected to demonstrate a larger shift in λ_{max}.[20] By and large λ_{max} returned to its pre-exposure value and the entire absorbance spectrum returned to it's original levels after venting of the cuvette, however upon extended exposure to saturated concentrations of toluene a loss of the LSPR absorbance was observed, which was recovered only after re-casting the nanoparticle film from toluene solution, see Fig. 6-3.

Apart from shifts in λ_{max}, spectral measurements also indicated absorbance changes within specific spectral regions that illustrated differences in response between the two VOCs: for all $\lambda > \lambda_{max}$ exposure to either VOC reduced the magnitude of the absorbance, while for all $\lambda < \lambda_{max}$ toluene increased the absorbance and *n*-heptane decreased the absorbance. The inset of Figure 6-2 (B) shows the absorbance at λ_{max} increased during toluene exposure and decreased during *n*–heptane exposure. This analyte-dependent difference in sorption-induced changes in spectral features alludes to the possibility that selective sensing would be possible by probing the MPN film at multiple discrete wavelengths.

6.3.3 Responses to vapors: reflectance measurements

A C8-MPN film was coated on a clean Si substrate, enclosed in a glass microfluidic cell, and tested with the two analytes, toluene and heptane, separately at various injected masses of vapor head space, while being interrogated consecutively with 785 and 488 nm lasers. In all cases, both wavelengths and both analytes, the reflected intensity showed a decrease with increasing injected analyte mass. Calibration curves for both vapors are shown in Figures 6-4 (A) and (B), displaying excellent linear fits ($r^2 > 0.97$, standard errors of the slopes < 6%). Changes in reflected intensity can be attributed to a combination of absorbance, reflectance, and scattering. Calculated sensitivities (peak area per µg of injected vapor) at 785 nm are 9.5×10^{-3} and 3.2×10^{-3} for toluene and *n*-heptane, respectively, and at 488 nm are 14×10^{-3} and 4.0×10^{-3}, respectively. The adsorption and desorption of the analytes can be seen in the inset of Fig. 6-4 (A) documenting excellent reversibility and repeatability of the responses.

The relative magnitudes of the sensitivities can be assessed in light of a previous study by Steinecker *et al*. of vapor uptake by films of C8-MPNs with ~4.3-nm Au-core diameters on CR and TSMR sensors.[24] From this study we calculate a net swelling ratio of 3.4 (i.e., $K_{tol}/K_{hep} \times \Psi_{tol}/ \Psi_{hep}$).

By keeping the condition for the dynamic exposures tests the same across all tests for both VOCs, thereby producing similar peak widths, it can be inferred that the vapor concentrations should be similar for a given injected mass. The toluene:*n*-heptane sensitivity ratios are 2.97 and 3.60 at 785 nm and 488 nm, respectively, which are remarkably close to the swelling ratio of 3.4. This suggests that the primary cause for the relative responses are the relative volumetric changes of the film. The larger sensitivity ratio at 488 nm and the smaller sensitivity ratio at 785 nm, compared to the calculated swelling ratio of 3.4 is qualitatively consistent with the differences in absorbance between toluene and *n*-heptane noted above for the spectral regions flanking λ_{max}. Such wavelength-dependent differences reflect the (secondary) contributions of the RI changes to the optical responses.

The reflectance measurements show the toluene sensitivity was higher at 488 nm than at 785 nm, which is consistent with the data acquired by the spectrophotometer that showed an increase in absorbance at $\lambda < \lambda_{max}$. However, the reflectance measurements showed decreases in reflected intensity at 785 nm for toluene and at both wavelengths for *n*-heptane, while the spectrophotometric measurements showed decreases in absorbance for these exposures. This discordance can be ascribed to differences in these two optical configurations; specifically to an increase in the extent of scattered and reflected light from the air-film and substrate-film interfaces in the reflectance measurements.[25,26]

Limits of detection (LOD) were calculated as 1σ/(sensitivity) where σ was the standard deviation of the baseline signal and the sensitivity was re-calculated using peak height instead of area. LODs at 785 nm are 0.07 and 0.16 μg for toluene and heptane, respectively, and at 488 nm are 0.36 and 1.1 μg, respectively. The LODs are higher at 488 nm than 785 nm despite higher sensitivites at the lower wavelength due to a higher baseline noise generated by the 488 nm laser. The baseline noise at 785 nm was eight times lower than at 488 nm.

To properly characterize these results reflectance measurements were also collected with a reference Si substrate coated with PDMS. Since PDMS has no absorbance in the visible range, changes in reflected light intensity arise only from changes in the film thickness and changes in the RI of the bulk. This phenomenon is exploited in vapor sensors that are based on Fabry-Perot (FP) interferometry.[27] Responses were proportional to injected vapor mass and calibration curves were linear ($r^2 > 0.97$, standard slope error < 5%). The PDMS exposures were performed with split injections (10,000:1) from the GC and the PDMS film was ~4-5 times thicker than the MPN film, a direct comparison of sensitivities and LODs is not possible. The PDMS film is more sensitive at 488 nm than at 785 nm due to the steeper slope in the FP spectrum at lower wavelengths. The steep slope allows for a larger shift in single wavelength intensity measurements even if the change in the position of the spectral peaks or dips is the same.

The bar charts in Fig. 6-4 (C) present the ratios of the sensitivities at the two wavelengths for toluene and *n*-heptane for both films, normalized to the sensitivities at

488 nm. For the C8-MPN film the average (± SD) ratios were 0.68 ± 0.035 and 0.80 ± 0.053 for toluene and *n*-heptane, while for the PDMS reference film the ratios were 0.082 ± 0.005 and 0.088 ± 0.006. The difference between the MPN ratios is significant, whereas the difference between the PDMS ratios is not, confirming that vapor discrimination is a function of the optical properties of the MPN film.

6.4 Conclusion

Here we demonstrated the use of dual-wavelength reflectance measurements to effectively discriminate between two non-polar analytes, toluene and heptane, based on differences in reflected light intensity at specific wavelengths. A simple two laser, CMOS imager, and a single substrate coated with C8-MPNs made up the experimental setup, unlike previous reports where complex spectrometric setups were used. Our system can be easily miniaturized for use in portable sensing systems for VOC monitoring.

Spectrophotometric measurements indicated reversible blue shifts in the LSPR λ_{max} for high-concentration exposures to both toluene and *n*-heptane, despite their RI values flanking that of the C8 monolayers in the MPNs tested here. Coupled with estimates of swelling ratios derived from independent data, these results suggest that the primary effect of the exposure to analytes is the increase in average inter-particle distance of the MPNs accompanying sorption-induced film swelling, with changes in the local RI having a secondary effect.

The use of multiple, discrete, optical probes of individual plasmonic sensing films shown here is an example of what might be termed multi-variable (MV) sensing. Other examples have been reported by Potyrailo, *et al.*[10,28] An array of such MV sensors in which multiple films of MPNs with different core sizes, shapes, and/or monolayer structures are probed at two or more wavelengths shows promise for increasing the diversity of responses one can obtain from a VOC sensor array. This, in turn, should lead to improvements in performance over current single-transducer (ST) and multi-transducer (MT) arrays, which provide only a single response from each sensor in the array and, consequently, have only limited capabilities for VOC-mixture analysis.[29,30]

Although the sensitivity achieved with the C8-MPN sensing film here was quite low, enhanced sensitivity should be possible by use of high-quality-factor optical resonators, to increase the effective path length of the optical sensor.[31] Current work in our laboratory on the development of microfabricated optofluidic ring resonators (μOFRR) as platforms for multi-wavelength sensing with MPN interface films has shown some promising results in preliminary testing.[32,33]

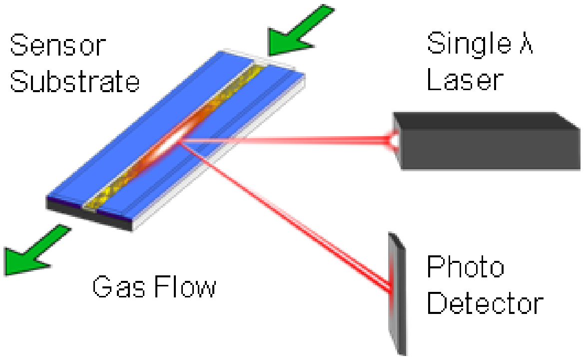

Figure 6-1 Illustration of the apparatus used for laser reflectance measurements of C8-MPN and PDMS films during calibrations with toluene and *n*-heptane. Discrete injections of different quantities of each vapor were made via a heated GC injection port and were routed through the microfluidic cell via de-activated capillary at 8 mL/min (carrier gas was He).

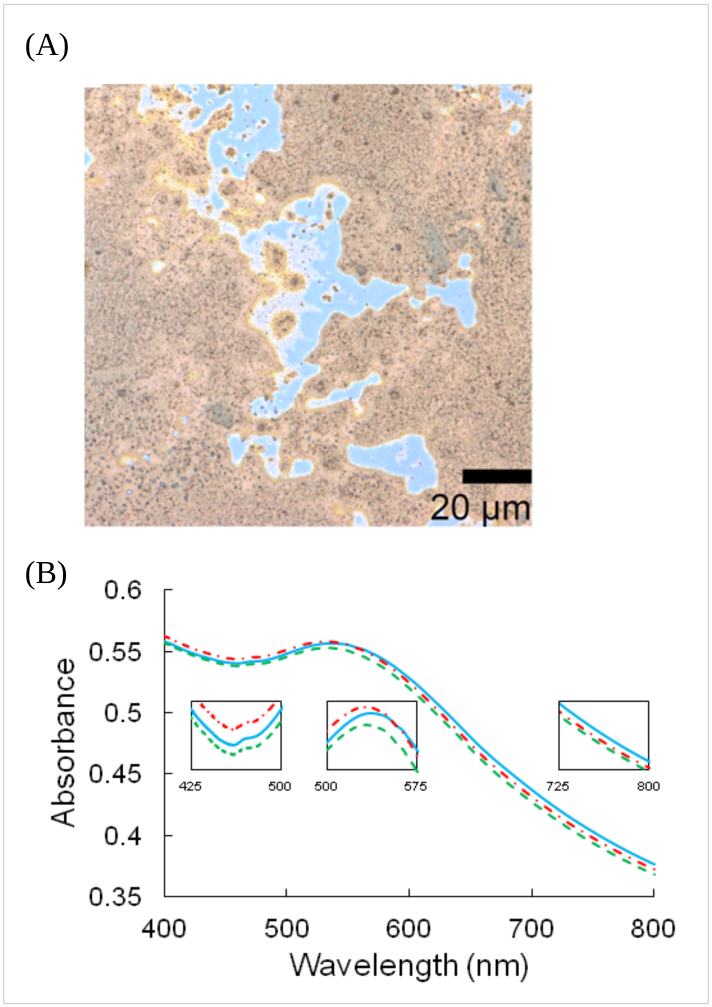

Figure 6-2 (A) Optical micrograph (1000×) of a C8-MPN film on a Si substrate; (B) visible absorbance spectrum of a C8-MPN coated glass slide prior to exposure (solid blue line), during static exposure to *n*-heptane (dashed green line), and during static exposure to toluene (dashed-dotted red line). Insets show enlargements of selected spectral regions. Absorbance was measured with reference to a blank glass slide.

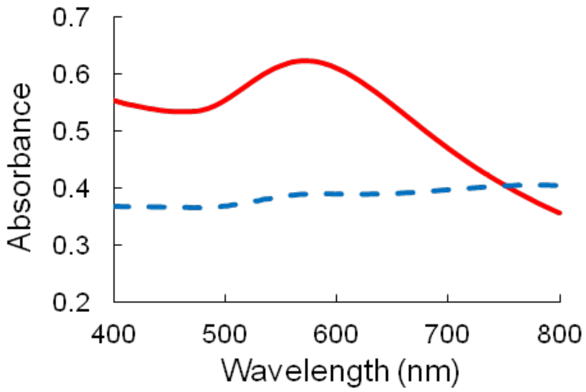

Figure 6-3 Visible absorbance spectrum of a C8-MPN coated glass slide before (solid line) and after (dashed line) several minutes of static exposure to vapors generated by injecting 5 µL of liquid toluene into the cuvette and sealing the lid.

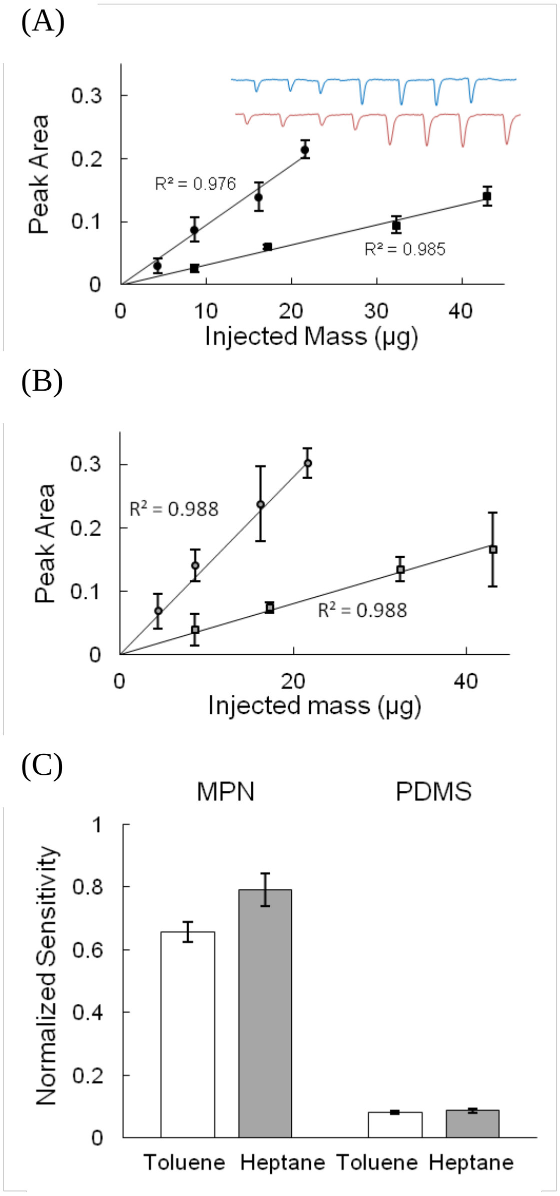

Figure 6-4 (A) 785 nm and (B) 488 nm laser reflectance calibration curves for vapors of toluene (circles) and *n*-heptane (squares) from a single C8-MPN coated Si device. Peak area is plotted versus the injected mass of vapor. Error bars designate ± 1 standard deviation (n = 4 or 5 injections) and are attributed to imprecision in injected masses rather than inherent variability in responses. R^2 values are from linear regression with a forced-zero intercept. Inset in a) shows a representative series of response profiles (peaks) for *n*-heptane (upper trace) and toluene (lower trace) at 785 nm. Bar charts in (C) show sensitivities to each vapor at 785 nm for the C8-MPN and PDMS coated devices (as indicated) normalized to the sensitivity at 488 nm. Error bars indicate ± one standard error of the slope.

References

1. A. Shipway, E. Katz and I. Willner, *Chem. Phys. Chem.*, 2000, **1**, 18-52.
2. M. Stewart, C. Anderton, L. Thompson, J. Maria, S. Gray, J. Rogers and R. Nuzzo, *Chem. Rev.*, 2008, **108**, 494-521.
3. T. Karakouz, A. Vaskevich, and I. Rubenstein, *J. Phys. Chem.*, 2008, **112**, 14530-14538.
4. M. K. Oo, C.F. Chang, Y. Sun and X. Fan, *Analyst*, 2011 **136**, 2811-2817.
5. C-S. Cheng, Y-Q. Chen, and C-J. Lu, *Talanta*, 2007, **73**, 358-365.
6. K-J. Chen, and C-J. Lu, *Talanta*, 2010, **81**, 1670-1675.
7. M. Dalfovo, R. Salvarezza, and F. Ibanez, *Anal. Chem.* 2012, **84**, 4866-4892.
8. T. Endo, Y. Yanagida and T. Hatsuzawa, *Sens. Actuat. B Chem.*, 2007, **12**, 589-595.
9. T. L. Kelly, A. G. Sega and M. J. Sailor, *Nano Lett.*, 2011, **11**, 3169-3173.
10. R. Potyrailo, H. Ghiradella, A. Vertiatchikh, K. Dovidenko, J. Cournoyer and E. Olson, *Nat. Photon.*, 2007, **1**, 123-128.
11. N. Nath, and A. Chilkoti, *Anal. Chem.*, 2002, **74**, 504-509.
12. A. Kabashin, P. Evans, S. Pastkovsky, W. Hendren, G.A. Wurtz, R. Atkinson, R. Pollard, V.A. Podolskiy and A.V. Zayats, *Nat. Mater.*, 2009, **8**, 867-871.
13. M. Nandasiri, P.H. Rogers, W. Jiang, T. Varga, S.V.N.T. Kuchibhatla, S. Thevuthasan and M.A. Carpenter, *Anal. Chem.*, 2012, **84**, 5025-5034.
14. B. Chen, C. Liu, M. Ota and K. Hayashi, *IEEE. Sens. J.*, 2013, **13**, 1307-1314.
15. M. Rowe, K. Plass, K. Kim, Ç. Kurdak, E.T. Zellers and A. Matzger, *Chem. Mater.*, 2004, **18**, 3513-3517.
16. F.I. Bohrer, E. Covington, Ç. Kurdak and E.T. Zellers, *Anal. Chem.*, 2011, **83**, 3687-3695.
17. C-L. Li, Y-F. Chen, M-H. Liu and C-J. Lu, *Sens. Actuat. B Chem.*, 2012, **169** 349-359.
18. J. Grate, D. Nelson and R. Skaggs, *Anal. Chem.*, 2003,**75**, 1868-1879.
19. N. Krasteva, I. Besnard, B. Guse, R. Bauer, K. Mullen, A. Yasuda and T. Vossmeyer, *Nano Lett.*, 2002, **2**, 551-555.
20. L. Wang, X. Shi, N. Kariuki, Schadt, M. G. Wang, Q. Rendeng, J. Choi, J. Luo, S. Lu and C-J. Zhong, *J. Am. Chem. Soc.*, 2007, **129**, 2161-2170.
21. S. Kim, H. Chang and E.T. Zellers, *Anal. Chem.*, 2011, **83**, 7198-7206.
22. CRC Handbook of Chemistry and Physics, 93rd Ed., Internet Version 2013 http://www.hbcpnetbase.com/
23. A. Templeton, J. Piertron, R. Murray and P. Mulvaney, *J. Phys. Chem. B,* 2000, **104**, 564-570.
24. W. Steinecker, M. Rowe and E.T. Zellers, *Anal. Chem.*, 2007, **79**, 4977-4986.
25. G. Gauglitz, A. Brecht, G. Kraus and W. Nahm, *Sens. Actuat. B Chem.*, 1993, **11**, 21-27.
26. G.G. Daaboul, R.S. Vedula, S. An, C.A. Lopez, A. Reddington, E. Ozkumur and M.S. Ünlü, *Biosens. Bioelectron.*, 2011, **26**, 2221-2227.
27. K. Reddy, Y. Guo, J. Liu, W. Lee, M. Oo and X. Fan, *Sens. Actuat. B Chem.*, 2011, **159**, 60-65.
28. R. Potyrailo and W. Morris, *Anal. Chem.*, 2007, **79**, 45-51.
29. C. Jin and E.T. Zellers, *Anal. Chem.*, 2008, **80**, 227-236.

30. C. Jin and E.T. Zellers, *Anal. Chem.*, 2008, **80**, 7283-7293.
31. F. Vollmer and S. Arnold, *Nat. Methods*, 2008, **5**, 591-596.
32. K. Scholten, X. Fan, and E.T. Zellers, *App. Phys. Lett*., 2008, **99**, 141108-3.
33. K. Scholten, X. Fan and E.T. Zellers, *Tech. Digest Transducers'13,* Barcelona, Spain, June 16-20, 2013.

Chapter VII

Rapid high-frequency graphene nanoelectronic vapor sensors for micro-gas chromatography

7.1 Introduction

Nanoelectronic devices based on nanomaterials such as nanowires, carbon nanotubes, and graphene offer an extremely large surface-to-volume ratio, a high carrier mobility, low power consumption, and high compatibility and integration with the modern electronic technologies.[1-3] These distinct advantages are being explored for a variety of applications, including vapor sensing. Currently, the most common sensing mechanism relies on the detection of charges. Charge transfer between the absorbed molecules and the nanomaterial changes the surface charge density, thus modulating the Fermi energy and conductivity of nanomaterials. To date, nanowires, carbon nanotubes, and graphene have been demonstrated as direct current (DC) nanoelectronic vapor sensors, showing a sensitivity down to the ppb level.[4-18]

However, one of the largest challenges for those nanoelectronic vapor sensors is their extremely slow sensing response and recovery, typically on the order of hundreds of

Collaborative work with Girish Kulkarni and Prof. Zhaohui Zhong seconds.[6,19] Although various chemoselective surface coatings have been used to improve the response time, they function for only narrowly selected vapor molecules.[6,8,20] Such drawbacks significantly hinder the employment of nanoelectronic sensors in the applications requiring rapid sensing response to a broad range of vapor analytes, such as micro-gas chromatography (μGC) where sub-second time resolution is desirable. Unfortunately, this slow response arises intrinsically from the slow dynamics of interface trapped charges in the nanoelectronic sensors, and therefore, it is difficult, if not impossible, to overcome within the current framework of the sensing mechanism.

Here we describe a radically different sensing mechanism based on detection of vapor molecules' dipole moments rather than charges. In contrast to the existing nanoelectronic sensing technologies where the DC signal is used, our approach utilizes the graphene transistor as a high-frequency (>100 kHz) mixer with surface-adsorbed molecules functioning as an electrostatic gate. By going into higher frequencies, the slow sensing response hindering the conventional nanoelectronic sensor can be overcome when the AC field switching outpaces the slow dynamics of interface states. In this work, we first analyzed the high-frequency graphene vapor sensor using the theory shown in Appendix V. Then we connected it with a GC system, showing rapid (down to ~0.1 s) and sensitive (down to ~10 ppb) detection of a wide range of analytes separated by a GC column, which represents orders of magnitude improvement in both response time and sensitivity over the state-of-the-art.

7.2 Theory

The sensing signal of a nanoelectronic sensor can generally be described as:

$$I(V+\delta V)=I(V)+G\big|_V\cdot\delta V+\frac{1}{2}\cdot\frac{\partial G}{\partial V}\bigg|_V\cdot(\delta V)^2+.......,\qquad(7.1)$$

where V is a constant bias voltage, G is the sensor conductance and δV is a modulating signal, if applied. The DC sensors are accounted for by the first term in Eq. (7.1). Vapor molecules are charge neutral and DC detection relies on the sensor's ability to donate/accept electrons, a slow process working only at defect sites, which may lead to irreversible binding of vapor molecules that requires prolonged heating, current stimulation, or ultraviolet radiation for sensor regeneration.[19,21] A time-variant signal δV forms the basis of alternating current (AC) detection and is represented by the first order term in Eq. (7.1). However, AC detection also relies on the charge-transfer mechanism, and therefore, suffers from the same aforementioned slow response and irreversibility issues. Moreover, it too requires a polymer coating to achieve high sensitivity and a large device footprint for accurate capacitance measurements.

In contrast, our high-frequency graphene transistor sensor exploits the non-linearity associated with the second order term of Eq. (7.1). An AC voltage passing through the graphene will induce a potential change, $\Delta\phi$, from the dipole moment of surface-bound molecules that oscillate at the same frequency as the drive. $\Delta\phi$ in turn behaves like a "local gate" to modulate the output current. The change in mixing current (*i.e.*, the sensing signal in this work) can be written as:

$$\Delta I_{mix}=-\frac{1}{2}\frac{\partial G}{\partial V_g}\Delta\phi|\delta V|.\qquad(7.2)$$

By applying a high-frequency AC field that outpaces the slow dynamics of interface states, the sensing response time can tremendously be improved. In addition, the dielectric response of molecule is amplified *in situ* by the intrinsic gain of the transistors.

Also note that sensing signal (ΔI_{mix}) is linearly proportional to the molecule induced potential, $\Delta\phi$, and hence the concentration of the vapor molecules near the sensor.

7.3 Methods

Figure 7-1(A) shows the experimental setup. Analytes were injected using a liquid syringe at the GC injection port, and delivered to the graphene sensor module (Fig. 7-1(B)) and a flame ionization detector (FID). The graphene sensor was first fabricated by the chemical vapor deposition method[22-24] and then transferred onto thermal oxide on silicon wafer before 0.5 nm Ti/100 nm Au source/drain terminals were lithographically patterned. The graphene sensor was implemented using a simple three-terminal field-effect-transistor (FET) geometry (Fig. 7-1(C)). An amplitude modulated (AM) voltage drive (f_c = 100 kHz) was applied to the source terminal through a bias-tee, while the dc bias at source and gate terminals were kept at ground (V_{sd}, V_g = 0 V). The mixing-current was detected at modulated frequency using a lock-in amplifier. Fig. 7-1 (D) shows mixing-current response of a typical graphene-FET (GrFET) sensor to 9 different analytes.

A 1.5 m GC guard column similar to what was used in previous chapters delivered the analyte to the sensor with helium used as a carrier gas at 8 mL/min.

7.4 Results and discussion

The temporal response of the GrFET sensor to pulsed injections of varying masses of common volatile organic compounds was investigated in Fig. 7-2 (A). In order to minimize the peak broadening caused by the GC column, a GC guard column, which has a minimal broadening effect, was used to deliver analytes to the graphene sensor and FID, separately. Fast sensor response with a sub-second full-width-half-maximum (FWHM, $t_{1/2}$) was observed for dichloromethane ($t_{1/2}$ = 0.61 s), ethanol ($t_{1/2}$ = 0.92 s), chloroform ($t_{1/2}$ = 0.69 s), 2-propanol ($t_{1/2}$ = 0.98 s) and acetone ($t_{1/2}$ = 0.75 s), which were similar to or faster than FID response times. Even for relatively high boiling point vapors - chlorobenzene, dioxane, and DMF, whose boiling point is over 100 ^{o}C (see Table 7-1), the GrFET sensor still showed impressive responses time of 0.9 s, 1.65 s and 1.8 s respectively, which was comparable to the FID response. Although dioxane and DMF show slow desorption from the graphene surface, total response time (90% recovery time, $t_{90\%}$) still compares well with the FID responses.

Vapors of a higher boiling point analyte tend to condense more on a surface and thus have longer desorption time. They can be used as a model system to ultimately test the sensor response time and sensitivity. Fig. 7-2 (B) presents the temporal response of the GrFET sensor of 205 pg injection of DMMP (boiling point = 181 ^{o}C) along with the corresponding FID response time. We observed comparable response time for GrFET sensor ($t_{1/2}$ = 6.1 s) and FID ($t_{1/2}$ = 5.5 s). However, DMMP desorption time for graphene sensor ($t_{90\%}$ = 28 s) was approximately two times that of FID ($t_{90\%}$ = 13.2 s), indicative of the slow desorption process of DMMP molecules from the graphene surface.

To investigate the GrFET sensor sensitivity, in Fig. 7-2 (C) we plot the sensor response, ΔI_{mix}, in response to repeated doses of DMMP varying from 205 pg to 23.2 ng, showing that sensing signal increased with increasing injected mass of DMMP, and that the response was instantaneous and also completely reversible for all the masses under test. Experimentally, the lowest injected mass was 205 pg, corresponding to a concentration of approximately 40 ppb (see Appendix III about the concentration calculation). To further estimate the GrFET sensor detection limit, we plot sensor dosage response more clearly in the log-log scale in Fig. 7-2 (D), which shows a slope of 0.4. Using a 1σ noise floor (1σ = 0.04 nA), the detection limit of our GrFET for DMMP is approximately 1 pg in mass or 0.22 ppb in concentration (Appendix III), which to our knowledge is the lowest for any uncoated, pristine nanoelectronic vapor sensor.

To demonstrate the capability of detecting a wide range of vapor analytes, Fig. 7-2 (E) plots the GrFET sensor dosage response for an additional 9 analytes on the log-log scale. All analytes are linear on the log-log scale at low concentrations and saturate at higher concentrations. The parameters and the experimental results (such response time and lowest injected mass, *etc.*) of all 13 analytes used in our work are summarized in Table 7-1. The superior performance of the high-frequency AC detection is obvious when we contrast the results in Fig. 7-2 (C) and 2 (F) with those in Fig. 7-3, where, using the DC detection method, the GrFET sensor was much less responsive in both response time and sensitivity.

The GrFET sensor exhibits strong bi-polar behavior, as exemplified in Fig. 7-4, where the sensor response can be categorized into 3 types – zero (Left panel), positive (Middle panel), and negative (Right panel). This characteristic can be understood by considering Eq. (7.2), where $\Delta\phi \propto \left|\vec{p}\cdot\vec{r}\right|$ accounts for the induced dipole fluctuations. $\vec{p}$ is the dipole moment vector and $\vec{r}$ is the distance between the dipole and graphene. Consequently ΔI_{mix} depends on both the dipole moment and the orientation of the vapor molecule on top of graphene. For molecules with zero dipole moment (Left panel), the term ΔI_{mix} is zero. For molecules that are oriented with the electronegative/electropositive

(Middle/Right panel) center closer to the graphene surface, the induced potential fluctuation, $\Delta\phi$, leads to a positive (negative) sign for ΔI_{mix}. The bi-polar response of the GrFET sensor adds a degree of selectivity to the benefit of vapor identification.

The above mixing current model can also be used to estimate the intrinsic sensitivity and hence the detection limit of the GrFET sensor. The mixing current term can be simplified to

$$\Delta I_{mix} = \frac{\mu\varepsilon}{2Lt_{ox}h} \cdot p\tilde{v}_{sd} \qquad (7.3)$$

(see Appendix V) and using L = 7 μm, h = 5 nm, μ = 1000 cm^2/V.s, t_{ox} = 200 nm, v_{sd} = 20 mV, we obtain ΔI_{mix} equal to 1 pA (5 pA, if we assume h=1 nm) for a molecule of dipole moment of p = 1 Debye. For the noise of σ = 0.04 nA, this corresponds to a detection of 7-10 molecules on the graphene surface. These initial results demonstrate that our GrFET sensors are not only promising candidates for integration with µGC systems; but with optimized channel geometry, better device transconductance and selective polymer gain coatings our GrFET sensors also show potential for single molecule detection.

Rapid separation and detection of chemical vapors is of critical importance for on-site vapor monitoring with portable µGC systems. In Fig. 7-5 we present the response of GrFET sensor (lower panel) and FID (upper panel) to a mixture of eight analytes. Analytes were separated and delivered using a combination of 7.2 m long CP-SIL-5-CB column, 2.8 m long Carbowax column, and 70 cm long guard column. Temperature and flow programming were used to achieve rapid separation, while maintaining sharp peaks. The oven temperature was initially set to 32 ^{o}C, after 36 seconds it was ramped up to 45 ^{o}C at a rate of 50 ^{o}C/min. The temperature was held at 45^{o}C for 24 seconds before being ramped up to 80^{o}C at 100 ^{o}C/min. After 12 seconds the temperature is increased to 110 ^{o}C at 50 ^{o}C/min and held there for the rest of the run. The flow pressure is initially set to 15 psi and ramped at a rate of 30 psi/min to 19 psi, after 30 seconds. A Y-split, placed after the CP-SIL-5-CB and Carbowax columns is used to split the analytes in a near 50-50 ratio and deliver them to the GrFET and FID simultaneously using two 70 cm long guard columns see Fig. 1 (A). Injector oven and FID oven were set at 250 ^{o}C and 300 ^{o}C respectively. We observed that the graphene sensor not only responds instantaneously to all polar molecules in the same temporal window as the FID, but also switches sign rapidly for electronegative and electropositive species (relative to graphene), delivered one after the other (Fig.7-5, 6 – dioxane and 7 – toluene). Pentane and benzene, being non-polar were not detected by the GrFET sensor. We have observed both positive and negative ΔI_{mix} response to 2-propanol (Fig. 7-2 (A) and Fig. 7-4), however all devices processed (including thermal oxide growth) in one batch show consistent behavior. We feel this could a substrate effect where end terminations may preferentially orient the alcohol molecules through hydrogen bonding, however further investigation is needed.[13]

7.5 Conclusion

We have fabricated and characterized a high frequency Gr-FET chemical sensor. The sensor is highly reproducible, has excellent sensitivity, with detection limits under 10 pg and response-desorption times orders of magnitude better than comparable pristine graphene DC sensors. The sensors show great promise for integration with µGC components. The nature of the detection scheme also gives a basis of analyte identification and the sensors were shown to be able to rapidly detect eluted analytes from a separation column. Future work will focus on fabrication procedures, instrumentation and a further understanding of the detection dynamics.

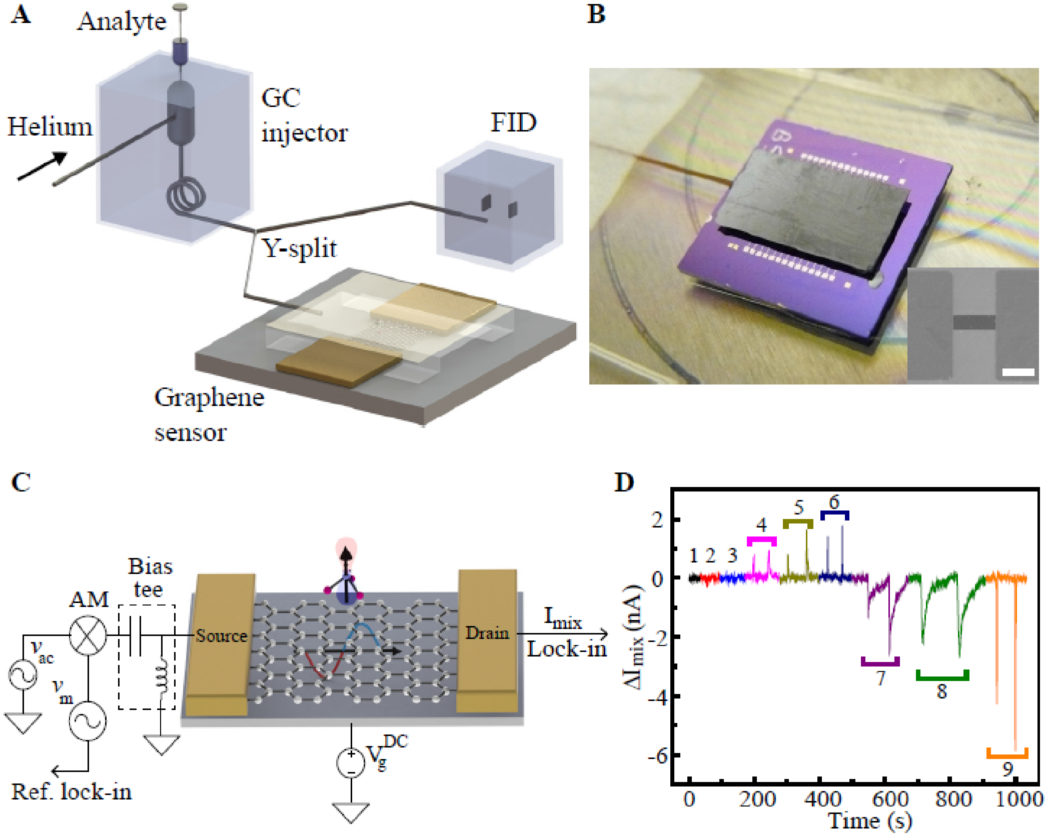

Figure 7-1 Experimental setup, optical image, measurement schematic, and mixing current response of a graphene field-effect-transistor (FET) vapor sensor. (A) Experimental setup showing a gas chromatography (GC) injector connected to the graphene sensor and flame ionization detector (FID, standard vapor detector with <0.1 s time resolution and <1 ppb sensitivity) through a GC separation column and a Y-split. (B) Optical image of the sensor capped with a silicon flow channel and a GC guard column inserted at one end. The flow channel (dimensions - 400 µm x 400 µm) was secured using a polymer adhesive at the edge. (Inset) Scanning electron micrograph of a typical graphene device. Scale bar: 5 µm. (C) Mixing current measurement setup showing amplitude modulated input signal at source electrode; and an illustration of chloroform molecule on top of graphene channel. The arrow represents the dipole moment vector of chloroform. (D) Mixing current response of a graphene-FET sensor to injections of (1) pentane, (2) hexane, (3) benzene, (4) chlorobenzene, (5) dichloromethane, (6) chloroform, (7) N, N-dimethylformamide (DMF), (8) dimethylmethylphosphonate (DMMP), and (9) acetone.

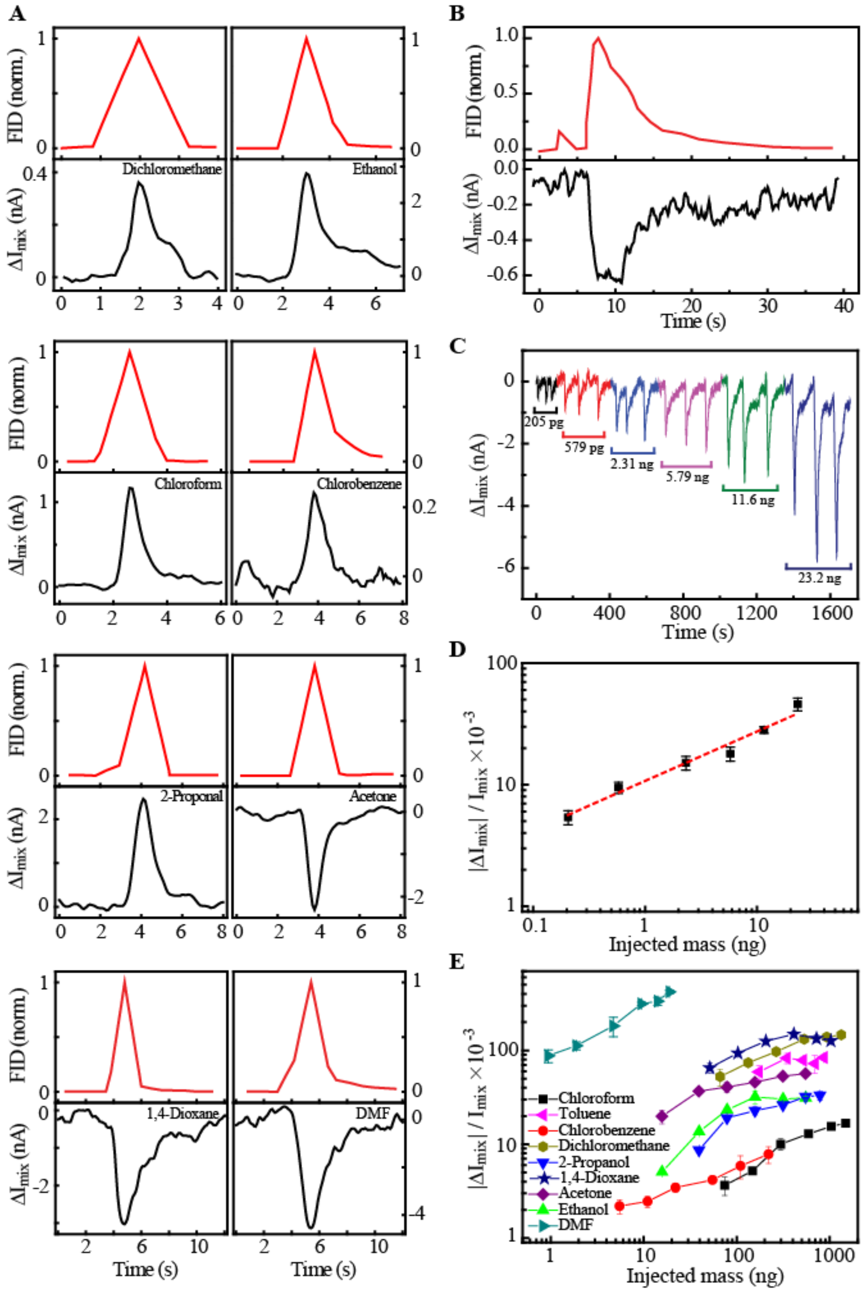

Figure 7-2 Graphene sensor response to different chemical vapors. (A) Comparison of the temporal response of the FID (red, top panels) and graphene sensor (L = 7 µm, W = 2 µm) measured at V_{sd} = 0 V, V_g = 0 V, f_c = 100 kHz, v_{ac} = 20 mV, f_m = 1.4342 kHz, m = 1 (black, bottom panels) to the same injected mass of 8 analytes (dichloromethane – 66.5 ng, ethanol – 78.8 ng, chloroform – 296 ng, chlorobenzene – 5.5 ng, 2-propanol – 78.5 ng, acetone – 15 ng, 1,4-dioxane – 51.5 ng, and DMF – 4.72 ng). 1, 4-dioxane and DMF were measured on a device with L = 9 µm, W = 2 µm at v_{ac} = 30 mV, all other parameters being the same. (B) Temporal response of the FID (red) and graphene sensor (black) to 205 pg injected mass of DMMP. (C) Chromatographic response of the sensor in Fig. 2B, to repeated pulses

of DMMP at varying mass injections noted in the figure. (D) Measured relative mixing current change of graphene sensor to DMMP mass injections from Fig. 2C. Linear fit (red dashed line) to log-log plot gives a slope of 0.4. (E) Measured relative mixing current response at varying mass injections of 9 different analytes. Error bars in (D) and (E) show the standard deviation over 3 runs. Analytes were delivered using a 70 cm long guard column at a carrier gas (helium) flow rate of 8 mL/min. All measurements were carried out in air, at atmospheric pressure and room temperature.

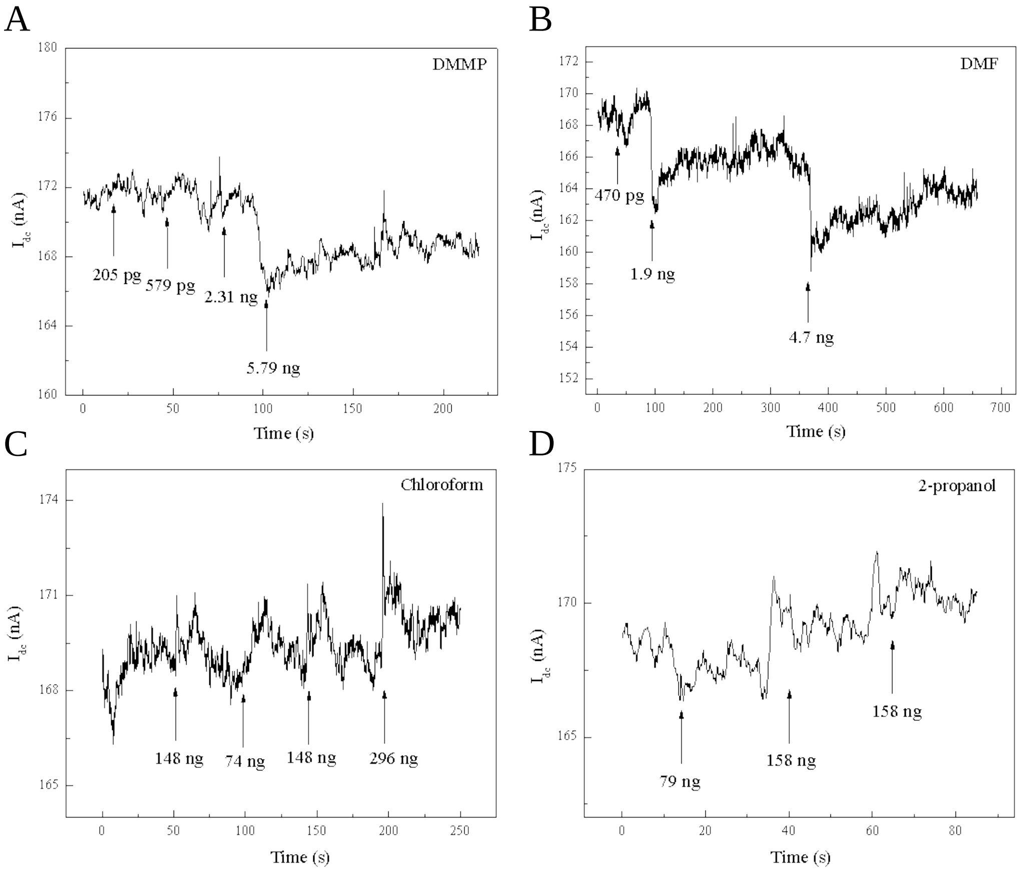

Figure 7-3 DC response of a GrFET sensor to various chemical vapors. The graphene FET sensor and the experimental conditions remained the same as those in Fig. 2 (main text), except V_{dc} = 1 mV and V_g = 0 V.

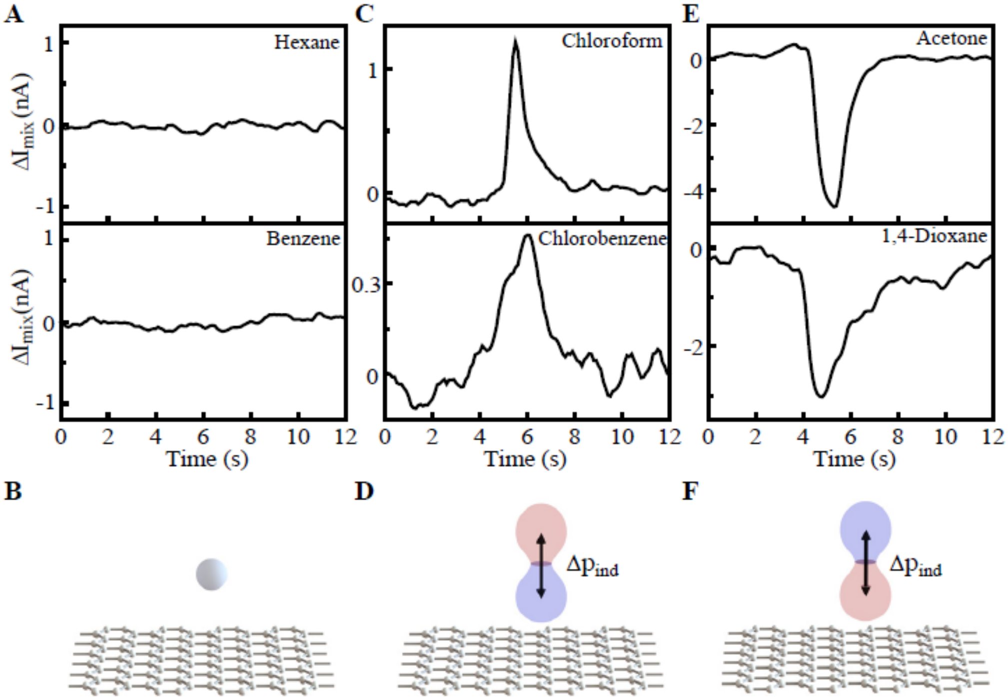

Figure 7-4 Graphene sensor chromatographic response and the corresponding illustration of the orientation of vapor molecules. (A) Measured mixing current response for an injected mass of 131 ng and 43.8 ng of hexane (0 D, top) and benzene (0 D, bottom) respectively. (B) Schematic illustration of an analyte with zero dipole moment on graphene. (C) Measured mixing current response for an injected mass of 296 ng and 55 ng of chloroform (1.04 D, top) and chlorobenzene (1.54 D, bottom) respectively. (D) Schematic illustration of an analyte on graphene with the electronegative cloud (blue) closer to the graphene surface. (E) Measured mixing current response for an injected mass of 156 ng and 51.5 ng of acetone (2.88 D, top) and 1, 4-dioxane (0.45 D, bottom) respectively. (F) Schematic illustration of an analyte on graphene with the electropositive cloud (red) closer to the graphene surface. Double sided arrows in (D) and (F) represent the induced dipole fluctuation, Δp_{ind}, due to the sinusoidal AC excitation field.

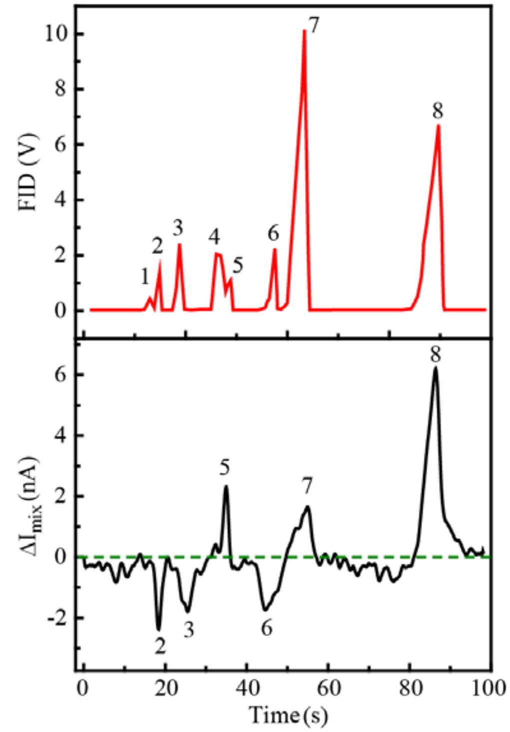

Figure 7-5 GC chromatograms obtained simultaneously from the FID (red, top panel) and the graphene sensor (black, bottom panel). The mixing current baseline for the sensor is marked by the green dashed line in lower panel. Graphene sensor device (dimensions - L = 2 µm and W = 2 µm) was operated at V_{sd} = 0 V, V_g = 0 V, f_c = 100 kHz, v_{ac} = 10 mV, f_m = 1.4342 kHz and m = 1. Peaks correspond to: (1) – pentane, (2) – acetone, (3) – 2-propanol, (4) – benzene, (5) – chloroform, (6) – 1,4-dioxane, (7) – toluene, and (8) – chlorobenzene. Analytes were separated and delivered using a combination of 7.2 m long CP-SIL-5-CB column, 2.8 m long Carbowax column, and 70 cm long guard column. A Y-split was used for simultaneous delivery of analytes to the FID and the graphene sensor.

Analyte	**Dipole moment (D)**	**Boiling point (^{o}C)**	**Smallest injected mass (ng)**	**FWHM ($t_{1/2}$) (s)**	**Concentration at minimum injected mass (ppm)**
Benzene	0	36	-	-	-
Hexane	0	69	-	-	-
Pentane	0	80	-	-	-
Toluene	0.37	111	172	1.61	210
1,4-Dioxane	0.45	101	52	2.1	50
Chloroform	1.04	61	74	0.68	164
Chlorobenzene	1.54	131	5.5	0.75	12
Dichloromethane	1.6	40	66	1	139
2-Propanol	1.66	82	39	1.12	105
Ethanol	1.69	79	15	0.9	65
Acetone	2.88	56	15	0.8	58
DMMP	3.62	181	0.205	6.83	0.043
DMF	3.82	153	0.944	2.54	0.92

Table 7-1 Experimentally detected minimum concentration of analytes. Listed are the smallest injected mass detected by the sensor, full width half maximum (FWHM; mean of 3 runs), and minimum concentration calculated using injected mass and FWHM.

References

1. W. Lu and C. M. Lieber, *Nat. Mater.*, 2007, **6**, 841-850.
2. A. K. Geim and K. S. Novoselov, *Nat. Mater.*, 2007, **6**, 183-191.
3. P. L. McEuen, *Phys. World*, 2000, **13**, 31-36.
4. J. Li, Y. J. Lu, Q. Ye, M. Cinke, J. Han and M. Meyyappan, *Nano Lett.*, 2003, **3**, 929-933.
5. C. Yu, Q. Hao, S. Saha, L. Shi, X. Y. Kong and Z. L. Wang, *Appl. Phys. Lett.*, 2005, **86**.
6. E. S. Snow, F. K. Perkins, E. J. Houser, S. C. Badescu and T. L. Reinecke, *Science*, 2005, **307**, 1942-1945.
7. F. Schedin, A. K. Geim, S. V. Morozov, E. W. Hill, P. Blake, M. I. Katsnelson and K. S. Novoselov, *Nat. Mater.*, 2007, **6**, 652-655.
8. C. Y. Lee, R. Sharma, A. D. Radadia, R. I. Masel and M. S. Strano, *Angew. Chem. Int. Ed.*, 2008, **47**, 5018 –5021.
9. Y. P. Dan, Y. Lu, N. J. Kybert, Z. T. Luo and A. T. C. Johnson, *Nano Lett.*, 2009, **9**, 1472-1475.
10. V. Dua, S. P. Surwade, S. Ammu, S. R. Agnihotra, S. Jain, K. E. Roberts, S. Park, R. S. Ruoff and S. K. Manohar, *Angew. Chem.-Int. Edit.*, 2010, **49**, 2154-2157.
11. Y. Dan, Y. Lu, N. J. Kybert, Z. Luo and A. T. C. Johnson, *Nano Lett.*, 2009, **9**, 1472-1475.
12. J. D. Fowler, M. J. Allen, V. C. Tung, Y. Yang, R. B. Kaner and B. H. Weiller, *ACS Nano*, 2009, **3**, 301-306.
13. B. Kumar, K. Min, M. Bashirzadeh, A. B. Farimani, M. H. Bae, D. Estrada, Y. D. Kim, P. Yasaei, Y. D. Park, E. Pop, N. R. Aluru and A. Salehi-Khojin, *Nano Lett.*, 2013, **13**, 1962-1968.
14. D. R. Kauffman and A. Star, *Angew. Chem. Int. Edit.*, 2008, **47**, 6550-6570.
15. C. Y. Lee, R. Sharma, A. D. Radadia, R. I. Masel and M. S. Strano, *Angew. Chem. Int. Ed.*, 2008, **47**, 5018-5021.
16. J. Li, Y. Lu, Q. Ye, M. Cinke, J. Han and M. Meyyappan, *Nano Lett.*, 2003, **3**, 929-933.
17. T. Someya, J. Small, P. Kim, C. Nuckolls and J. T. Yardley, *Nano Lett.*, 2003, **3**, 877-881.
18. J. Wang and M. Musameh, *Anal. Chem.*, 2003, **75**, 2075-2079.
19. S. Rumyantsev, G. X. Liu, M. S. Shur, R. A. Potyrailo and A. A. Balandin, *Nano Lett.*, 2012, **12**, 2294-2298.
20. C. Y. Lee and M. S. Strano, *J. Am. Chem. Soc.*, 2008, **130**, 1766-1773.
21. A. Salehi-Khojin, K. Y. Lin, C. R. Field and R. I. Masel, *Science*, 2010, **329**, 1327-1330.
22. X. Li, W. Cai, J. An, S. Kim, J. Nah, D. Yang, R. Piner, A. Velamakanni, I. Jung, E. Tutuc, S. K. Banerjee, L. Colombo and R. S. Ruoff, *Science*, 2009, **324**, 1312-1314.
23. X. Li, W. Cai, L. Colombo and R. S. Ruoff, *Nano Lett.*, 2009, **9**, 4268-4272.
24. L. Zhao, K. T. Rim, H. Zhou, R. He, T. F. Heinz, A. Pinczuk, G. W. Flynn and A. N. Pasupathy, *Solid State Commun.*, 2011, **151**, 509-513.

Chapter VIII

Conclusions and future work

8.1 Conclusions

The preceding chapters have detailed several projects related to the development of sensors for use in µGC. Three type of sensors were development and characterized. Two were optical sensors i.e. FP sensor and LSPR sensor and the third was a electrical GrFET sensor.

We have developed a robust silicon based FP vapor sensor which was exceptionally easy to fabricate and was capable of sub-picogram detection limits. These sensors can be implemented as an array, by using different polymers as the FP cavity and therefore used to build response patterns based on analyte-polymer interaction. We further explored a method a standardize the output data from the FP sensor wherein responses would not be dependent on the position of the interrogating wavelength on the FP spectrum or the thickness of the polymer. Finally we demonstrated the monolithic integration of the sensors with separation columns leading to decreased system dead volumes. Sensors were shown to consistently detect a mixture of analytes eluted from separation columns using Helium as carrier gas. The use of a laser and CMOS detector was also implemented to improve sensitivity and resolution over traditional optical schemes used with optical sensors.

We performed proof of concept measurements on MPNs to illustrate that the LSPR spectra of films of these particles will behave differently under exposure to different analytes. We performed spectroscopic measurements to illustrate the differences in the modified LSPR spectrum in the presence of heptane and toluene. We also showed a better method to measue such changes by interrogating the sensing film with two lasers whose output wavelengths were on opposite sides of the LSPR peaks.

The final sensor development yielded a AC Gr-FET sensor which illustrated the superiority of using AC measurement over DC measurement techniques. Not only was this sensor more sensitive that previously reported CNT or graphene FET sensors, with detection limits under 10 pg, it was also the first time such a sensor was shown to be capable to sub second response times, without any need for external heating or stimulus.

8.2 Future work

While significant progress has been made on the development of sensors and exploration of sensing schemes, there is still a significant amount of work that remains to be done.

Work on the silicon-based FP yielded exceptional sensitivity and response times along with a demonstrable ease for integration with µGC components, however work remains to be done on a thorough study effect polymer thickness has on sensing capabilities. Apart from the polymers utilized by us there are several other polymers[1,2] and materials, such a zeolite,[3-5] and sol-gels[6-8] which are worthy of investigation. These polymers and materials have been shown to be easily deposited on desired substrates and hence would be suitable for on-chip FP sensors fabrication. The integration of these sensors with other µGC components including pre-concentrators and separation columns will be investigated in further detail. To be fully integrated in µGC systems, the optical setup will need to be significantly miniaturized, this can be easily accomplished using a low cost solid state laser driven by a small DC current, and the use of a CMOS imager connected to a data acquisition system. In terms of fabrication it is necessary to avoid the degradation of sensor quality and low yield experienced when using drop coating, and to investigate more economical methods of fabrication. The use of a spin coated FP sensor in µGC is ideal for purposes of high sensitivity and excellent chormatographic resolution to discriminate between analytes in a mixture. Finally these integrated sub-systems can be utilized for development of small multi-dimensional GC systems.

The LSPR sensors showed selectivity between analytes however the sensitivity of the sensors was poor and not suitable for µGC. Work is currently being done in collaboration with the Zellers group to develop a method to implement these MPNs in a high Q-factor sensing scheme, such as the µOFRR, to enhance optical path length and hence sensitivity. Work on the µOFRR has yielded exciting results with PDMS coatings and shows great promise for use with MPNs to develop selective sensing arrays.[9,10] For these LSPR/µOFRR sensors to be implented in µGC, would require a significant reduction in optical setup; methods similar to those mentioned above, for FP sensors, can be utilized here too.

Graphene sensors are a relatively new entry in the field of chemical sensing. The mechanics and dynamics of the sensing scheme can yield interesting insights into the working and optimization of these sensors. An ongoing collaboration with the Zhong group is looking into the properties of these sesnors, with work currently focusing on temperature effects on sensitivity and desorption as well as a push to a goal of achieving single molecule detection. Work here can also be done to find methods to use AC sensing to detect non-polar molecules through some form of surface modifications. Another solution to this problem with sensing non-polar analytes would be the use of a multi transducer array, wherein one or more other types of sensors can be used to to sense the analytes including non-polar analytes. Long term goals with these sensors with include a complete chip based GrFET sensor, with on-chip mixers and driving circuitry. With the small footprint for such a scheme woud use it would be ideal for use in µGC.

Apart from these sensors there are numerous other sensing schemes which have not been thoroughly characterized. Grating structures have been shown to be useful in chemical sensing, however apart from a couple of papers on polymer gratings there has minimal research on these sensors.[11,12] Materials like Molybedenum Disulphide, a semicondutor material with band gap of 1.8 eV, which shares some properties with graphene is a candidate for FET based sensing method similar to those demonstrated with the graphene-FETs.[13]

From an implementation side the sensors we have developed can be useful for breath analysis for cancer detection. Breast cancer is one of the cases where these sensors can play a vital role in early detection. Worldwide breast cancer kills nearly 500,000 people each year, accounting for over 13 percent of all cancer related deaths in women.

Current method of detection include magnetic resonance imaging (MRI),[14-16] mammograms,[14,16,17] ultrasound,[16,18] etc. However these tests can be expensive, require prohibitively complex equipment and training; while exposing patients to harmful radiation. Breath analysis is a prime candidate to replace these tests with a fast, non-invasive, and economical method to screen from breast cancer. It has been shown that several biomarkers are present in the breath of women with breast cancer including pentane, nonane, 5-methyl tridecane, 3 methyl nonadecane, 4-methyl dodecane, 2-methyl propane, and 3-methyl undecane.[19,20] These compounds can all be easily detected by our sensors and used as a basis to screen for breast cancer.

Breast cancer isn't the only condition where breath analysis can be used for screening purposes. Several reports have been published on work pertaining to lung cancer screening using vapor sensors.[21-24] Worldwide lung cancer is responsible for almost 1.4 million deaths annually and in the United States has a 5 year mortality rate of over 85%. This is partially due to the difficulties related to early screening of lung cancer and a lack of symptoms especially in the early stages. Chen *et al.* identified 1-butanol and 3-hydroxy-2-butanone as VOCs which are found in significantly higher concentrations in the breath of people diagnosed with lung cancer.[23]

Apart from these applications it might be possible to perform breath analysis for a host of oral and esophageal diseases and infections. However to the best of our knowledge no significant work has been performed in this area.

References

1. F. L. Dickert and O. Hayden, *TrAC Trend. Anal. Chem.*, 1999, **18**, 192-199.
2. F. L. Dickert, P. Forth, P. Lieberzeit and M. Tortschanoff, *Fresen. J. Anal. Chem.*, 1998, **360**, 759-762.
3. J. Zhang, X. Tang, J. Dong, T. Wei and H. Xiao, *Sens. Actuat. B-Chem*, 2009, **135**, 420-425.
4. P. Yang, X. Ye, C. Lau, Z. Li, X. Liu and J. Lu, *Anal. Chem.*, 2007, **79**, 1425-1432.
5. J. Zhou, P. Li, S. Zhang, Y. Long, F. Zhou, Y. Huang, P. Yang and M. Bao, *Sens. Actuat. B-Chem*, 2003, **94**, 337-342.
6. B. D. M. Craith, C. M. Donagh, A. K. McEvoy, T. Butler, G. O'Keeffe and V. Murphy, *J. Sol-Gel Sci. Techn.*, 1997, **8**, 1053-1061.
7. J. Lin and C. W. Brown, *TrAC Trend. Anal. Chem.*, 1997, **16**, 200-211.
8. R. Zusman, C. Rottman, M. Ottolenghi and D. Avnir, *J. Non-Cryst. Solids*, 1990, **122**, 107-109.
9. K. Scholten, K. Reddy, X. Fan and E. Zellers, Micro-optofluidic ring resonator structires for selective detection of organic vapors Barcelona, Spain, 2013.
10. K. Scholten, F. Xudong and E. T. Zellers, *Appl. Phys. Lett.*, 2011, **99**, 141108-141108-141103.
11. R. C. Bailey and J. T. Hupp, *J. Am. Chem. Soc.*, 2002, **124**, 6767-6774.
12. R. C. Bailey and J. T. Hupp, *Anal. Chem.*, 2003, **75**, 2392-2398.
13. P. A. Lieberzeit, A. Afzal, A. Rehman and F. L. Dickert, *Sens. Actuat. B-Chem*, 2007, **127**, 132-136.
14. M. Kriege, C. T. M. Brekelmans, C. Boetes, P. E. Besnard, H. M. Zonderland, I. M. Obdeijn, R. A. Manoliu, T. Kok, H. Peterse, M. M. A. Tilanus-Linthorst, S. H. Muller, S. Meijer, J. C. Oosterwijk, L. V. A. M. Beex, R. A. E. M. Tollenaar, H. J. de Koning, E. J. T. Rutgers and J. G. M. Klijn, *New Engl. J. Med.*, 2004, **351**, 427-437.
15. C. D. Lehman, C. Gatsonis, C. K. Kuhl, R. E. Hendrick, E. D. Pisano, L. Hanna, S. Peacock, S. F. Smazal, D. D. Maki, T. B. Julian, E. R. DePeri, D. A. Bluemke and M. D. Schnall, *New Engl. J. Med.*, 2007, **356**, 1295-1303.
16. E. Warner, D. B. Plewes, R. S. Shumak, G. C. Catzavelos, L. S. Di Prospero, M. J. Yaffe, V. Goel, E. Ramsay, P. L. Chart, D. E. C. Cole, G. A. Taylor, M. Cutrara, T. H. Samuels, J. P. Murphy, J. M. Murphy and S. A. Narod, *J Clin. Oncol.*, 2001, **19**, 3524-3531.
17. E. D. Pisano, C. Gatsonis, E. Hendrick, M. Yaffe, J. K. Baum, S. Acharyya, E. F. Conant, L. L. Fajardo, L. Bassett, C. D'Orsi, R. Jong and M. Rebner, *New Engl. J. Med.*, 2005, **353**, 1773-1783.
18. W. A. Berg, J. D. Blume, J. B. Cormack and et al., *JAMA- J. Am. Med. Assoc.*, 2008, **299**, 2151-2163.
19. H. B. E. Hietanen, J. C. Bereziat, A. M. Camus, S. McClinton, O. Eremin, L. Davidson, and P. Boyle, *Eur. J. Clin. Nutr.*, 1994, **48**, 575-586.
20. M. Phillips, R. N. Cataneo, B. A. Ditkoff, P. Fisher, J. Greenberg, R. Gunawardena, C. S. Kwon, F. Rahbari-Oskoui and C. Wong, *Breast J.*, 2003, **9**, 184-191.

21. I. Horváth, Z. Lázár, N. Gyulai, M. Kollai and G. Losonczy, *Eur. Respir. J.*, 2009, **34**, 261-275.
22. C. Di Natale, A. Macagnano, E. Martinelli, R. Paolesse, G. D'Arcangelo, C. Roscioni, A. Finazzi-Agrò and A. D'Amico, *Biosens. Bioelectron.*, 2003, **18**, 1209-1218.
23. G. Song, T. Qin, H. Liu, G.-B. Xu, Y.-Y. Pan, F.-X. Xiong, K.-S. Gu, G.-P. Sun and Z.-D. Chen, *Lung Cancer*, 2010, **67**, 227-231.
24. H. P. Chan, C. Lewis and P. S. Thomas, *Lung Cancer*, 2009, **63**, 164-168.

Appendix I

Fabry-Pérot etalon

The Fabry-Pérot (FP) interferometer or etalon is named after Charles Fabry and Alfred Pérot, who are credited with it's discovery and the explanation of interference fringes. An FP etalon consists of a transparent plate or medium with reflective surfaces while an interferometer is considered to be two mirrors placed parallel to each other, however these terms are used interchangeably.

The effect of phase change as the incident light is reflected and transmitted at each reflective surface gives rise to the characteristic FP intereference spectrum. The peaks in the spectrum arise from constructive interference when the beams are in phase and when the transmitted beams are out of phase the destructive intereference causes minimas in the spectrum.

Consider the FP interferometer shown in Fig. A-1, with bulk refractive index (RI) n_2 surronded by a medium with RI n_1. When a beam of light is incident on the etalon at an angle of θ using Snell's law we can calculate the angle of the light through the FP cavity.

$$\Phi = \sin^{-1}\left(\frac{n_1}{n_2}\sin\theta\right),$$

Whether the transmitted beams are in phase or out of phase is determined by the thickness of the cavity (t), the refractive index of the cavity (n_2), the wavelength of light (λ) and the angle of light within the cavity (Φ). The phase difference is given by δ and shown to be;

$$\delta = \frac{4\pi nt}{\lambda}\cos\Phi ,$$

For most FP etalons reflection at both interfaces is the same (R), so the transmission function can be given as,

$$T_e = \frac{(1-R)^2}{1+R^2-2R\cos\delta} = \frac{1}{1+F\sin^2\left(\frac{\delta}{2}\right)} ,$$

where the coefficient of finesse F is,

$$F = \frac{4R}{(1-R)^2} ,$$

The sum of transmission and reflection is 1 in the absence of absorbance.

Another important parameter is the distance between two peaks or free spectral range (FSR), $\Delta\lambda$ which is shown to be,

$$\Delta\lambda = \frac{\lambda^2}{2nt\cos\Phi} ,$$

where λ is the the central wavelength.

The FSR is reated to the finesse (f) of the FP etalon and the full width half maximum of a transmission band $\delta\lambda$ by,

$$f = \frac{\Delta\lambda}{\delta\lambda} .$$

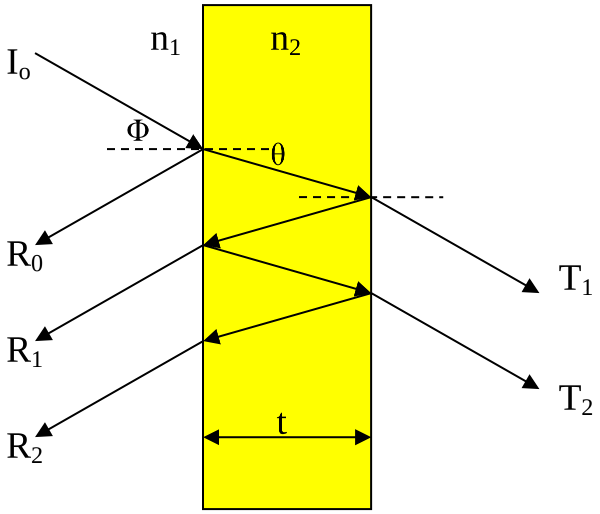

Figure A-1 Typical FP structure with optical beam path illustrated.

Appendix II

Localized surface plasmon resonance

Surface plasmon resonance (SPR) refers to the oscillations of electrons in a material upon stimulation by electromagnetic radiation. This phenomena is observed in materials with negative real components of dielectric constant and a small positive imaginary component. The resonance conditions are dependent on the oscillation frequency of the electrons under the influence of the restoring force from the positive nuclei. The occurrence of these oscillations in nanoparticles of noble metals like gold and silver is known as localized surface plasmon resonance (LSPR). These nanoparticles have to be much smaller than the wavelength of the electromagnetic radiation in which the nanoparticle is placed.

A comprehensive study on LSPR by Van Duyne *et al.* is available in ref. [1], including a complete deriviation of the equation and theory governing LSPR. The key equation to note after derivation of Maxwell's equation is shown below,

$$E(\lambda) = \frac{24\pi^2 N a^2 \varepsilon_{out}^2}{\lambda \ln(10)} \left(\frac{\varepsilon_i(\lambda)}{\left(\varepsilon_r(\lambda) + \chi\varepsilon_{out}\right)^2 + \varepsilon_i(\lambda)^2} \right),$$

where $E(\lambda)$ is the extinction at a given wavelength, a is the size of the nanoparticle, ε_i is the wavelength dependent imaginary component of the nanoparticle dielectric, while ε_r is thewavelength dependent real component of the same, N is the density of nanoparticles, ε_{out} refers to the dielectric constant of the surrounding medium and χ is a factor used to account for the geometries of various nanoparticles. There is clear dependence of extinction on the dielectric surrounding the nanoparticle, hence a change in the external dielectric will initiate a change in the extinction spectrum making LSPR a useful method to sense the external medium.

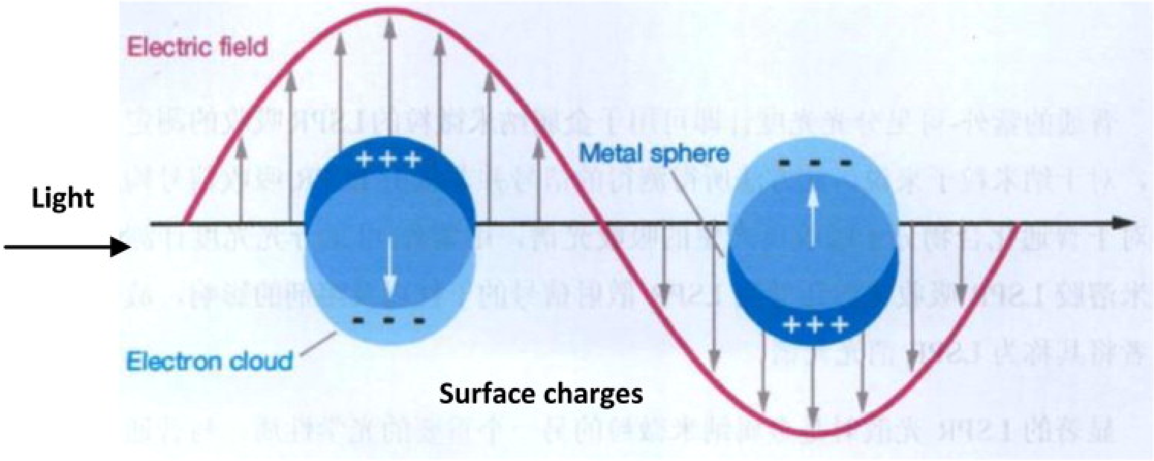

Figure A-2. Induced LSPR of a spherical nanoparticle in a electromagnetic field. Reprinted with permission from [2]. Copyright Elsevier.

References

1. K. A. Willets and R. P. Van Duyne, *Annu. Rev. Phys. Chem.*, 2007, **58**, 267-297.
2. A. Liang, Q. Liu, G. Wen and Z. Jiang, *TrAC Trend. Anal. Chem.*, 2012, **37**, 32-47.

Appendix III

Method to calculate concentration from injected mass

To measure the concentration equivalents of the injected mass for any given analyte we use the full width half maximum, flow rate of carrier gas, analyte molar mass and density.
Measured Helium flow rate

= 8 ml/min

Amount of helium which flows over the device in ‘t’ seconds

= 8t/60 mL

24 Liters = 1mole at room temperature and standard pressure
So, number of moles of Helium which pass over the device

$$= \frac{8t}{60} \times 10^{-3} \times \frac{1}{24} = 5.56 \times 10^{-6} \times t \text{ moles}$$

Volume of analyte injected

$= x$ µL

Density of analyte

$= \rho$ kg/m^3 $= \rho$ µg/uL

Therefore, amount of injected analyte

$= x\rho$ microgram

Molar mass of analyte

$= M$ g/mol

Therefore, $x\rho$ microgram

$$= \frac{x\rho \times 10^{-6}}{M} \text{ moles}$$

Hence, concentration

$$= \frac{\frac{x\rho \times 10^{-6}}{M}}{5.56 \times 10^{-6} \times t} \times 10^{6}$$

$$= \frac{x\rho}{5.56Mt} \times 10^{6} \text{ ppm}$$

Appendix IV

Polymer Structures

PDMS

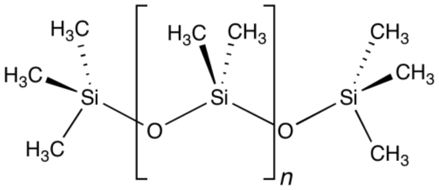

OV-1701

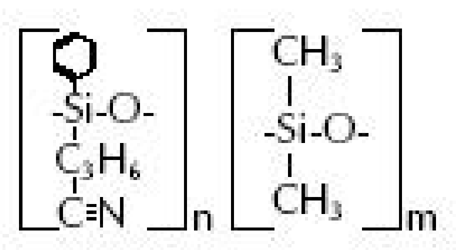

OV-73

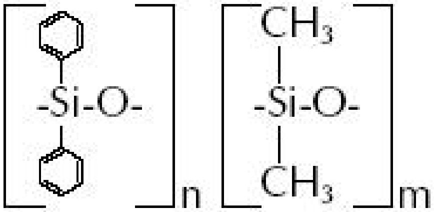

OV-215

Not available

Appendix V

Mixing current derivation

The charge density on graphene is expressed as

$$n_{total} = \sqrt{n_o^2 + n^2(x)}$$

Since we are operating in the linear regime far away from the Dirac point, $n(x) >> n_o$, and

$$n_{back-gate} = \frac{C_{bg}V_{bgo}}{e} \text{ and } n_{\Delta} = \frac{C_{\Delta} \cdot \Delta\phi}{e},$$

where C_{bg} is the back gate capacitance, V_{bgo} is the back gate potential relative to the dirac point (V_{bg}-V_{dirac}), and $\Delta\phi$ is any extraneous potential due to a molecular adsorbate present in the graphene vicinity and C_{Δ} is the associated capacitance with it. The total charge density can be expressed as

$$n(x) = C_{bg}\left(\frac{V_{bgo}}{e} + \frac{C_{\Delta}}{eC_{bg}}\Delta\phi - V(x)\right),$$

where $V(x)$ is the voltage at a point x due to the source bias.

Now, for a simple transistor model we have

$$I = \frac{Wq\mu}{L}\int_0^{Vsd} n(x).dV(x) = \frac{\mu W}{L}\int_0^{Vsd} C_{bg}\left(V_{go} + \frac{C_{\Delta}}{C_{bg}}\Delta\phi + V(x)\right) \cdot dV(x)$$

$$I = \frac{\mu W}{L} C_{bg} \left[(V_{go} + \frac{C_{\Delta}}{C_{bg}} \Delta\phi) \cdot V_{sd} + V_{sd}^2 \right] \qquad \text{-equation (1)}$$

Now, when a molecular dipole is located at a distance h above the graphene surface,

$$\Delta\phi = \frac{p}{4\pi\varepsilon_0 h^2} = \frac{|p_{perm}| + |p_{ind}|}{4\pi\varepsilon_0 h^2}$$

where $|p_{perm}|$ and $|p_{ind}|$ are the permanent and induced dipole components perpendicular to the graphene.

In the presence of a AM modulated field, $\delta V_{ac} = v_{ac}(1 + m \cdot \cos(\omega_m t)) \cdot \cos(\omega_c t)$, the potential would also be modulated at the drive frequency (a fair assumption as the screening in gas phase is negligible and our operating frequency is 100 kHz). Since we are operating our graphene mixers at very low drive voltages, we don't expect the permanent dipoles to flip, consequently, the potential fluctuation at the graphene surface can be represented as

$$\Delta\tilde{\phi} = \frac{p}{4\pi\varepsilon_0 h^2} = \frac{|p_{perm}| + |p_{ind}| \cos(\omega_c t)}{4\pi\varepsilon_0 h^2} \qquad \text{-equation (2)}$$

Now, substituting equation (2) in equation (1) and using the expression,

$$\delta V_{sd} = v_{ac}(1 + m\cos\omega_m t)\cos\omega_c t = v_{ac}\cos\omega_c t + \frac{m}{2}\cos(\omega_c - \omega_m)t + \frac{m}{2}\cos(\omega_c + \omega_m)t,$$

we have our mixing current term, which the lock-in amplifier reads at frequency ω_m

$$I_{mix}^{\omega_m} = m\frac{\mu W C_{bg}}{L}(\frac{1}{4}v_{ac}^2 + \frac{1}{2}\frac{C_{\Delta}}{C_{bg}}\frac{|p_{ind}|}{4\pi\varepsilon_0 h^2}),$$

where the first term is the baseline mixing current and the second term is our mixing current signal change in the presence of a molecular adsorbate.

Hence,

$$\Delta I_{mix}^{\omega_m} = m\frac{\mu W C_{bg}}{L}\left(\frac{1}{2}\frac{C_{\Delta}}{C_{bg}}\frac{|p_{ind}|}{4\pi\varepsilon_0 h^2}\right)v_{ac}$$

Now, relative gate coupling, $\frac{C_{\Delta}}{C_{bg}}$ can be taken to be $\frac{h}{t_{ox}}$ which gives us for p_{ind} = 1 Debye,

$\Delta I_{mix}^{\omega_m} = \frac{20}{7} pA$, considering v_{ac} = 40 mV on the device, L = 7 µm, W=2 µm, μ = 0.1 m^2/V.s, m = 1, t_{ox} = 200 nm and h = 5 nm.

Appendix VI

I-V characteristics of GrFET

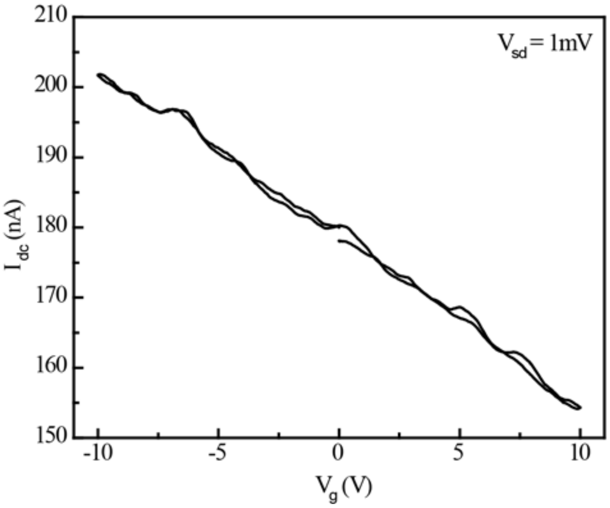

I-V characteristics of a graphene-FET used in VOC detection